DESIGN AND OPTIMIZATION OF MICRO/NANO PHOTONICS AIMING AT SENSOR APPLICATIONS

HO CHONG PEI
(B.Eng.(Hons.), NUS)

A THESIS SUBMITTED

FOR THE DEGREE OF DOCTOR OF PHILOSOPHY
DEPARTMENT OF ELECTRICAL & COMPUTER ENGINEERING
NATIONAL UNIVERSITY OF SINGAPORE

2016

DECLARATION

I hereby declare that this thesis is my original work and it has been written by me in its entirety. I have duly acknowledged all the sources of information which have been used in the thesis.

This thesis has also not been submitted for any degree in any university previously.

HO CHONG PEI

05 MAY 2016

ACKNOWLEDGEMENTS

There have been help, guidance and hospitality received in making this thesis possible. With that, I wish to express my sincere acknowledgement to the persons for making the difference in my doctorate degree study.

First and foremost, I would like to express my deepest gratitude to my advisor, Professor Vincent Lee Chengkuo, for his extraordinary guidance, knowledge sharing and selflessness understanding. The entire journey to the completion of this program was made much more enjoyable due to his enormous support. His great mentorship has really made a meaningful impact to my life and it is an honour to have him as my advisor.

I want to thank my fellow group mates from CICFAR, Department of Electrical and Computer Engineering, National University of Singapore (ECE, NUS), especially individuals like Prakash, Li Bo, Wang Nan and Jeffrey. The countless discussions we had were instrumental and it was my pleasure to have all of them as my team mates and close friends.

My special thanks to Dr. Alex Gu, Dr. Cai Hong, Dr. Wang Jian and Dr. Pitor Kropelnicki who were there to support me whenever I needed help. They had placed their trust in me and I hope that I have lived up to their expectations.

I am also extremely grateful to the cleanroom staffs from Institute of Microelectronics (A*STAR Singapore) especially Dexian, Eric, Ozalis, Fariz,

Badrul and Yong Wei. Their warmth and friendliness brightened up the cleanrooms and they made the time spent in the cleanrooms much more enjoyable.

Thanks to my parents and siblings for being there whenever I needed help during my study. I would not be able to make it through the programme without their strong encouragement, support and patience. This thesis is also dedicated to my wife, You Mei, for her unconditional support, love, kindness and time throughout the long journey towards the completion of my Ph.D study.

Finally, all the contributions from the many others not named above are also greatly appreciated.

CONTENTS

SUMMARY

Optical passive devices such as sensors play an important role in everyday applications as they are found to be extremely powerful for the detection and analysis of very infinitesimal changes in the environment physically and chemically. This thesis aims to explore and develop optical based sensors and the work done can be classified into two key methods which involve guided wave and free-space propagation of light.

Guided wave based sensors involve the use of optical waveguides for the guidance of light propagation to the photonics designs. Our work involves the design and fabrication of silicon (Si) based photonic crystal (PhC) waveguide in order to excite the slow light effect, which increases light-matter interaction for enhanced sensitivity. Simulations of the device reveals that the group index and low dispersion bandwidth are optimized to 166 and 1.69 nm, respectively, where the DBP is derived as 0.1812. A Mach-Zehnder interferometer (MZI) is integrated with the PhC waveguide in one of its arms in order to verify the results experimentally. The measured transmission spectrum of fabricated MZI embedded with PhC waveguide show slow light endured interference patterns. The use of aluminium nitride (AlN) as the optical material for guided wave sensor is also attempted. A simple design of PhC resonator with a defect is implemented and measurement reveals a resonance at 1576.3 nm with a quality (Q) factor of around 2000. This creates a strong foundation for further endeavours in optical designs involving AlN.

For free-space based optical sensors, PhC is investigated as an optical reflector which is used in many optoelectronic devices and photonic elements. We design and fabricate a two-dimensional (2-D) PhC reflector with the peak reflection wavelength at 3.55 μm. Measurements reveal that both the circle air holes and square air holes designs show 96.5% and 97.2% reflectance around 3.58μm. We also characterize the performance of the PhC reflector at high temperatures. Measurements done at 450^{o}C reveal that the thermo-optic coefficient is $+1.70\times10^{-4}$ K^{-1}. In order to compensate the redshift by the thermo-optic effect, a simple methodology of changing the air hole dimension is shown. In order to passively correct the shift introduced by thermo-optic effect at all temperatures, an AlN based PhC reflector is fabricated and characterized. The thermo-optic coefficient is estimated as $+2.22\times10^{-5}$ K^{-1}. This is an order of magnitude lower than Si and is better performing in high operating temperatures. The thesis extends the work on PhC reflector to realize a PhC Fabry-Perot filter (FPF). We propose a monolithic approach in the fabrication in order to achieve simplicity and low-risk. After taking fabrication variations into account, the simulated Q-factor is around 540. Measurement of the fabricated device reveals a Q-factor of around 300 which is around an order of magnitude higher than existing works. By employing PhC in Si and AlN to manipulate the propagation of light in both in-plane and free space based photonics, PhC has been shown to enhance the sensitivity of sensors, thus making PhC a possible solution for many sensing needs.

LIST OF TABLES

LIST OF FIGURES

LIST OF SYMBOLS AND ABBREVIATIONS

CMOS	Complementary metal–oxide–semiconductor
Si	Silicon
MtM	More than Moore
ICs	Integrated circuits
OEIC	Optoelectronics IC
Cu	Copper
IO	Input and output
Q-factor	Quality factor
WGM	Whispering gallery mode
FSR	Free spectral range
EM	Electromagnetic
PhC	Photonic crystal
PBG	Photonic band gap
-D	-dimensional
MEMS	Microelectromechanical systems
EIT	Electromagnetically induced transparency
v_g	Group velocity
GVD	Group velocity dispersion
DBP	Delay-bandwidth product
Al_2O_3	Aluminium oxide
TiO_2	Titanium dioxide
SiN	Silicon nitride
MIR	Mid infrared
FIR	Far infrared

NIR	Near infrared
FPF	Fabry-Perot filter
AlN	Aluminium nitride
Mo	Molybdenum
ε_0	Permittivity of free space
$\boldsymbol{\chi^{(1)}}$	Electrical susceptibility
$\boldsymbol{\chi^{(2)}}$	Pockel's coefficient
$\boldsymbol{\chi^{(3)}}$	Kerr's coefficient
SEM	Scanning electron micrograph
IDT	Interdigital transducer
n	Refractive index
$\Delta n/\Delta T$	Thermo-optic coefficient
ΔT	Temperature change
THz	Terahertz
PWE	Plane wave expansion
FDTD	Finite-difference time-domain
r	Radius of the holes
a	Lattice constant
c	Speed of light in free space
PM	Polarization maintenance
CW	Continuous wave
OSA	Optical spectrum analyzer
TE	Transverse Electric
TM	Transverse Magnetic
FTIR	Fourier-transform infrared spectroscopy
CaF_2	Calcium fluoride

MCT	Mercury Cadmium Telluride
FPA	Focal plane array
MZI	Mach-zehnder interferometer
w	Width of the waveguide
SiO_2	Silicon dioxide
PECVD	Plasma-enhanced chemical vapor deposition
BOX	Buried silicon oxide
PVD	Physical Vapour Deposition
DRIE	Deep reactive-ion etching
t	Thickness of the PhC membrane
LPCVD	Low-pressure chemical vapour deposition
PR	Photoresist
VHF	Vapour hydrofluoric acid
L	Length of the square air hole
RIE	Reactive ion etching
R	Reflectance
T	Transmittance
FWHM	Full-width half-maximum
CST	Computer Simulation Technology
MWS	Microwave Studio
CMP	Chemical mechanical polishing

CHAPTER 1: Introduction

Moore's law suggested by G. Moore in 1965 predicted that the numbers of transistors per chip will double every 19 months. Since then, the progress of semiconductor has resulted in the transition from microelectronics into nanoelectronics. Today, complementary metal–oxide–semiconductor (CMOS) electronics forms the basis of the multi-trillion dollar computer, electronics and information technology industry. On top of the conventional building blocks, photonics and sensors become the new promising building blocks for realization of silicon (Si) "More than Moore" (MtM) micro/nano-systems in the near future, where new Si MtM micro/nano-systems will be equipped with various non-digital functionalities. On the other hand, integration of Si integrated circuits (ICs) together with Si photonics will lead to the ultra-high-performance optoelectronics IC (OEIC) in a system-on-chip (SoC) format as shown in Figure 1.1(a). Leveraging chip-scale integration of ultrafast Si photonics and Si electronics, the data transmission bottleneck posted by copper (Cu) metal interconnects in current advanced IC technology can be effectively removed by using optical transmission input and output (IO) terminals. In the coming generation of ICs, Si transistor will still be the foundation of computing layer. However, not only the IO buses, optical passive devices such as memory, modulator and sensors will also be fabricated and embedded in advanced Si photonics IC chips monolithically as well as shown in Figure 1.1(b). Eventually all the active on-chip components, such as lasers, detectors, optical logic gates, are integrated together to realize the all-optical ICs as shown in (c), with

promising scaling of device capacity and reductions in the "cost per bit" for optical data processing efficiency.

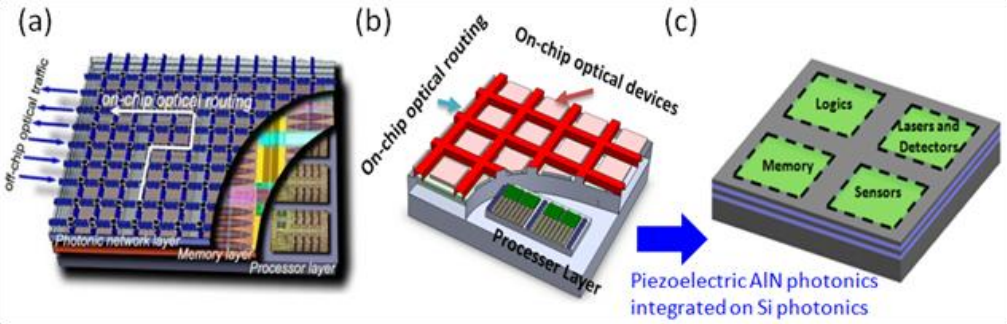

Figure 1.1: (a) Advanced OEIC with optical IO to overcome the data transmission limitation due to Cu interconnects; (b) Photonics ICs integrated with lasers, detectors, optical logic gates, optical memory, modulators and photonics sensors; (c) Monolithic integrated photonics ICs.

In view of future development, optical passive devices such as sensors will play important role in everyday applications as they are found to be extremely powerful for the detection and analysis of very infinitesimal changes in the environment physically and chemically. Optical sensors are robust and resistant to both electrical and magnetic interference. They are also capable of rapid and multiplexed sensing within a single device. More importantly, optical sensors provide either high quality factor (Q-factor) outputs or enhanced light-matter interaction, both of which are essential for high sensitivity sensing [1-7]. Vast number of technologies has been developed for optical sensing and can be classified into two key methods which involve guided wave and free-space propagation of light. Guided wave based sensors involve the use of optical waveguides for the guidance of light propagation to the photonics design such as ring resonators, optical interferometer, photonic crystals, etc [8-14]. This method typically characterises the change in the material property, such as refractive index, to the interested property of the analyte. Another key

technology that is used is free-space based optical sensors [15-17]. Optical reflector and interferometer is frequently used as an optical interface to provide interaction with the light incidence onto the surfaces.

1.1 Guided wave based optical sensors

1.1.1 Ring Resonators based sensors

Optical resonators such as ring and disk resonator, as shown in are the most commonly used optical sensor and are well-studied over the past decades [18-24]. It confines the light energy within the circular path, forming a whispering gallery mode (WGM) as shown in Figure 1.2. Such devices are shown to provide ultra-high Q-factor and ultra-small footprint, making them very attractive in numerous applications. In sensor applications, the effective light-matter interaction length is not determined by the physical dimensions of the structure itself, but by the duration at which the resonator supports the revolving resonance which is reflected in the Q-factor of the resonator. In order to achieve a free spectral range (FSR) of the filter to be larger than the optical communication wavelength, it is necessary for the ring radius to be less than 5 μm. This corresponds to a FSR larger than 30 nm in the case of C-band spectra range [25]. However, this induces larger bending loss in the dielectric waveguide. In addition, the performance of ring resonators is strongly affected by the surface roughness. Finally the nanometer scale gap between the ring and the bus waveguide presents a grand challenge in manufacturing [26].

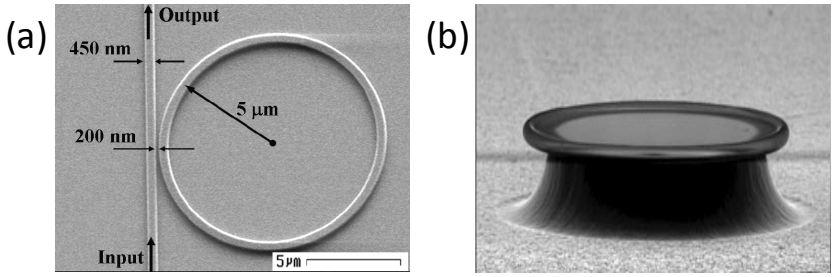

Figure 1.2: Scanning microscope image of a (a) ring and (b) disk resonator.

1.1.2 PhC based Sensors

Photonic crystal (PhC) is a cornerstone technology used in optical sensor due to its promising optical performance. Pioneering works on photonic band gap (PBG) and PhCs done by the Yablonovitch et al. [27] and John et al. [28] has evoked considerable attention from researchers to study its fundamental physics as well as its potential applications. PhCs are engineered nanostructures which provide capability to control and manipulate the propagation of electromagnetic (EM) waves within a given frequency range. Over the last decades, thin film of periodic dielectric nanostructures, e.g. an array of holes in a Si slab, exhibits a PBG for certain frequency ranges. More clearly, the propagation of light within PBG frequency range is forbidden in PhC nanostructures. By leveraging the PBG effect, the light within the PBG frequency range is enabled to be guided or localized by introducing certain defects for example, point and line defects, in the PhC structures [29]. Cavity defects in two-dimensional (2-D) PhCs can provide a high degree of both spatial and temporal light confinement. Various microcavity or nanocavity based PhC resonators are demonstrated as ultra-compact filters of high quality factor (Q-factor) [30, 31]. One added advantage of PhCs filter is that their sizes are suggested to be less than 1/10,000 of those

of conventional optical devices. Compared to conventional optical waveguide devices, PhCs devices can achieve the same functions with their nanometric size, which in turn raises the channel densities within a small area of photonic ICs. Some examples of applications using PhCs are found in many optical communication devices such as channel drop filters, power splitters and PhCs coupler are reported [29, 32-35]. Particularly, channel drop filter plays an important role in photonic ICs [35] because it integrates various functional elements such as multiplexer [36, 37], switch [38, 39], and directional coupler [39] together. Literatures of channel drop filters aimed to enhance the compactness, high spectral selectivity, wide spectral tunability, fast switching, and low-power switching have also been reported [40-42]. These designs are summarized in Figure 1.3.

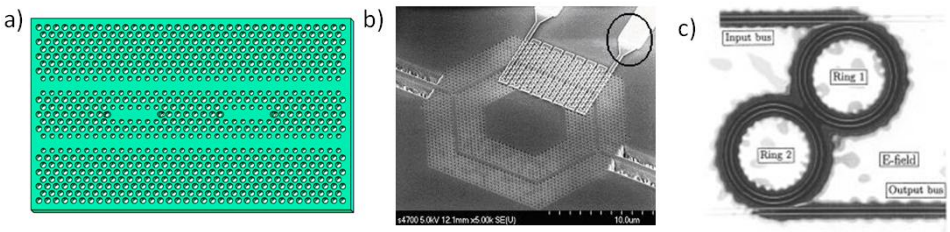

Figure 1.3: (a) Design by Hwang et al. where PhCs design is used as multiplexer [36], (b) a thermo-optic switch by Camargo et al. [38] and (c) a channel-dropping filter design by Little et al [42].

1.1.2.1 Optical biosensors

Single hexagonal PhC nano-ring resonator as shown in Figure 1.4(a) has been investigated as biochemical sensors and [43, 44]. Owning to the good light confinement, the size of a hexagonal nano-ring resonator can be as small as 3 μm^2. 2-D PhCs based hexagonal dual nano-ring resonators with appropriate spacing between the two rings can provide backward or forward channel drop,

and wavelength selective channel drop. As an avenue to enhance effectiveness, it is also greatly desired that multiple biomolecules can be sensed at the same time [45]. In order to achieve this, designs including innovative designs such as PhC based triple nano-ring resonator biosensor or waveguides that are often made into an array as shown in Figure 1.4(b) and (c) [45-48].

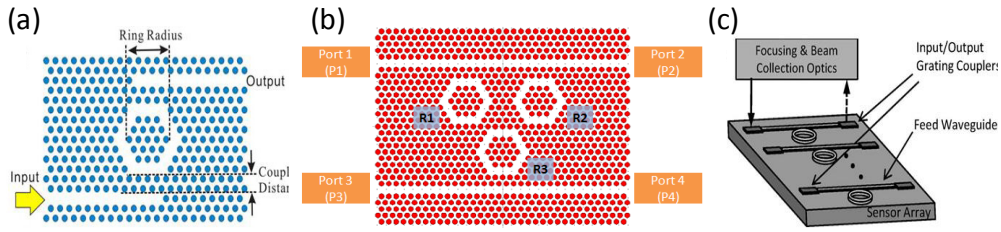

Figure 1.4: (a) Design of DNR based biosensor by Hsiao et al. [43]. (b)Triple nano-ring resonators for biosensing by Ho et al. [48] and (c) waveguides design that are made into an array by Iqbal et al. [46].

In triple nano-ring resonator biosensor, it avoids the use of repeating units as it causes possible interference of results. In addition, cascading designs often increases the complexity of the device, thus complicating fabrication and testing process. In an attempt to alleviate these issues, the PhC based triple-nano-ring resonator is used as a biosensor and its symmetric resonance output and add-drop channel characteristic can be harnessed to enable the detection of multiple biomolecules simultaneously. In addition, the triple nano-ring resonator biosensor is also equipped with a novel function to corroborate the results obtained by reversing the light input and the output.

The use of such optical biosensor also allows small molecules such as single proteins to induce measurable changes in the cavity resonance due to the device's small mode volume and sensor footprint. Optical biosensor also tends

to have much smaller line widths, and very small perturbations can be detected, thereby enhancing the sensitivity of the sensors. A comparison between optical biosensors and other sensors such as mechanical and electrical biosensors are shown Table 1.

Table 1: Performance of various categories of biosensors

Category	Description	Analysis time	Limit of detection	Ref.
Optical detection	Ring resonator	2min	0.6nM	[7]
Plasmonic detection	Surface plasmon resonance	10s	3nM	[49]
Mechanical detection	Microcantilever	10min	15nM	[50]
Electrical detection	Nanowire field effect transistor	10min	10pM	[51]

1.1.2.2 Opto-mechanical sensors

Tuning of the performance of PhC cavities is a popular topic for investigation as it is a key technology of realizing dynamically reconfigurable photonic sensors. Various tuning approaches employing magneto-optic [52-54], liquid crystals [55-57], micro-fluidic [58-60] and electro-optic effects [61-63] have been explored, they face major limitations as they suffer from small tuning range, high power consumption and the lack of certain key but exotic materials needed. Opto-mechanical sensors are receiving unprecedented interests as research and development of microelectromechanical systems (MEMS) gain speed. With the ability to include movable structures into the photonic designs, the idea of tuning PhC cavities was highly anticipated. For example, Chew et al. reported the integration of comb-drive actuators with two PhC nano-beams as shown in Figure 1.5(a) [64]. When a voltage is added to the comb-drive actuators, the gap between the two PhC nanobeams will change as shown in (b).

This changes the resonant condition of the PhC design and hence changes the output wavelength.

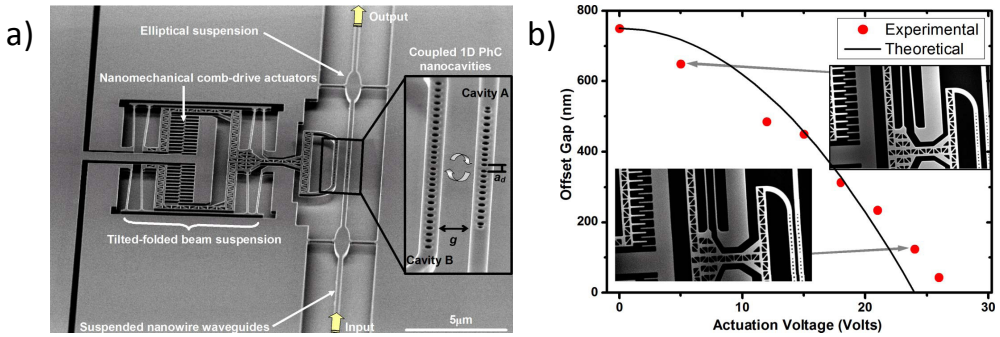

Figure 1.5: (a) SEM image showing the dynamically tunable coupled PhC nanocavities and the submicrometer MEMS driving mechanism and waveguides [64]. (b) Offset gap between the two nanocavities versus driving voltage.

By harnessing this aspect of PhC beams and designing mechanically compliant PhC cavity, the readout of mechanical motion can be optically and resonantly enhanced. Such opto-mechanical sensors have the capability of providing measurements with ultra-high precision at or below the standard quantum limit, which correspond to the position uncertainty of the quantum ground state of the mechanical object [65, 66]. One such application that utilizes opto-mechanical sensor is in the realization of an optical accelerometer [67] as shown in Figure 1.6(a).

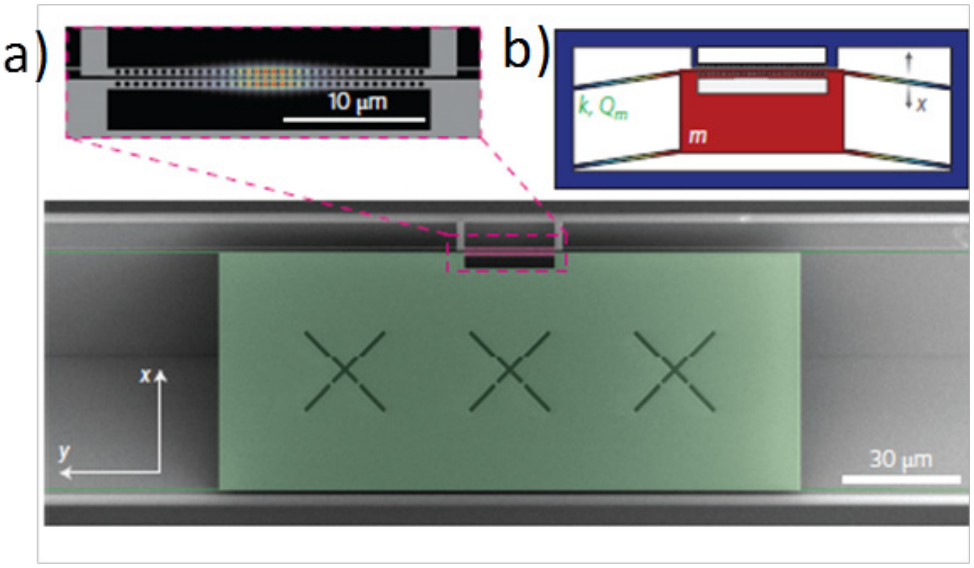

Figure 1.6: (a) False-coloured SEM image of a typical optomechanical accelerometer. The test mass (green) is suspended with springs that allow high oscillation frequencies. The PhC cavities (pink) are fabricated at the top of the test mass. The zoom-in image of the PhC cavities shows the magnitude of the electric field around the optical cavities region. (b) Schematic displacement profile (not to scale) of the fundamental in-plane mechanical mode used for acceleration sensing.

As shown in (a), the optical accelerometer comprises of two parts, namely a test mass (green) and PhC cavities (pink). In order to allow motion with high oscillation frequencies, the test mass is suspended with springs. From the zoom-in image of the PhC cavities which is overlaid with the magnitude of the electric field, it can be seen that the electric field is largely confined within the PhC design. Due to the presence of the strong electric field confinement, the resonant optical wavelength is very sensitive the separation between the two PhC beams. When the test mass moves due to an external acceleration as shown in (b), this alters the separation and causes the change in the output resonant wavelength can be detected. Through this method, the reported measurable acceleration resolution is 10 $\mu g Hz^{-1/2}$ with sub-milliwatt optical power, bandwidth greater than 20 kHz and a dynamic range of greater than 40 dB.

1.1.2.3 Slow light effect

It is common knowledge that velocity of light in vacuum is approximately $3x10^8$ m/s. This ultrahigh speed is advantageous for efficient data transmission between two points that are separated on a global scale or on a single chip. However, the high velocity also makes control of optical signals in the time domain difficult. Slow light is a technology now being investigated as a means to overcome this problem. For sensor applications, slow light provides better performance due to enhanced light-matter interaction [68].

Earlier attempts to create slow light effect was electromagnetically induced transparency (EIT) [69-72] and other methods such as Bragg fiber [73-75] soon appeared. With design flexibility and ultra-low group velocity (v_g), PhC waveguides soon become a common platform to produce slow light and this can be easily done by elongating the cavity defects into a line [68, 76-79]. One of the main issues faced when trying to produce slow light effect in light propagation is the presence of group velocity dispersion (GVD) which leads to degradation of optical signal due to pulse broadening and distortion. To overcome this, structural optimization has been done on PhC lattices to achieve dispersion free slow light over the largest possible bandwidth. In order to quantify the performance of slow light devices, the delay-bandwidth product (DBP) is usually calculated. For example as shown in Figure 1.7, Frandsen et al. have shown that nearly constant group index of 34 over 11 nm bandwidth or a DBP of around 0.241 can be achieved by altering the size of the air holes in the first two rows next to the waveguide channel [80]. More recently, Caer et

al. proposed the idea of altering the PhC waveguide by changing it into a slot with Bragg-like corrugation as shown in (b). With such a design, group indices exceeding 130 and 90 over a bandwidth of 1.5 nm and 2 nm or DBP of 0.126 and 0.116 can be achieved [81].

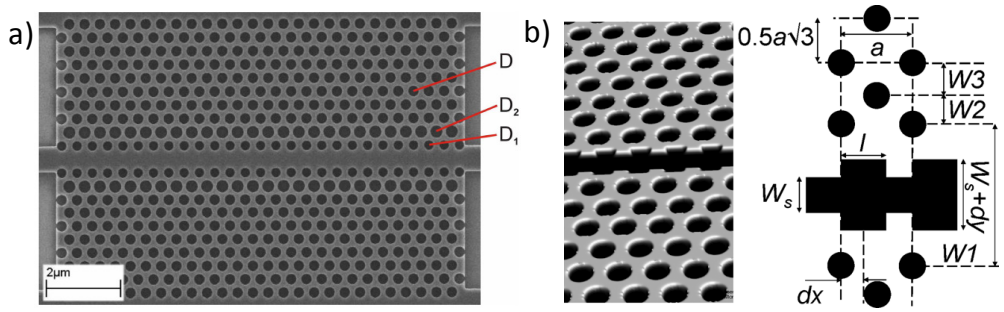

Figure 1.7: (a) Slow light device by Frandsen et al. which has its DBP enhanced by changing the radius of the first two rows of air holes beside the PhC waveguide [80]. (b) Design by Caer et al. which has a corrugated Bragg-like waveguide [81].

1.2 Free-space based optical sensors

For free-space based optical sensors, PhC is investigated as an optical reflector [82-84]. Optical reflectors play an important role in the realization of many optoelectronic devices and photonic elements such as mirrors [85, 86], sensors [87-89] and interferometers [90-92]. As a sensor, it can also be used as a physical sensor for applications such as pressure sensing. Recently, Si PhC has attracted much attention due to its small size and exceptional optical performance. For an easy implementation, most research is based on 1-D PhC reflector or more commonly known as Bragg reflector [93, 94]. It is formed by depositing thin layers of two alternating materials with high and low refractive indices. The larger the difference between the refractive indices of the two materials, the Bragg reflector will display higher reflection. Typical materials used are aluminium oxide (Al_2O_3), titanium dioxide (TiO_2), Si and silicon

nitride (SiN). The thickness of the layers is set to be a quarter of the design wavelength divided by the material's refractive index. Some of the designs by Rissanen et al. are shown in Figure 1.8(a) and (b) [92]. The fabricated device is shown in (c). The small holes that appear are etching holes so that the membrane can be undercut and make the Bragg reflector suspended. From their results, the reflection measured is higher than 80% at their design wavelengths. In order to increase the reflection, more layers of the materials can be deposited.

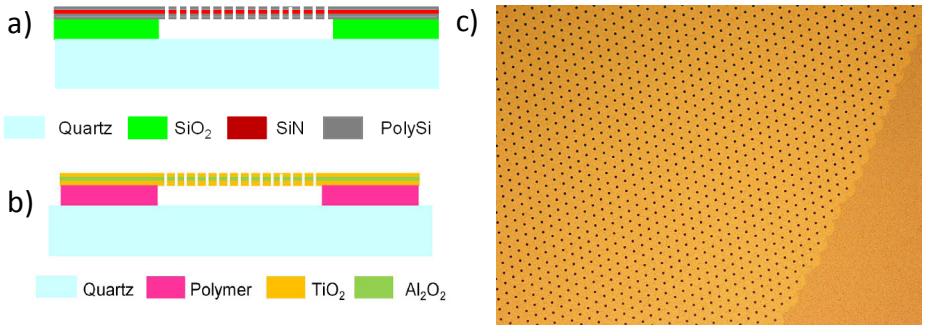

Figure 1.8: Designs by Rissanen et al. which uses alternating layers of (a) Si and SiN and (b) TiO_2 and Al_2O_3. (c) Optical image of the fabricated Bragg reflector [92].

One big issue with Bragg reflector is that as the wavelength increases, the thickness of the optical layers and the total thickness of the Bragg reflector increase. This results in higher stress of the multilayer thin-film stack which increases the risk of cracking during the fabrication process. Sub-wavelength metal gratings have been shown to produce broadband reflection over a large bandwidth but are hindered due to its high intrinsic absorption losses [95-100]. In order to overcome these issues while maintaining high reflection, 2-D PhC reflector emerges as a good candidate and it has receives intense research interest. This is because 2-D PhC reflector has been shown to display Fano resonance which is a characteristic of extremely high reflection. With proper

designed parameters, high reflection can practically be achieved across different frequency regions. 2-D PhC based single layer membrane devices have been reported by various groups for their high reflectivity in the optical communication applications, i.e., relevant wavelength of about 1550 nm [83, 101-105], as well as in the mid infrared (MIR) and far infrared (FIR) wavelength region [106-110] as shown in Figure 1.9. These reports show the potential of PhC membranes in practical applications.

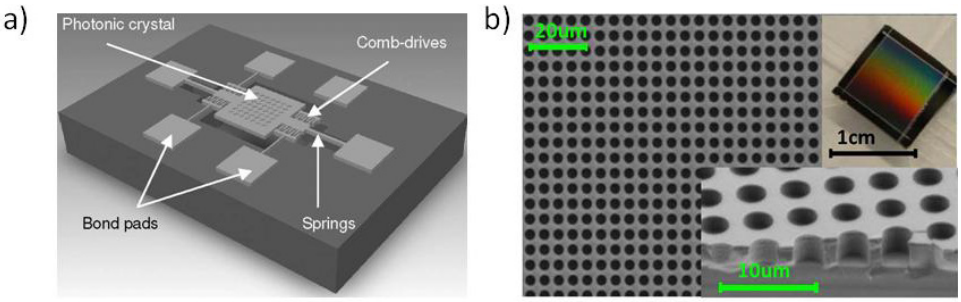

Figure 1.9: (a) PhCs based scanning working at wavelength of 1550 nm [101] and (b) PhCs reflector aimed to work in FIR wavelengths [106].

There is however a lack of the investigation in using polycrystalline Si for the formation for such PhC membrane. This is mainly due to the challenge of the stress present in the membrane which usually causes bulking [35, 36] and even cracking. An attempt to achieve a free-standing polycrystalline Si PhC membrane was done by Kim et al. in the near infrared (NIR) range [111] as shown in Figure 1.10. In order to alleviate the stress present in the polycrystalline Si membrane, the authors use tensile stressed silicon nitride for stress compensation. However, such techniques require good matching between the stress in the PhC membrane and SiN, which is difficult in typical deposition processes.

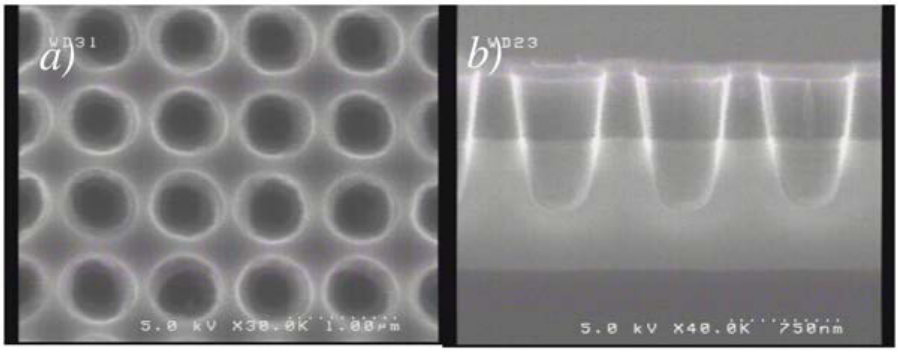

Figure 1.10: Free-standing polycrystalline Si PhC membrane by Kim et al. in the NIR range [111]. The stress in the Si is compensated by a thin layer of SiN on top.

Such PhC reflector can be used for physical sensing such as pressure by Wu et al. as shown in Figure 1.11 [112]. When a pressure is applied from the bottom of the diaphragm, it will push the PhC design upwards towards the fiber. This reduces the distance between the PhC top surface and the fiber and causes a shift in the reflection wavelength. The resolution of the pressure sensor based on this method is reported to have a spectral shift sensitivity magnitude of up to 8.6 nm/kPa.

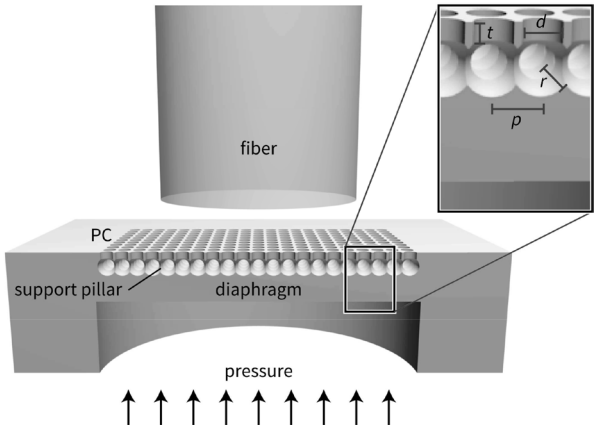

Figure 1.11: PhC reflector based pressure sensor by Wu et al.

One major application of highly reflective surfaces is in the formation of Fabry-Perot filter (FPF) where two highly reflective surfaces are placed parallel to each other. The gap between the mirrors is designed to be nλ/2, where n is an

integer and λ is the desired filtered wavelength, in order to achieve constructive interference of the desired wavelength. The gap between the two highly reflective surfaces can be tuned by incorporating MEMS technology. Such tunable filters are extremely important in applications like gas sensing [113, 114] and hyperspectral imaging [115, 116]. Many attempts in recent works use Bragg reflectors with the high reflectivity to realize the FPF [114, 115, 117-119]. However, the Bragg reflectors are typically heavy and require high actuation voltage to achieve tunability. As mentioned before, when working at longer wavelengths, the thickness of the layers has to be increased and this complicates fabrication. Suh et al. introduced the idea of using 2-D PhCs as the reflective mirror and proved theoretically the high performance of such FPF [120].

MIR photonic has recently attracted tremendous attention due to its potential for industrial applications as well as rapid improvement in MIR laser technologies. MIR spectroscopy, in particular is an extremely powerful technique that can be used for chemical and biological sensing in environmental monitoring and medical diagnosis [121-123]. For example, as shown in Figure 1.12, MIR wavelengths from 3 μm to 6 μm are particularly important for gas sensing [124]. In order to sense these gases through spectroscopy, it is important that the input light has only the wavelength that the gas absorbs. This is usually realized through the output of the FPF. By using 2-D PhC reflectors in the FPF, their high Q-factor output would allow for a more sensitive and higher resolution sensing.

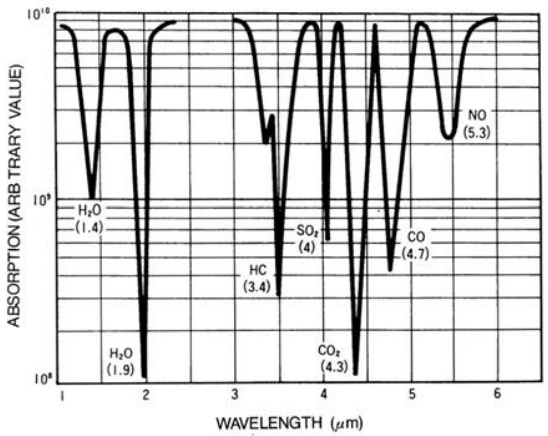

Figure 1.12: Infrared absorption dips for common gases of environmental concern.

Current effort to realize FPF also typically involves bonding of the mirrors as shown in Figure 1.13(a) or the use of non-CMOS compatible materials such as polyimide as sacrificial material to define the cavity length [114-118]. In addition, more exotic materials such as lead chalcogenide and europium(II) telluride might be needed for the formation of the mirror used in the FPF as shown in (b). The Q-factors of the filtered peak by current reports of FPF are typically few tens and using PhC reflector as mirrors is deemed to be a method to increase the Q-factor more sensitive and higher resolution applications as shown in Table 2. More details on our work on PhC based FPF will be given in Chapter 5.

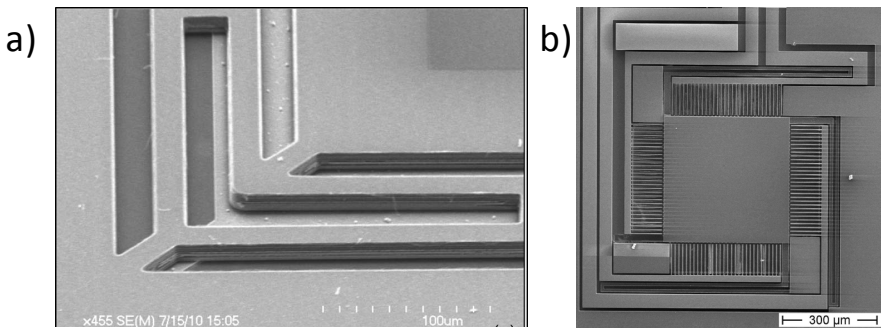

Figure 1.13: (a) An FPF that is formed through the use of bonding of the top and bottom mirror and (b) shows a FPF that uses more exotic materials.

Table 2: Comparison of Q-factors between various FPF designs

Institutes	Design	Q-factor	Remarks	Ref.
Space and Naval Warfare Systems Center Pacific, USA	Si and SiO2 multilayers mirrors	< 100	Bonding of two chips to achieve dual plates	[118]
University of Western Australia, Perth, Australia	Ge, SiO and SiN multilayers mirrors	< 100	Bonding of two chips to achieve dual plates	[125]
Institute of Mechanical Systems, ETH Zurich. Switzerland	chalcogenide and EuTe multilayers mirrors	Few hundreds	Bonding of two chips and use of non-CMOS materials	[126]
Our work	Si PhC based mirrors	300	Monolithic process	-

In summary, Table 3 presents some of the benefits and advantages of harnessing optical sensors in the various applications. It also highlights some of the challenges and disadvantages. Generally, the use of optical means helps to enhance the sensitivity of the sensor while providing small footprint. However there are several disadvantages and challenges that has to be overcome in order to fully implement such optical means in the various applications.

Table 3: Advantages and disadvantages of optical sensors

Applications	Advantages	Disadvantages
Optical biosensor	• Small footprint • Enhanced sensitivity • Very low limit of detection	• Require the use of surface functioning for binding of biomolecule
Optical accelerometer	• Small footprint • Fast readout • Extremely high sensitivity	• Only one axes of measurement per device
Optical pressure sensor	• Small footprint • Fast readout • Extremely high sensitivity	• Require diaphragm that is delicate and fragile • Need bonding with optical fiber
Optical MIR gas sensor	• Fast readout • Label free sensing • High sensitivity • Low power	• Require long absorption length • Precise alignment of optical components

1.3 Material choice for photonics

While Si photonics have been studied in the NIR wavelengths for many years, they have also been investigated as passive devices to be used in new mid-IR wavelength band for applications including optical communication, datacom and sensing through photonics devices including resonators, demultiplexers, waveguides, modulators, etc. in recent years. [127-129] So far, patterning high-quality single crystal Si to form Si photonics from the device layer of silicon-on-insulator (SOI) 8" wafers is the mainstream manufacturing process. However, in order to realize multiple photonic layers to be integrated onto CMOS ICs for future generations of all photonic ICs, Si is found to be an impractical choice as high-temperature processing is necessary to get defect-free Si-layer. More importantly, the lack of strong non-linearity property in Si also limits its ability to generate additional frequencies from the original input wavelength. Frequency comb which is the current method used to generate multiple output wavelengths from a single input wavelength requires non-linear optical properties where Si does not have. This restricts the entire Si photonics ICs to be only operated at the wavelength provided from the input terminal. As power consumption scales with the number of sources, it is impractical to have multiple light sources, i.e., multi-wavelength, in a single device, thus preventing the use of multi-channel design which is important for densely integrated OEIC.

On the other hand, aluminium nitride (AlN) is a CMOS-compatible insulating piezoelectric thin film material which can be prepared by sputtering process at low temperature. To provide good crystalline structure of AlN film with sound

piezoelectric characteristics, AlN film needs to be deposited on top of low-temperature deposited molybdenum (Mo) electrode, a CMOS-compatible refractory metal, by sputtering. In addition to the advantages of AlN film in terms of process and piezoelectric characteristic, AlN is an optical material with sound non-linearity which is a desired feature for tunable photonics. Si has negligible non-linearity effect, while the Pockel's coefficient and Kerr's coefficient of AlN is comparable to SiN (Table 4[130-133]).

Table 4: Properties and Status of CMOS photonic materials, Si and AlN

Material	Workable wavelengths	Thickness for 1.55 µm wavelength	Pockel's Coefficient (pm/V)	Kerr's Coefficient (cm^2/W)	Piezoelectric Coefficient (pC/N)
Si	1 - 8.5 µm	0.22 µm	Nil	$1.5x10^{-14}$	Nil
SiN	0.1 - 7 µm	0.55 µm	0.04 [130]	$2.5x10^{-15}$ [131]	Nil
AlN	0.2 - 13.6 µm	0.5 µm	1 [132]	$2.3x10^{-15}$ [133]	1.7[132]

Table 4 also indicates the workable wavelength range (0.2 µm to 13.6 µm) for AlN, which is much wider than Si. More importantly, Si does not possess piezoelectric property, and hence lacks one dimension of tuning in photonics. The refractive indexes of AlN and Si are 2 and 3.42, respectively, and the desired thin film thickness for optical waveguide used in 1.55 µm optical signals is 0.5 µm and 0.22 µm for AlN and Si. This is within the capability of current sputtering AlN technology which can provide low-stress AlN film for up to 3 µm thickness. Because of its process advantage and wide electrical bandgap, AlN is a promising CMOS material for both near and mid-IR applications. Together with AlN's optical non-linearity, AlN offers more flexibility so as to complement Si by fulfilling the technological gap of Si as photonics material.

1.3.1 Non-linearity tuning in AlN photonics

The non-linearity phenomenon is referring to polarization, **P**, as a function of the input electric field, **E**:

$$\boldsymbol{P} = \varepsilon_0 \chi^{(1)} \cdot \boldsymbol{E} + \varepsilon_0 \chi^{(2)} : \boldsymbol{EE} + \varepsilon_0 \chi^{(3)} \vdots \boldsymbol{EEE},$$

where ε_0 is the intrinsic permittivity, $\chi^{(1)}$ is the electrical susceptibility, $\chi^{(2)}$ is the Pockel's coefficient and $\chi^{(3)}$ is the Kerr's coefficient.

The presence of non-linearity in AlN opens up applications that are not ideal if Si is used. For instance, the presence of Kerr's coefficient in both Si and AlN enable them to be used for frequency comb generation. For Si, Griffith et al. have demonstrated the use of an etchless process for Si photonics for MIR frequency comb generation as shown in Figure 1.14 [134]. Although the ring resonator is doped, the performance of the device is still of high Q-factor and the propagation mode well maintained within the optical waveguide.

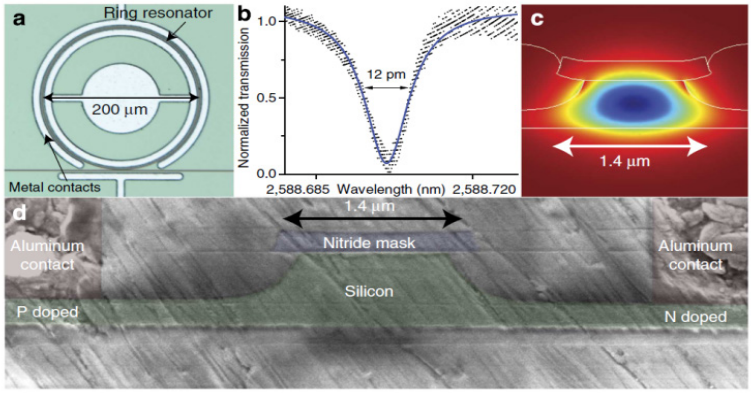

Figure 1.14: (a) Optical microscope image of a ring resonator and metal contacts fabricated. (b) Normalized transmission spectrum taken at low-input power, with an intrinsic quality factor of 590,000. (c) Simulated optical mode at 2.6 mm, showing high-modal confinement in Si. (d) False coloured cross-sectional SEM image of silicon waveguide, doped regions and metal contacts.

Measurement of the device by Griffith et al. reveals generation of a frequency comb, but its performance is largely hindered by the presence of free carrier

absorption. This causes only a few lines to be generated as shown in Figure 1.15(a). In order to maximize the performance of the frequency comb generation, a reverse bias is needed as shown in (b). The reverse voltage for peak performance is 10V.

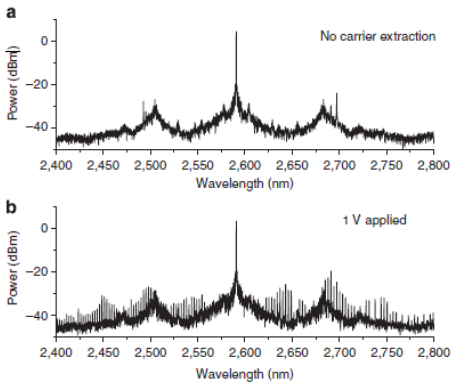

Figure 1.15: (a) When the pump set at a fixed wavelength and the voltage source off, only a few lines are generated near 2,500 and 2,700 nm at this detuning. (b) By applying even a small voltage in reverse bias to the junction, hundreds of comb lines across the spectrum can be generated.

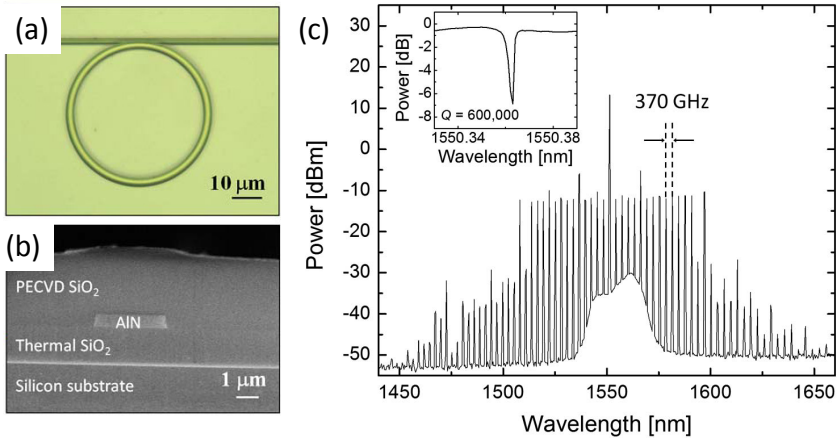

Figure 1.16: (a) Optical micrograph of the microring. (b) Scanning electron micrograph (SEM) of the cross section of the fabricated AlN waveguide. (c) Frequency comb generated from microring resonator.

Likewise to Si, AlN with a non-zero Kerr's coefficient can be used for comb generation. However, a reverse bias is not needed in AlN to remove free carrier absorption, hence reducing the power consumption of the device. Jung et al. [133] has demonstrated using an AlN based ring resonator as shown in Figure

1.16(a) and (b). The frequency comb has a FSR of 370 GHz as shown in (c). The presence of Pockel's coefficient in AlN allows it to have an edge over Si in non-linearity applications as Si has a zero Pockel's coefficient due to its centrosymmetric crystal structure. By inducing Pockel's effect in AlN, Xiong et al. has shown electro-optic tuning in AlN for modulating signals [132]. A simple ring resonator design is used as shown in Figure 1.17(a) and electric pads can be included to introduce electric field to the device as shown in (b). With the application of voltage bias from -7.5V to +7.5V, the authors illustrated the excitation of Pockel's effect which enables a tuning range of 8pm to the resonance wavelength, as shown in (c).

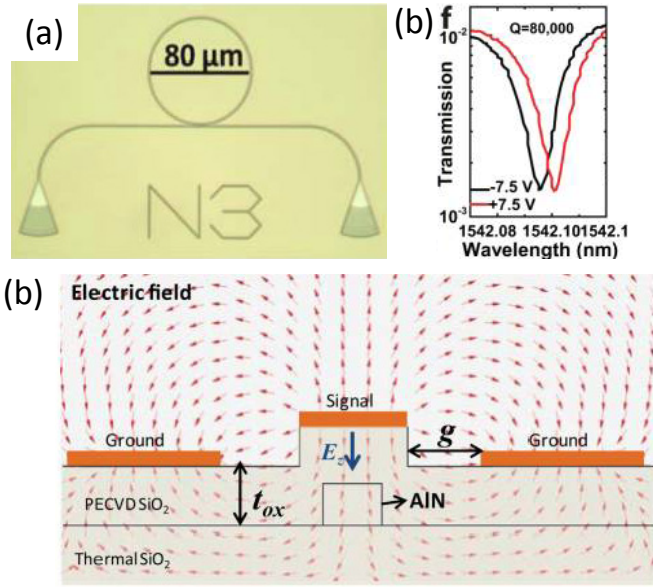

Figure 1.17: (a) Optical micrograph of the microring. (b) The numerically calculated electric field distribution induced by the ground−signal−ground electrodes. The arrows denote the direction of the applied electric field.. (c) A ring resonance near 1542.10 nm with an extinction ratio of 10 dB and quality factor of 80 000 is tuned 8 pm by applying bias from −7.5 V to +7.5 V.

1.3.2 Piezoelectric tuning in AlN photonics

Piezoelectric tuning is also a tuning mechanism that is possible with AlN since it is a piezoelectric material with a piezoelectric coefficient of 1.7 pC/N [132]. Suspended piezo-electrically controlled movable part such as cantilevers and ring resonators can be used in optical designs to tune or modulate the output signal. A photonic design can be made tunable by connecting it to an actuator design using AlN with the appropriate interdigital transducer (IDT) pads [135, 136] as shown in Figure 1.18. The piezoelectric nature of AlN allows the excitation of phononic output through the use of IDT designs for surface acoustic wave [137] and lamb wave resonator [138]. By applying a voltage difference to the IDT, the AlN actuator will bend and bring the released portion of the ring resonator along. This causes changes in the propagation length in the ring resonator and the intensity at the resonance wavelength. Likewise, as shown in (b), IDT can also be used to tune the resonance condition of a nanocavity even when the device is not released. The piezoelectric property in AlN allows the performance of the photonic components to be tunable [139, 140]. This creates the opportunity to realize a more creative methodology for light manipulation in future photonics research. Such tunability also relaxes the stringent requirement in fabrication since such tunability can be used to mitigate process variations.

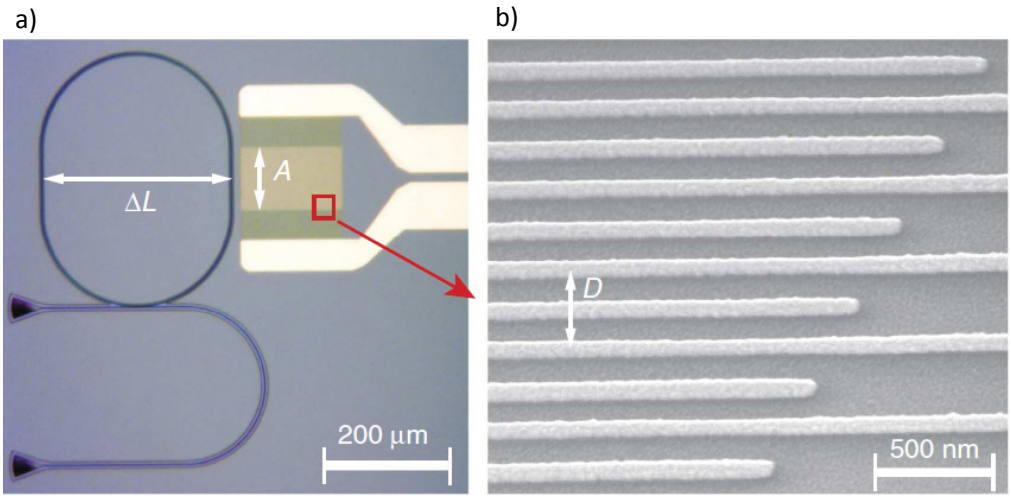

Figure 1.18: (a) Optical microscope image of a device which has its nanocavity in close proximity to an IDT. (b) Design of IDT for structural deformation to achieve tuning [136].

By offering tunability that is not possible in Si, AlN offers a platform that has flexibility in its design not seen before. At current stage of research, AlN is the only CMOS compatible material that offers both non-linearity and piezoelectric tuning. This promises an optical material with high optical performance while benefiting from current CMOS foundry capabilities.

1.4 Thermo-optic effect

Thermo-optic effect is a well-known phenomenon where the optical property, namely refractive index, of a material varies with temperature change. In the case of down-hole oil drilling where high operation temperature is expected, thermo-optic effect has to be taken into account for design optimization. Numerous works have been done recently to characterize the impact of temperature change on the optical performance of photonic devices [141-144]. The change in peak reflection wavelength of the PhC membrane due to thermo-optic effect of polycrystalline Si is quantified by

$$\Delta\lambda = \Delta T \left(\frac{\lambda_0}{n_0}\right) \left(\frac{\Delta n}{\Delta T}\right), \quad (1)$$

where n_0 is the refractive index at 25°C, $\Delta n/\Delta T$ is the thermo-optic coefficient and ΔT is the temperature change.

Through greater understanding of the thermo-optic effect, efforts are also done to harness the effect for applications like optical switch, optical filters and temperature sensors [145-149]. However, in applications where thermo-optic effect is undesirable, such temperature effect on the optical performance has to be compensated [150-152]. A common method to compensate thermo-optic effect is the use of a material, typically polymer, which has negative thermo-optic coefficient as shown in Figure 1.19(a) [153]. The negative thermo-optic coefficient of the polymer will cancel the thermo-optic effect that is induced in the Si waveguide. In other words, when the temperature increases, the refractive index of Si will increase. This increase will be offset by the decrease in the refractive index of the polymer coating around the waveguide. By considering the refractive index that the light is subjected to, there is no net change in the effective refractive index. However such method faces the problem of integration with CMOS process, as well as reliability concerns due to high sensitivity on the polymer thickness. Other methods such as the use of MEMS structure to induce a wavelength shift that is opposite to the shift induce by the temperature change as shown in (b) [154]. When there is a temperature increase in the working environment, the refractive index of Si will increase and the resonance wavelength of the ring resonator will increase. At the same time, the bi-material cantilever which is made of Si and Al_2O_3 will bend upwards. This is due to the higher coefficient of thermal expansion of Al_2O_3 than Si. The

bending away of the cantilever from the ring resonator causes a decrease in the refractive index that the propagating light faces within the waveguide. Together with the increase in refractive index of Si due to the temperature change, the movement of the cantilever counteract any net effect, hence producing an athermal structure. Once again, such method faces the problem of possible inaccuracy when correcting the thermal effect through mechanical structure. In addition, it requires complex and risky fabrication process. In view of these problems, it is largely desired to have a CMOS compatible material to be used as the photonic device and also achieve high independence from operating temperature changes.

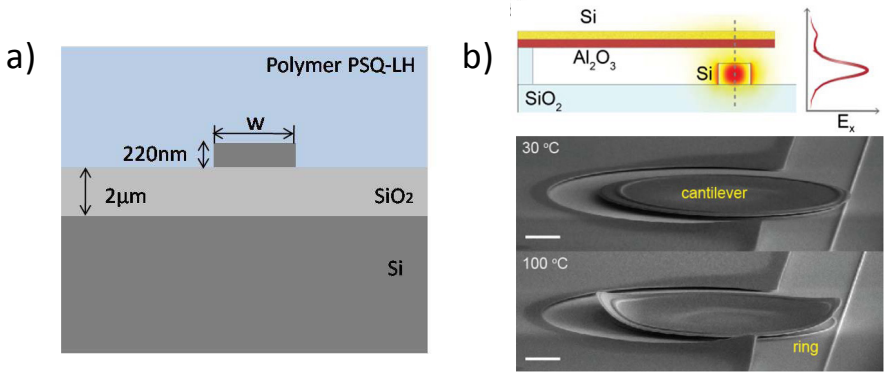

Figure 1.19: Methods to compensate thermo-optic effect by using (a) polymer and (b) MEMS structure.

1.5 Motivation

The primary focus of this work is to develop photonics, in particularly PhC designs, for both in-plane and out-of-plane applications. For in-plane design, the design, fabrication and characterization of a PhC waveguide will be examined in great detail. An attempt to improve the DBP of the slow light effect of a PhC structure will be done by changing the circle air holes into elliptical air holes. In addition, typical methodology like displacing the rows of the air

holes to enhance the performance will also be included in order to obtain a more robust result. We will also move on to examine the performance of in-plane PhC designs using AlN as the main optical material as preliminary work which will help lay the foundation for more sophisticated photonic designs. A simple AlN bus waveguide will be used to couple to a 1-D PhC design which has a cavity defect. The effects of fabrication challenges like sloping sidewall and AlN's relatively low refractive index will be examined.

For the out-of-plane photonics, the development of PhC reflectors will be presented first. This includes designs through the use of simulations, fabrication and characterization. In particular, this work will focus on MIR wavelengths which were identified to be extremely useful wavelengths for sensor applications such as spectroscopy. In applications such as ruggedized electronics, the devices will face high temperatures during their operation. In order to characterize the change in performance, the PhC reflectors are measured at temperatures that varies from room temperature to 450^{o}C. As the thermo-optic effect causes drastic change in the peak wavelength, this work seeks to find a way to overcome this effect in Si through design compensation. A more thorough way of reducing thermo-optic effect is done through the use of AlN as an alternative material as its refractive index displays very low changes with fluctuating operating temperatures. The thesis will also describe the application of PhC reflectors in forming a FPF. A monolithic fabrication process will be introduced in order to avoid difficulties faced in bonding. The fabricated FPF will be characterized and its suitability for high resolution

applications such as imaging and spectroscopy will be examined.

1.6 Organization of thesis

In accordance with the motivation and objective of the current work to explore and develop optical based sensors using guided wave and free-space propagation of light to enhance the sensitivity of sensors and make PhC a possible solution for many sensing needs, this thesis is divided into six chapters and they are organized as below:

Chapter 1 presents the introduction of photonic designs for both in-plane and out-of-plane applications and how they are used in sensor applications. On top of that, it presents the possibility of using alternative material, AlN, as it promotes several advantages. The reasons for using MIR in photonics is also offered. It also introduces the motivation and objective of the work presented in this thesis.

Chapter 2 follows the details of modelling methodology and various testing setups that are used in the in-plane and out-of-plane characterization of the photonic designs.

Chapter 3 presents a novel design of PhC waveguide which contains elliptical air holes in order to enhance its DBP. The fabricated device is also characterized and the slow light effect of the device is quantified through examination of its transmission spectrum. AlN photonics using a simple AlN bus waveguide to

couple to a 1-D PhC design with a cavity defect will also be characterized. From this work, we verify the possibility of using AlN as an optical material despite our fabrication limitations.

Chapter 4 presents our design, fabrication and characterization of PhC reflectors. We investigated the performance of PhC reflectors with two shapes of air holes, namely circle air holes and square air holes. The performances of these two types of PhC reflectors are compared. In addition, the thermo-optic effect of Si is also examined and an attempt will be made to compensate such drift in peak reflection wavelengths. In order to further alleviate temperature issues and create a more robust device, AlN based PhC reflector is also introduced.

Chapter 5 features the extension to PhC reflectors by form a FPF through the formation of two PhC reflectors in parallel to each other with an air gap in between. This work introduces a monolithic fabrication flow and measurement of the fabricated FPF reveal a high performing filter device with a transmitted peak which has a Q-factor that is an order of magnitude higher than existing works.

Chapter 6 presents the conclusion of this thesis and present some recommended future works. Both extension of current effort, like the designing of actuators to be integrated with FPF and initial exploration of PhC devices in the terahertz (THz) frequencies are presented.

CHAPTER 2: Modelling Methodology and Testing Setups

2.1 Photonic crystal simulation

It is commonly known that PhCs based resonators provide very low bending loss due to good optical confinement. They are different from Si slab waveguide, which is based on total internal reflection principle as the confinement method of the light. Instead, confinement of light within PhCs is based on PBG which is created by their unique structures. In PhC, patterns typically include the formation of air holes in Si or Si pillars. This induces an alternating variation of dielectric properties which is responsible for the formation of the PBG. To characterize the frequency response of the PhC structure, it was found that calculation is only needed for the First Brillouin Zone. The results are then applicable to the whole structure since it is periodic. This is the basis for the calculation of the frequency response using the method known as plane wave expansion (PWE) [155]. Several commercial programs, like Rsoft and MIT Photonic Bands are available for such simulations work.

For a full characterization of the electromagnetic wave propagation in the Si slab, finite-difference time-domain (FDTD) method is typically used in modelling. For such simulations, commercial programs like Lumerical, are also available. FDTD calculation, while being accurate, is however very time-consuming and memory intensive. In order to reduce the computation time while not reducing accuracy, 2-D FDTD calculation is often employed rather

than 3-D calculation. M. Kitamura et al. and M. Belotti et al. have both reported that the cavity modes obtained by PWE method and FDTD method in PhCs slab structure are in good agreement with the measured results [156, 157].

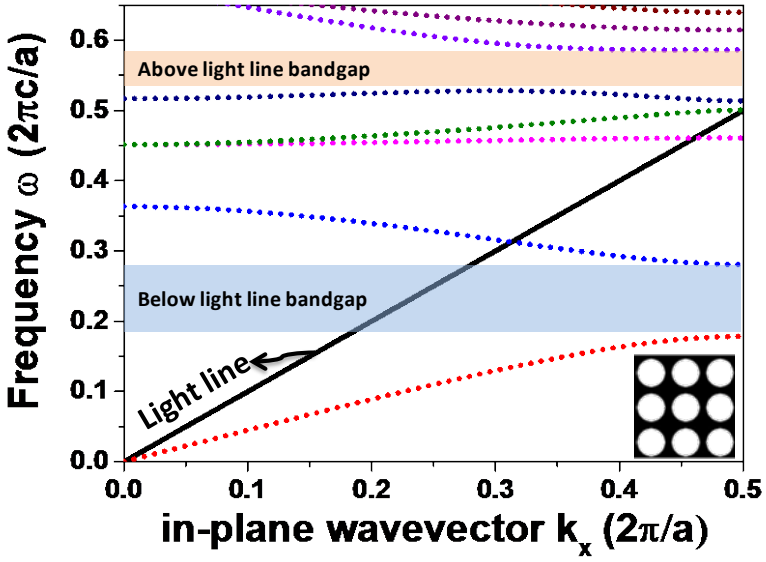

Figure 2.1: Band structure of PhC design.

For example, through the use of PWE method by the program MIT Photonic Bands, the band structure of a silicon PhCs slab with square lattice of air holes is derived and shown in Figure 2.1. The ratio between the radius of the holes (**r**) and lattice constant (**a**) is selected as 0.395. According to the derived photonic band structure diagram, there are two photonic band gaps which ranges from normalized frequency range of photonic 0.192(2πc/**a**) to 0.275(2πc/**a**) and 0.528(2πc/**a**) to 0.587(2πc/**a**). An important element of the band structure is the light line. For bands and bandgaps below the light line, they refer to in-plane guided modes, which are completely confined by the slab without any coupling to external radiations. The bandgap region as shaded in blue indicates the frequency range that is not allowed to propagate within the PhC design. This concept is used in in-plane photonic design like PhC waveguide in Chapter 3.

For bands and bandgaps above the light line, it indicates that the PhC is in radiation modes which allows or restricts coupling from free-space illumination. The band gap region as shaded in red indicates the bandwidth within an out-of-plane illumination that will be reflected as it cannot coupled into the PhC slab. This concept is used in our work on PhC reflector described in Chapter 4.

2.2 Testing setups

2.2.1 In-plane photonic measurement setup

For in-plane photonic measurement which is in the NIR wavelengths from 1470 nm to 1630 nm, the input light with a fixed wavelength is generated from a tunable laser source and guided by polarization maintenance (PM) fiber. In order to couple the guided light from the fiber to the device, there are two kinds of coupling mechanisms. The general setup of an in-plane photonic measurement setup is shown in Figure 2.2. Light input is supplied by continuous wave (CW) tunable laser sources, model 81940A and 81960A by Keysight Technologies. The input light is then coupled into a PM optical fiber to the device. In order to obtain the high precision alignment needed, both the chip and fiber are both placed and locked on optical nano stages. The output signal is collected into another fiber which is connected to an optical spectrum analyzer (OSA), model 86142B from Keysight Technologies, which collects the optical data. These data can be input to a computer for more detailed data analysis.

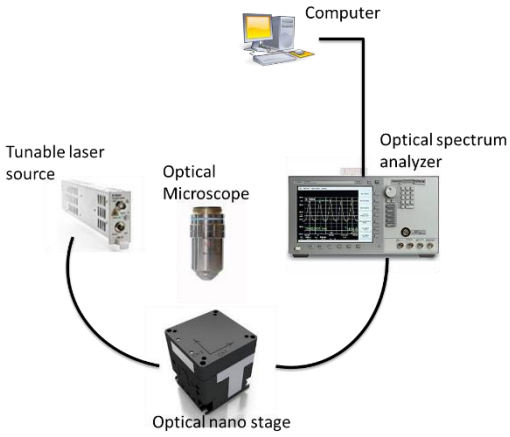

Figure 2.2: General setup of an in-plane photonic measurement.

The setup that is used is shown in Figure 2.3. The wavelength range provided by the sources is from 1465 nm to 1630 nm with a minimum wavelength step of 0.1 pm and the maximum power output is 30 mW. Both an OSA and optical power sensor are used in the collection of optical signals. The fibers and the device are placed on optical nano stages which are controllable in six-axis and have sub-micron minimum tuning steps. The alignment stages provide coarse tuning travel distance of 13 mm with a resolution of 10 μm/div. The fine tuning travel distance is 0.6 mm with a resolution of 0.5 μm/div. The total rotation angle is up to 6°. The polarization of the input light is controlled by manual fiber three paddle polarization controllers, model FPC032 from Thorlabs.

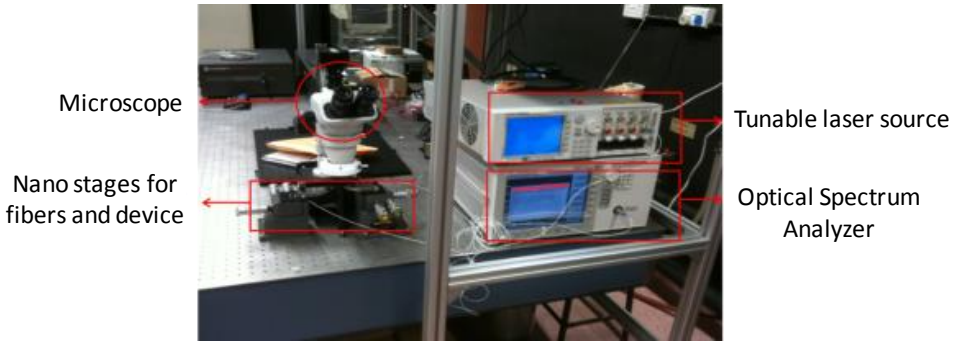

Figure 2.3: In-plane photonic measurement setup used.

During the measurement process, the chip and fibers are placed in line with the

waveguides on the chip. A fiber is first connected to the tunable laser source and the other end of the fiber is directed towards the waveguide on the device. An optical microscope is placed orthogonally on top of the fiber and is used to monitor the X and Y directions of fiber alignment with the waveguides. For alignment in the Z direction, an infrared camera with a 20x infrared lens is used at the output of the waveguide instead. When the input fiber and the waveguide are aligned, the infrared camera will capture a light spot of the input light from the waveguide. Any movement in the input fiber from this position will cause the light spot to disappear as the light spot is only able to transmit to the other side of the device through the waveguide. Once this is achieved, the infrared camera is removed and replaced with the output fiber which is connected to the power meter. Alignment of the output fiber to the waveguide is achieved by maximizing the power transmitted to the power meter.

The other in-plane photonic measurement setup involves the use of grating coupler. As the waveguide of the device does not terminate at the edge of the chip, we will not be able to use the previous method. Instead, we use a fiber array as shown in Figure 2.4(a) to introduce the light to the device. PM fibers are locked in position into several V-grooves that are fabricated on a transparent substrate with certain constant spacing, which is 127μm in our design. The fibers are arranged in accordance to their polarization with two fibers in the Transverse Electric (TE) orientation and two fibers in the Transverse Magnetic (TM) orientation. A transparent lid is then sealed on top of the PM fiber array to fix the whole structure without damage as shown in (b). The array surface is polished to 25^{o} in order to achieve a large enough clearance space to avoid

contact between the base of the fiber array and the device when performing alignment as shown in (c). With a sufficient clearance, the coupling angle, $Ø_{coupling}$ can be adjusted to be around 12^o which is the optimal angle of incidence to the grating coupler for maximum coupling.

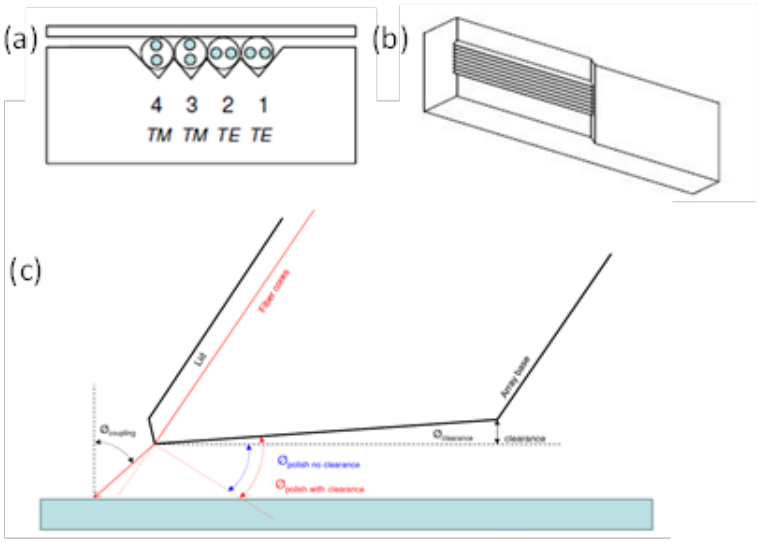

Figure 2.4: (a) and (b) Fiber array used for in-plane photonic measurement which is placed in a transparent lid. (c) Cross-sectional view of fiber array when aligned with device during measurement.

Only one optical nano stage is needed in this setup to control the fiber array. The fiber array is aligned orthogonally to the surface of the chip. In order to monitor the alignment condition of the fiber array and the device, a universal rotatable stereo optical microscope is used at 45^o to the chip surface, as shown in Figure 2.5. As the grating surface can be designed to be much larger than the waveguide's cross-sectional area, the alignment of the grating coupler is much easier than fiber based coupling method. In summary, both coupling mechanisms are used in this work and have been successfully tested in experiment.

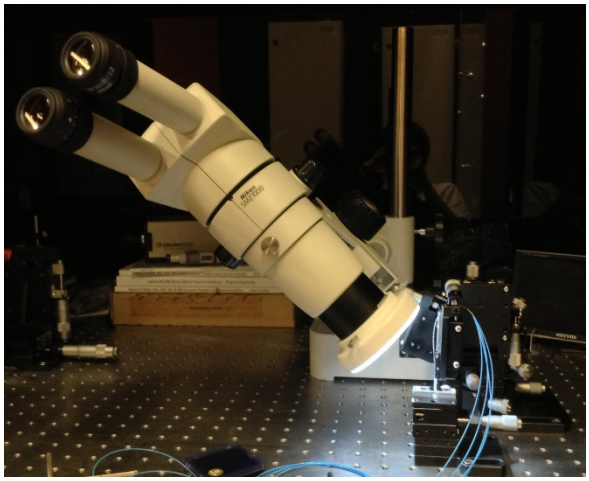

Figure 2.5: Experimental setup used for aligning fiber array to the device.

2.2.2 Out-of-plane photonic measurement setup

For out-of-plane photonic measurement, the interested wavelength range is in the MIR region around 3.55 µm. The main equipment used in this measurement setup is the Agilent Cary 660 Fourier-transform infrared spectroscopy (FTIR) spectrometer as shown in Figure 2.6. The infrared source is a ceramic heater which has a spectral range from 1 µm to 0.34 mm. The interferometer is used for the analysis of the light to obtain the optical properties associated with the target device. A portion of the light source is transferred to the interferometer and the other portion is directed to the sample. This is done through the calcium fluoride (CaF_2) beamsplitter which has negligible absorption from 0.55 µm to 8.33 µm. Detection of the response of the sample is done through a Mercury Cadmium Telluride (MCT) detector which has a spectral range from 0.8 µm to 22 µm. The MCT detector is a common component used for the detection of MIR wavelengths due to its large spectral range and high quantum efficiency. However, the main drawback of MCT detectors is that the detector needs to be cooled to temperatures near that of liquid nitrogen (77 K), to reduce noise due

to thermally excited current carriers. By examining the entire optical path, the infrared signal will go through several components that have different spectral ranges. The eventual spectral range detectable is the overlapped workable wavelength which is from 1 μm to 8.33 μm. As the energy output from 1 μm to 2 μm is low, the more reasonable working spectral range from 2 μm to 8.33 μm.

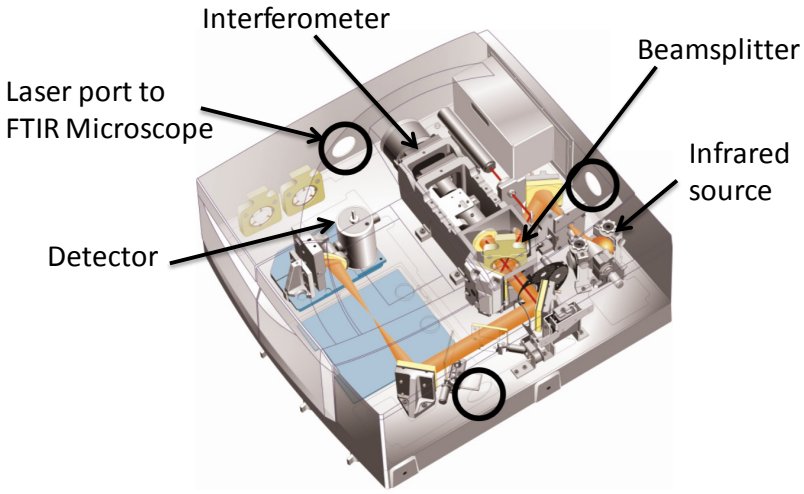

Figure 2.6: Agilent Cary 660 FTIR Spectrometer.

While the Cary 660 FTIR spectrometer is powerful as MIR equipment, the limitation is the large spot size that will incident on the sample. The typical size of the MIR spot is around 2 mm in radius. This is too big for our samples as the interested areas are usually around few hundred micrometers wide. Hence in order to reduce the spot size, the Cary 660 FTIR spectrometer is connected to the Agilent Cary 620 FTIR Microscope. The MIR source is from Cary 660 FTIR spectrometer and is fed to the FTIR microscope though the laser port. The FTIR microscope is shown in Figure 2.7. The FTIR microscope has the flexibility to do both reflection and transmission measurements. The MIR signal is captured by either a MCT detector or a focal plane array (FPA) detector. The FPA detector has 32 by 32 detectors which has sizes as small as 5 μm by 5 μm. This

means that the FPA detector is able to create an MIR spectra image. The only downside to this method is the amount of time needed for each data acquisition due to the increased amount of data computation. Both these detectors will be used in this thesis.

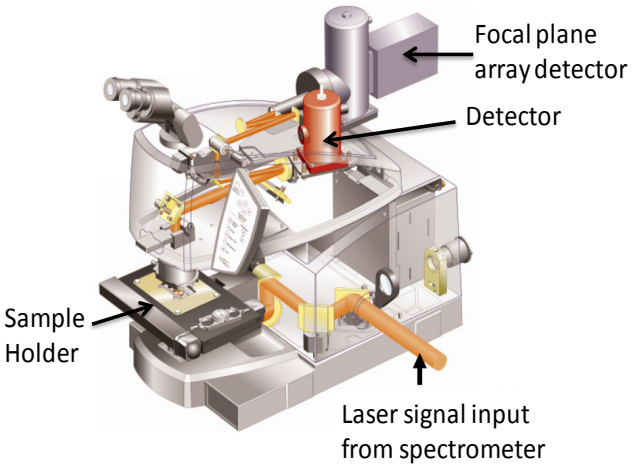

Figure 2.7: Agilent Cary 620 FTIR Microscope.

The physical connection of the Cary 660 FTIR spectrometer and the FTIR Microscope is shown in Figure 2.8. The spot size of the beam emitted by the FTIR microscope is controllable from 50 by 50 μm^2 to 250 by 250 μm^2. In order to obtain maximum energy throughput from the device, the spot size is fixed at 250 by 250 μm^2. For reflection measurements as shown in the inset, the measured reflectance is normalized against a gold sample which is assumed to have an almost perfect reflectance across the MIR wavelengths [158]. For transmission measurements, the measured transmittance is normalized against free-space instead.

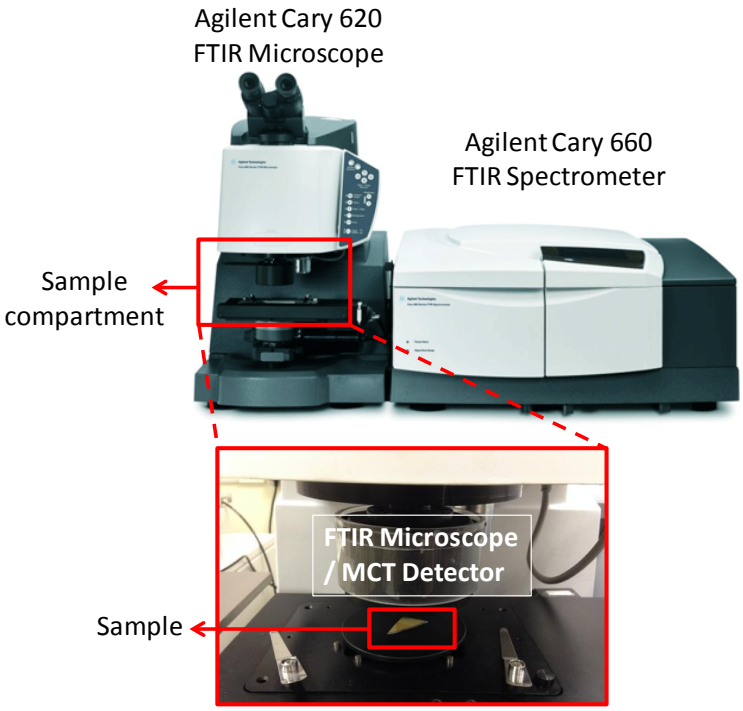

Figure 2.8: Experimental setup with Agilent Cary 660 FTIR Spectrometer connected to the Agilent Cary 620 FTIR Microscope. The inset is a closer view of the sample compartment.

The FTIR Microscope is also used in the measurement of the PhC sample at high temperatures, with an additional accessory as shown in Figure 2.9. The sample is placed in the air-tight sample compartment which is mounted on the FTIR Microscope. The MIR source and detector is above the sample for measurement of reflection. The heating stage is connected to a water circulator which provides water flow so as to induce cooling of the temperature within the compartment. The temperature within the compartment is sensed by the temperature controller which will control the heating elements within the stage to regulate the temperature of the sample. The close-up view of the sample compartment is shown in (b). As shown, the heating elements are in contact with the sample to ensure fast conduction of heat to the sample. The schematic of the measurement setup is shown in (c). The sample compartment can be

closed and MIR beam is input to the sample through the CaF_2 window (not shown in figure). The reflected MIR beam is then collected through the optics of the FTIR Microscope and detected by the MCT detector. At each temperature step, which can be set from room temperature up to 450°C through the use of the computer, the temperature controller ensures that the temperature variation is less than ±5%. In this thesis, the temperature sets are room temperature (25°C) and from 100°C to 450°C in steps of 50°C. When the thermometer displays the desired temperature within the chamber, the sample is left for an additional ten minutes before any measurement is taken. This is to ensure that the temperature of both the membrane and the chamber is stabilized.

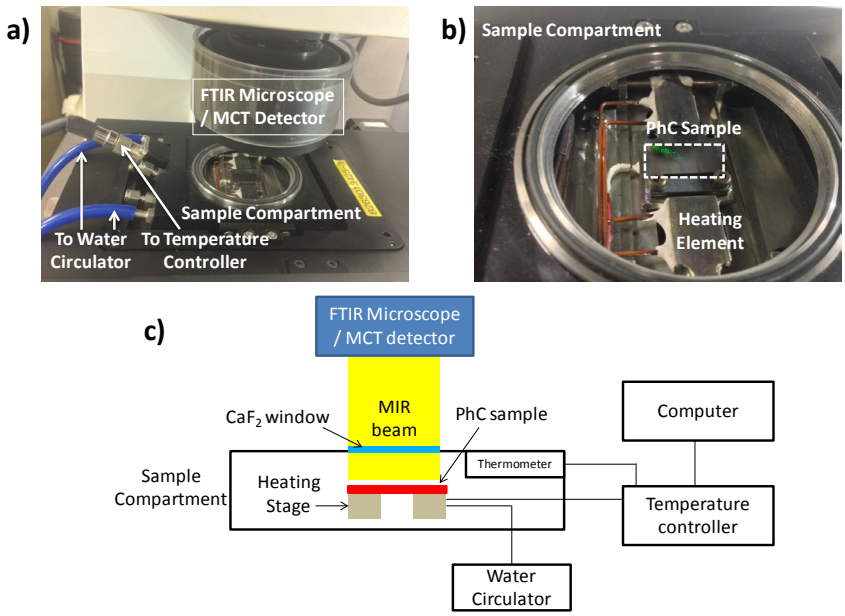

Figure 2.9: Photo of the measurement setup for the thermal measurements, (b) close-up photo of the sample compartment and (c) schematic of the thermal setup.

2.3 Conclusion

In summary, this chapter introduces the main methodologies that are used to predict the performance of the PhC devices. The band structure of the device is

derived using plane wave expansion method and this is readily available through commercial programs such as Rsoft and MIT Photonic Bands. For full characterization of the device, FDTD method is used through the commercial program Lumerical. These two methodologies allow the prediction of the performance of the devices, which is especially important due to the long duration needed for fabrication. In addition, two kind of measurement setups are introduced for in-plane photonic measurement and out-of-plane measurement respectively. For in-plane photonic measurement, the coupling mechanism, which involved in-line placement of chip and fiber, and another coupling mechanism, which uses grating couplers, are used and have been successfully tested in experiment. For out-of-plane measurement, the Cary 660 FTIR spectrometer is heavily utilized for MIR wavelengths. By connecting the Cary 660 FTIR to the Cary 620 FTIR Microscope, the spot size of the beam is controllable from 50 by 50 μm^2 to 250 by 250 μm^2. In addition, the FTIR Microscope can be used with a heating stage which allows the experimentation of devices with varying temperature conditions.

CHAPTER 3: In-plane Photonic Crystal based designs for sensor applications

3.1 Introduction

In this chapter, a Si based PhC waveguide which operates in the slow light regime is reported. Slow light means that the light travels with a very low group velocity. In general, the proposed PhC waveguide can support the slow light because of the standing wave pattern generated by the PhC lattice. Hence, by leveraging the engineering effort of the PhC lattice design, the slow light properties can be modified and enhanced. Slow light is instrumental in sensor applications as it increases light-matter interaction. This enhances the changes to the properties of the light propagating within the device and shows larger sensitivity to environmental changes. In this particular design, the second line of circular air holes from the PhC waveguide in triangular lattice is replaced by a line of ellipse air holes. By replacing the second nearest line of circular air holes of both sides of the waveguide into ellipse air holes, the slowdown factor of the propagation mode is enhanced. Lattice shifting method has been reported as an attractive approach to study the slow light effect on the PhC waveguide [159-161]. Thus both the size and shape of the PhC air holes and their lattice positions are investigated to achieve lower dispersion. Based on 3-D PWE simulation, the lateral shift of ellipse air holes is conducted to enhance the slow light characteristics. By using ellipse air holes and performing lateral shift in the air holes position, a group index of 166 and DBP of 0.1812 are obtained through simulation. The details of the optimized PhC structure are detailed later. Finally,

to demonstrate the slow light effect, we fabricate slow light devices comprising Mach-Zehnder interferometer (MZI) embedded with the PhC waveguides based on optimized lattice shift results. The MZI is integrated with the above-mentioned PhC waveguide is 17 μm in length in one of its arms. The measured transmission spectrum of fabricated MZI embedded with PhC waveguide will show interference patterns when the normal propagating light interacts with the slow light.

We will also move on to investigate the performance of in-plane PhC designs using AlN as the main optical material. This will be the preliminary work that is needed to lay the foundation for more sophisticated photonic design exploration later. We start the investigation with a simple AlN bus waveguide that is coupled to a 1-D PhC design which has a cavity defect. We have designed the coupling wavelength to be 1550 nm. However, due to fabrication variations, experimental results show that the coupled wavelength is around 1575 nm instead. Nonetheless, the dip in the optical signal measured from the bus waveguide still reveals a high Q-factor of 2000. This signifies that AlN is a viable option to be used as an optical layer despite its relatively low refractive index. The propagation loss for AlN waveguide is also within tolerance. This bodes well for further optical design involving AlN especially when the material offers flexibility such as non-linearity and piezoelectric effect, which are absence or difficult to obtain in Si based photonic designs.

3.2 Slow light effect in Si PhC design

3.2.1 Design and Modelling

As mentioned before, the slow light design seeks to maximize the DBP. Based on previous works as summarized in Table 5, DBP is relatively small and in order for it to be suitable for applications such as sensing, the DBP has to be increased.

Table 5: Summary of performance of existing works on slow light

	Design	Group index	Bandwidth (nm)	DBP
C. Bao et al. IEEE Photonics Technology Letters, vol. 23, no. 22, 2011	Grating waveguide with slot	13	13.2	0.110
C. Bao et al. IEEE Photonics Technology Letters, vol. 24, no. 1, 2012	One dimensional grating waveguide	18.3	10.3	0.122
C. Caer et al. IEEE Photonics Technology Letters, vol. 23, no. 18, 2011	PhC based corrugated slot waveguide	130	1.5	0.126
Our work	Si based elliptical PhC waveguide	166	1.69	0.181

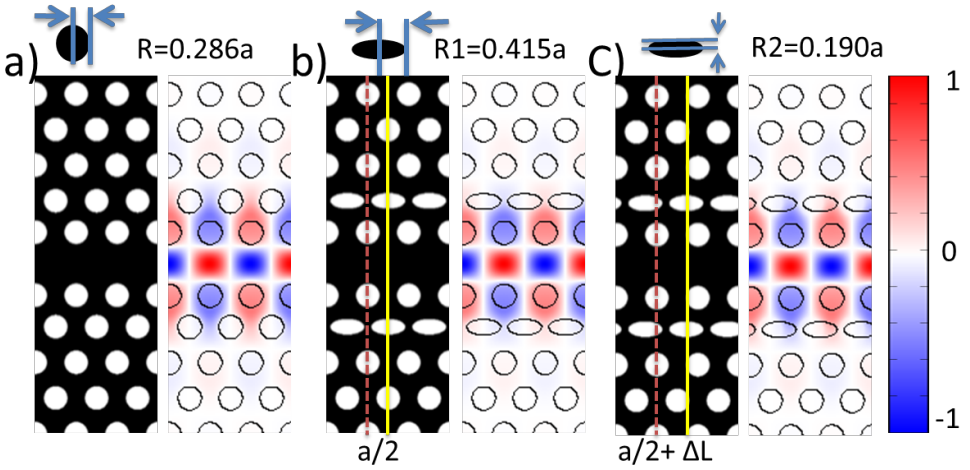

Figure 3.1: Schematic of proposed structure and simulated electric field distribution (a) normal photonics crystal lattice; (b) one line of circular air holes is replaced by ellipse shape air holes; (c) the ellipse air holes shift to half of the lattice period; The red dashed line indicates the original lattice position.

The proposed basic PhC structure containing circular air holes in triangular lattice is shown in the Figure 3.1(a). The radius of each air holes R is designed to be 0.286**a**, where **a** is the lattice constant of the PhC lattice, in order to obtain the large photonic band gap in TE polarization as shown in Figure 3.2. This is important so that when the PhC waveguide is created by removing one row of air holes, which produces a mode within the band gap, the mode is well confined and have sufficient wavelength allowance for optimization.

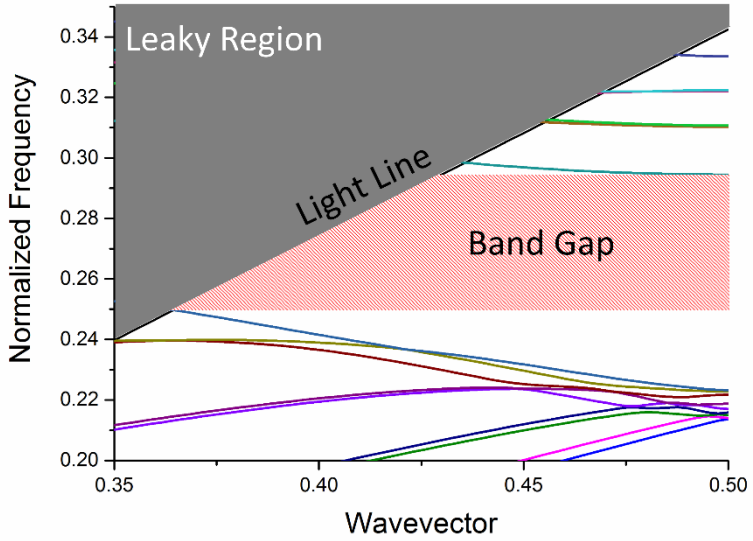

Figure 3.2: Band structure plot of the PhC structure when R is 0.286a.

A PhC waveguide is formed by creating a line defect of the PhC lattice. The interested propagation mode of electric field distribution is also shown in (a). The main propagation mode of light inside the PhC waveguide is TE mode in simulation. We can observe a highly concentrated field energy in the waveguide region, utilizing the highly confinement by the PBG in the triangular PhC lattice. Reducing the line defect width [159, 160, 162] and changing the selected hole position either perpendicularly or laterally can enhance the slow light effect [161, 163]. Briefly speaking, the group index and the bandwidth can be

optimized by shifting the lattice line and modifying the air hole shape. Therefore, we further modified the propagation mode of the PhC waveguide by changing the second nearest line of circular air holes into a line of ellipse air holes, as shown in the Figure 3.1(b). The PWE modelling suggests a slightly modified mode profile in comparison with the data shown in Figure 3.1(a), i.e., result derived from PhC waveguide of circular air holes. The elliptical air holes are placed along the lateral direction, and the longer radius is parallel to the light propagation direction. The longer and shorter radii of the ellipses are denoted as R1 and R2 shown in (b)-(c), and are optimized as 0.415**a** and 0.19**a**, respectively. The PhC waveguide propagation mode can be further reproduced by lateral shifting the ellipse shape air holes to off-lattice positions [79]; we define ΔL to represent the offset from the lattice position, as shown in the (c). The red dashed line represents the origin position of triangular lattice and the solid yellow line indicates the original ellipse hole lattice position. We shifted the elliptical air holes along the light propagation direction by ΔL, meaning the yellow solid line shifted away from the red dashed line by ΔL. The difference of index profile of the electric field introduced by shifted elliptical air holes modifies the standing wave pattern attributed to the light scattering in the waveguide. Hence the propagation mode within the PhC waveguide is modified and also affects the slow light profile.

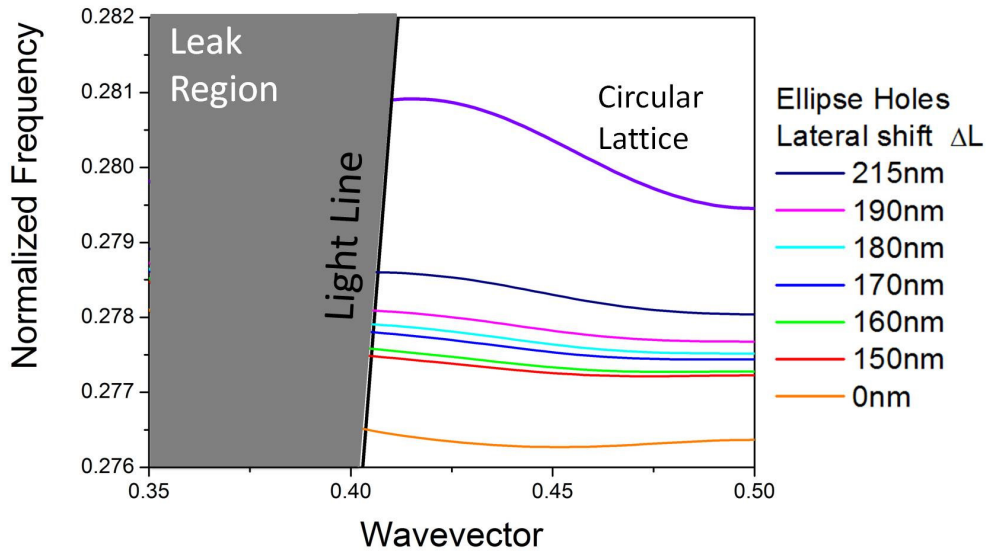

Figure 3.3: Band structure plot of the ellipse PhC waveguide.

Figure 3.3 presents the band structure of the various designs of PhC waveguides. The basic circular lattice design, ellipse lattice design and six different designs of PhC waveguide with different lateral shifts are shown. All of the pass band modes present a linear band profile. The pass band of the basic circular lattice design, shown on the top of band structure plot, is centered between the 0.2810 and 0.2795 of normalized frequency. This range is much wider than the ellipse lattice pass band between 0.2762 and 0.2765, i.e., the bottom line in Figure 3.3. As the lattice shift ΔL changes from 0 to 215 nm, i.e, half of the lattice constant, the pass band of PhC waveguide of larger ΔL moves to higher normalized frequency. However, comparing with the original circular lattice position, all pass band of PhC waveguides with shifted lattice are in higher wavelength range. The pass bands of the lattice shifted design are centered at the normalized frequency of 0.2775. With the optimized design of PhC lattice constant as 430 nm, we can localize the slow light region at 1550 nm wavelength range.

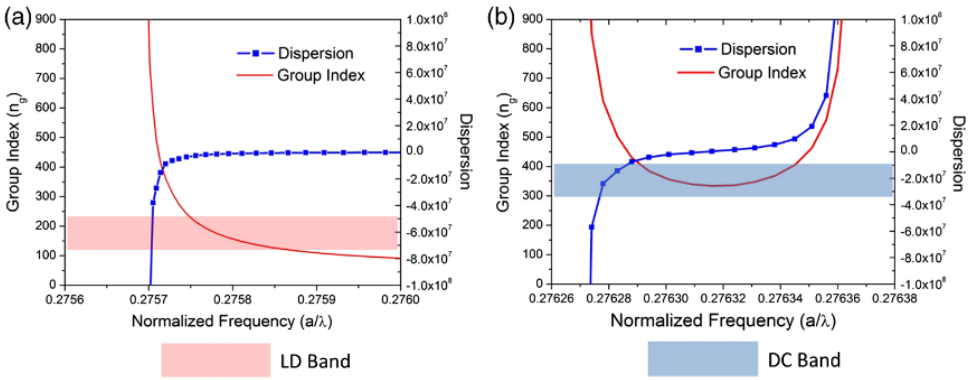

Figure 3.4: Group index n_g and group-velocity dispersion plot against the normalized frequency of (a) circular holes lattice; (b) ellipse holes lattice.

Figure 3.4 illustrates the improvement of n_g and GVD as a function of the normalized frequency of the circular lattice and the ellipse shape lattice PhC waveguide. The group index n_g is given by the inverse of the TE-like group velocity v_g at operating wavelength. Moreover, the GVD is given by the slope of the group index n_g, which is described as $d(v_g^{-1})/d\omega=d^2k/d\omega^2$. The circular holes lattice produces a straight band over a large range of bandwidth. This is referred a low-dispersion (LD) slow-light band. However, as the lattice structure is modified to a line of elliptical holes, a flat band in the group index plot is shown and it can be considered as a dispersion compensated (DC) slow-light band. As shown in (b), the DC band is a narrow band slow light and the group index is 300, which is observed within a range of the normalized frequency where the GVD value is close to zero. Similar simulation work has been done on different lateral shifting lattice and the results are shown in Figure 3.5. The group index profile changes from an S-shape to a U-shape as lateral shift away from its central position. From Figure 3.5(a), the S-shape-like group index flattens the index profile which expands the bandwidth with the low group velocity region. The GVD plot shows a low dispersion region at the S-shape

group index region. It is clear that as the ellipse lateral shift increases, the group index decreases but the interested bandwidth expands with the lateral shift increases. A peak of group index profile is observed when the lattice shift ΔL reaches 180 nm. The nearly constant high group index region narrow by the index peak and change to a U-shape profile. The nearly zero GVD shows in the low velocity region but giving high fluctuation at the index peak point. The group index and the DBP for all the different designs from the group index plot are shown in Figure 3.5. The DBP is defined as the product of group index and the bandwidth, and is given by DBP= $n_g(\Delta\omega/\omega)$. A larger bandwidth is more desirable in most applications. However, it comes with a tradeoff, i.e., a lower group index. The range of the wavelengths over which the group index remains a certain constant is considered as the best operating wavelength range of the device. It is usually defined as the flat band range where the group index variation within 10% of its value. Thus, that flat band is considered as the bandwidth of the device. From Table 6, we can observe that the group index of the PhC waveguide decreases from 300 to about 100 as the ΔL shift further away till half of the period. However, the bandwidth of the PhC waveguide expands to its maximum value at ΔL = 160 nm and then it narrows down as the ellipse lattice further shifts, while the group index peak is observed in the plot. The group index and the bandwidth are 166 and 1.69 nm at the shift distance of 160 nm, where a maximum DBP is derived as 0.1812. By considering both the group index and dispersion, we fabricated and tested the designed PhC waveguide with the ellipse air holes with lateral shift of 160 nm.

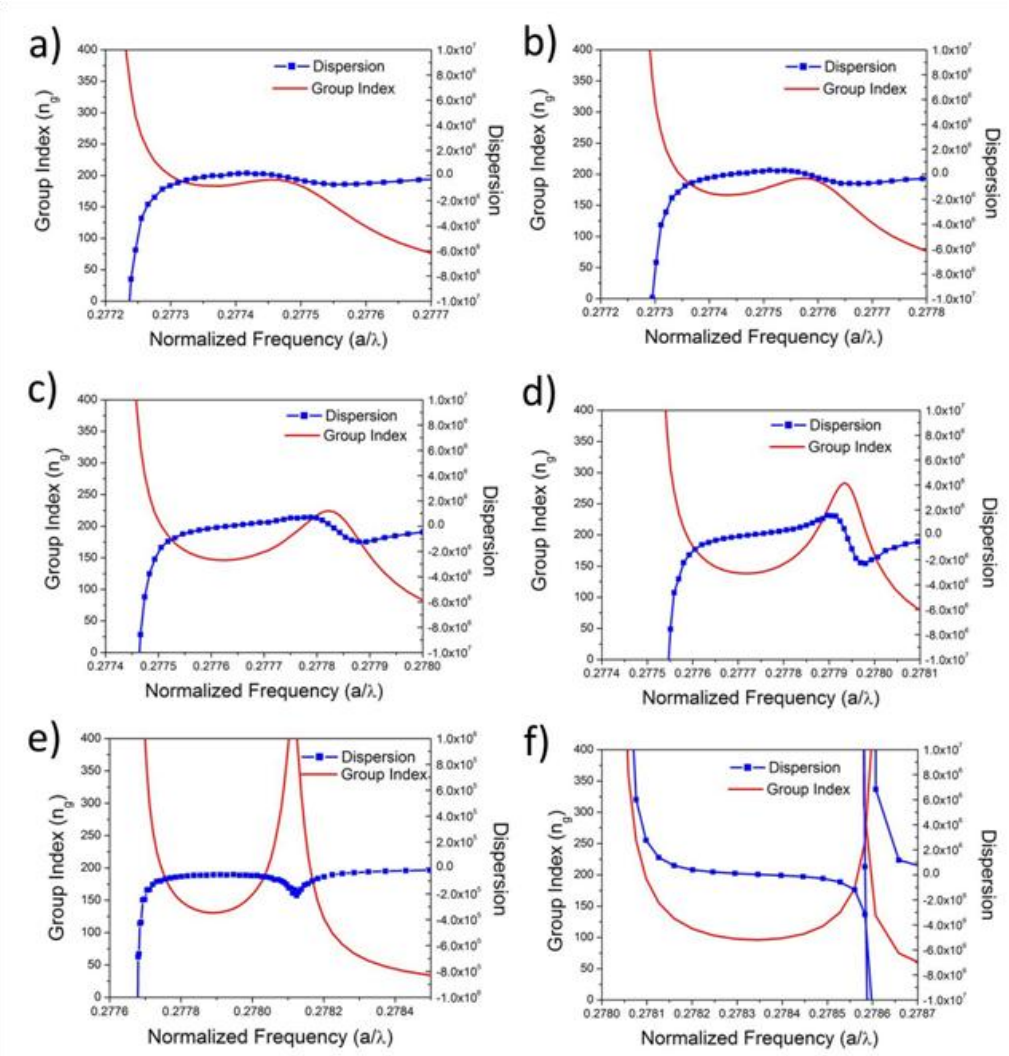

Figure 3.5: Group index n_g and group-velocity dispersion plot against the normalized frequency of various designs with ellipse hole shift. (a) the line of ellipse holes shift laterally 150 nm; (b) shift 160 nm; (c) shift 170 nm; d) shift 180 nm; (e) shift 190 nm; (f) shift half of lattice constant a.

Table 6: Group index and bandwidth of designs with ellipse PhC

	Design	Group Index	Bandwidth	DBP
Lateral shift (ΔL)	Ellipse without shifts	333	0.079 nm	0.017
	150nm	183	1.39 nm	0.1641
	160nm	166	1.69 nm	0.1812
	170nm	146	1.15 nm	0.108
	180nm	138	0.953 nm	0.0848
	190nm	130	1.18 nm	0.10
	215nm (Half Period)	95	1.6 nm	0.09

3.2.2 Device fabrication and characterization

As shown in the Figure 3.6(a), the PhC waveguide is embedded in one of the MZI arms with a total length of 17 μm and the device is fabricated to demonstrate the existence of the slow light effect. The reference arm is a 440 nm width Si strip waveguide. The total length of each arm of the MZI is designed to be 300 μm between the two Y-shape beam splitters. The 440 nm wide Si bus waveguide splitter into two beams at the 15 degree Y-shape junction. An optical microscope image of fabricated device is shown in Figure 3.6(b). The light is brought to the device through the use of a fiber array. In this setup, the fiber array is placed orthogonally to the surface of the chip and its alignment to the device is ensured through the use of an optical microscope. The light from the fiber array is then coupled in and out from the bus waveguide via two adjacent grating couplers which are located at the bottom of (b). The spacing between the two grating couplers is 127 μm which is designed to fit the PM-fiber array for easy alignment. The entire structure is patterned using electron beam lithography and then etched using plasma etching (DRIE, Oxford 100 Plus). The pattering is processed on a 220 nm SOI wafer with 2 μm buried oxide layer. SEM image of the fabricated device is shown in the Figure 3.6(c). Figure 3.6(d) is the magnified image of fabricated PhC lattice. The lattice constant is designed to be 430 nm in order to center the slow light region at 1550 nm. Due to imperfections of the fabrication process, the lattice constant and the radius of the air holes are measured as 438.8 nm and 118.4 nm respectively. For the ellipse design, the longer and shorter radii are measured as 173.7 nm and 75 nm, respectively. PhC waveguide of circular lattice are also fabricated as a

reference as shown in Figure 3.6(e)-(f). The radii and the lattice constant are measured as 130 nm and 440.7 nm, respectively.

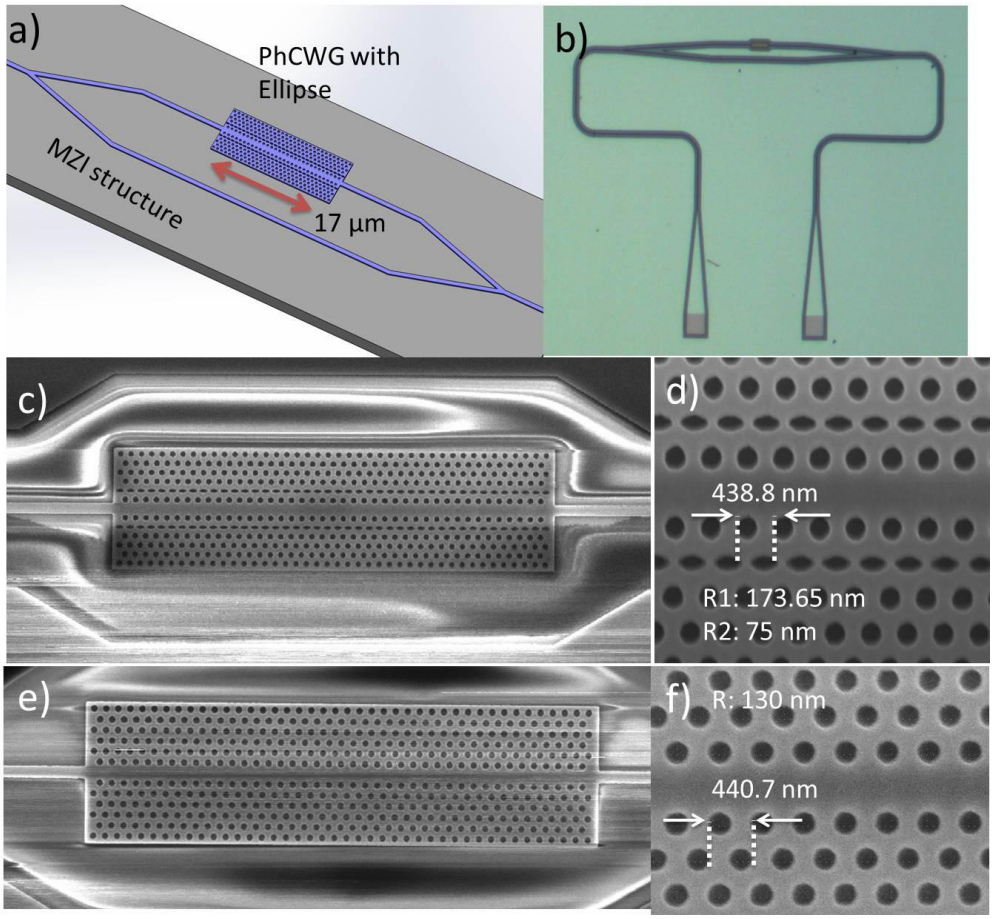

Figure 3.6: (a) Schematic drawing of Mach-zehnder interferometer (MZI) embedded with the PhC Waveguide. (b) Optical microscopy image of fabricated MZI device. (c) SEM image of fabricated PhC waveguide. (d) Zoom-in image of ellipse shape holes.

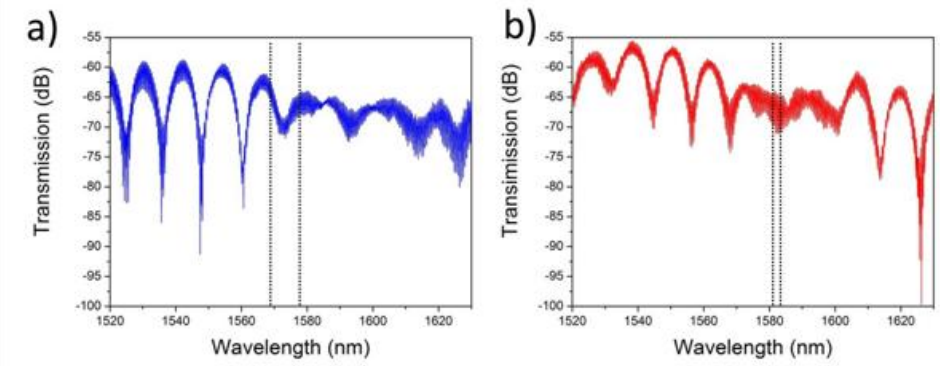

Figure 3.7: Transmission spectrum of fabricated MZI embedded with PhC waveguide (a) circular lattice PhC; (b) ellipse shape lattice PhC.

Figure 3.7 illustrates the measured spectrum of two designs of MZI embedded with the PhC slow light waveguide. The small fluctuation pattern with 0.5 nm fringes separation shown in the spectrum comes from the Fabry-Perot resonance of the grating coupled back reflections [164]. The pass band of propagation mode of the PhC waveguide calculated from the band structure plot is indicated by two dashed lines in the Figure 3.7 for the two cases of circular lattice and ellipse lattice, respectively. They are matched with the measured transmission slow light interference pattern which can be read from the plot. The slow light effect can be observed from the transmission spectrum plot by analysing the portion with MZI interference. The two designs share the same PhC waveguide effective length as well as the MZI design, and are different in the 2nd line of air holes in PhC waveguides, i.e., data of ellipse shape shown in Figure 3.7(b). From the spectrum plot we can clearly observe two portions of transmission structure. One is the interference fringes with a FSR of around 12 nm and the other is a relatively flat pattern due to slow light interference pattern. However, the slow light interference pattern of circular lattice design is much longer than the ellipse pattern, since the passing bandwidth of the circular lattice design is much larger than the ellipse lattice design. The slow light interference pattern is relatively larger than the pass band calculated from the band structure. The mismatch of the calculated and the PWE simulated results is due to the imperfection of the fabrication and the finite period of the PhC structure in the fabricated waveguides. The intrinsic losses due to the PhC waveguide also expand and shift the pass band of the fabricated PhC structure. Further optimization of integrated PhC waveguides and MZI devices will be done to

achieve a flat band slow light over a reasonable range which is desired for various applications. For example, a modulator is benefitted from its low dispersion and large bandwidth; a delay line is benefitted from the large group index and small footprint. Moreover, slow light effect also enhances the study of optical nonlinearities which can have great potential in many functions for OEICs application.

3.3 AlN in-plane PhC design

As mentioned in previous chapter, AlN is an extremely ideal material to be used for photonic applications. AlN is transparent and workable in the communication wavelength of 1.55 μm. On top of that, AlN has exceptional non-linearity properties which are not possible in Si. As a preliminary demonstration of using AlN as a photonic material, we fabricated AlN-based photonic design with a 1-D photonic crystal. This simple design will verify the performance of AlN photonic and lay the foundation for more complicated photonic designs.

3.3.1 Design and simulation of in-plane AlN photonic design

For the design of the 1-D photonic crystal using AlN, the band structure of AlN is first examined using PWE method. The schematic of the 1-D photonic crystal is shown in the inset of Figure 3.8. The designed parameters to be optimized are the thickness of the device layer, the width of the waveguide, **w**, and the radius, **r,** of the air hole. As the design is for an in-plane application, only the bands below the light line are applicable. In this design, the thickness is set to 0.5238**a**,

w is set to 1.587**a** and **r** is 0.25**a**. The simulated band structure is shown in Figure 3.8. The simulated bandgap is found to be from 0.390(2πc/a) to 409(2πc/a). As the desired central wavelength is 1.55 µm, the value of **a** can be calculated to be 0.63 µm. The thickness of the AlN waveguide is 0.33 µm, while **w** and **r** are 1 µm and 0.16 µm respectively. In order to create a resonator, a cavity is created by deliberately not placing an air hole in the middle of the waveguide. The length of this defect is set to 0.7 µm.

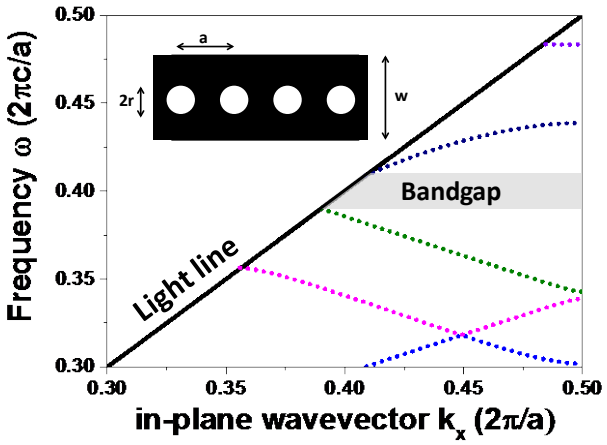

Figure 3.8: Band structure of the PhC design in AlN waveguide, the inset showing four unit cells with various design parameters.

The transmission spectrum of the device is also simulated using FDTD as shown in Figure 3.9. As seen, the defect in the PhC design will couple input light at 1.582 µm as this wavelength is missing from the simulated output. The Q-factor of this resonance is seemingly low in the simulation. This is due to the tradeoff taken during simulation which requires very long simulation duration and extensive computer memory utilization to ensure that the simulated Q-factor is accurate. Nonetheless, the simulation offers an insight to the wavelength at which the resonance will occur.

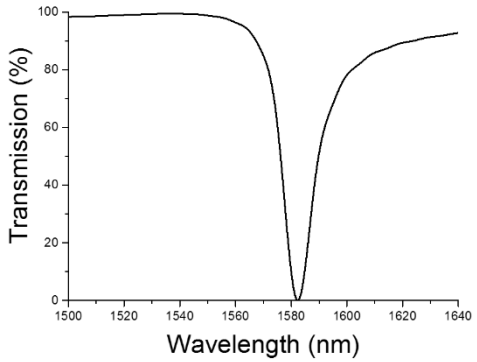

Figure 3.9: FDTD simulation of AlN photonic device.

3.3.2 Fabrication process of in-plane AlN photonic design

The process flow to realize the AlN based photonic design starts with an 8" bare Si wafer. A 2 μm silicon dioxide (SiO_2) layer is then deposited using plasma-enhanced chemical vapor deposition (PECVD) to act as the buried silicon oxide (BOX) layer. A layer of 0.33 μm AlN using Physical Vapour Deposition (PVD) and a 150 nm hardmask of SiO_2 are then deposited. Photolithography is then done to define the photonic designs. The hardmask is etched before the patterns are transferred to the AlN device layer. The hardmask is then removed and the wafer cleaned and diced. The SEM image of the fabricated device is shown in Figure 3.10. The input light is introduced to the PhC design via the bus waveguide. The zoom-in image of the coupling area is shown on the right. The gap between the two waveguides is set to be 300 nm. After the wafer is cleaned, it was found that there are AlN particles that residue on the top of the BOX layer. This is due to the imperfection of the etching recipe used and can be totally avoided when better etching recipes are developed. However, the presence of such AlN residues will not impact the photonic performance as their sizes are too small.

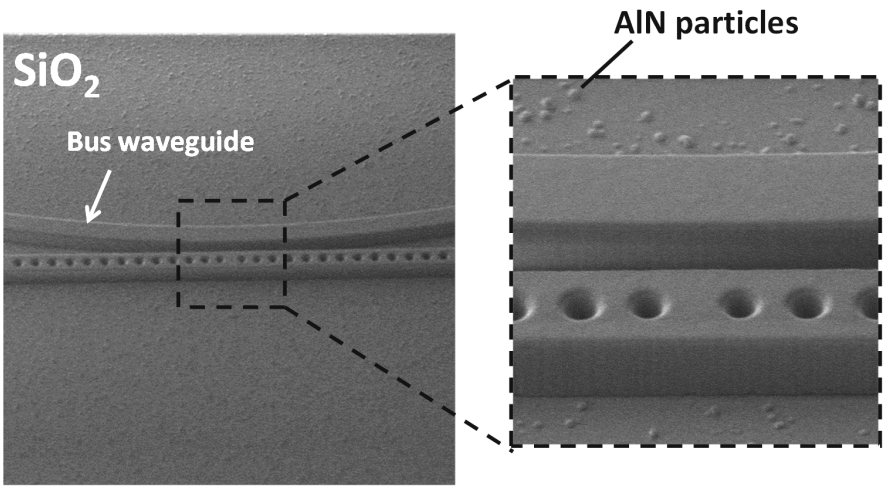

Figure 3.10: SEM image of the fabricated device. The zoom-in image of the coupling region is shown in the right.

Another challenge that was faced in the fabrication of AlN photonics is the lack of anisotropy during deep reactive-ion etching (DRIE) of AlN. While the selectivity of AlN to SiO_2 etching is very high (more than 1:10), the sidewall profile of AlN after etching is not straight. As shown in Figure 3.11, the sloping sidewall of AlN after etching is very apparent. Based on measurement and calculation, the sloping sidewall has an angle of 81^o. This has an impact in the performance of the photonic design and has to be taken into account during simulations.

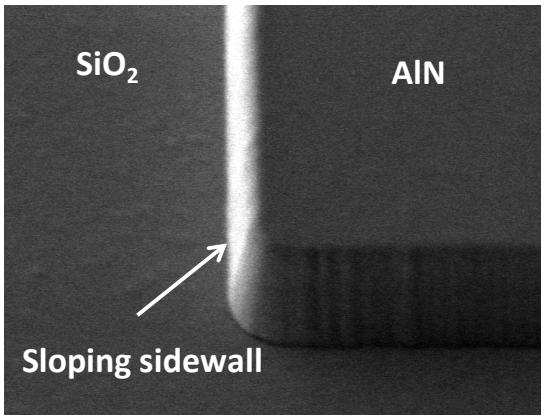

Figure 3.11: SEM image of the wafer which shows sloping sidewall after etching of AlN.

3.3.3 Characterization of in-plane AlN photonic design

The AlN photonic device is characterized using the in-plane photonic measurement setup described in previous chapter. The input wavelength is scanned from 1505.12 nm to 1597.99 nm with a resolution step of 0.02 nm. At this resolution, the maximum Q-factor measurable is around 70000 which is sufficient for this design. Measurement of the device reveals that the insertion loss is around 45 dB which is rather high. This could be due to the sloping sidewall at the coupling facet of the AlN waveguide to the fiber at the diced end of the device. The resonance of the device is around 1576.3 nm which matched relatively well to the FDTD simulation as shown in Figure 3.12. The Q-factor of the device is calculated to be around 2000. While this result is not comparable to Si based photonics, we believe that the performance of the AlN photonic device can enhanced through further optimization of the designed parameters and through better fabrication techniques. Currently, the sidewall of etched AlN is sloping and this has a negative impact on the performance.

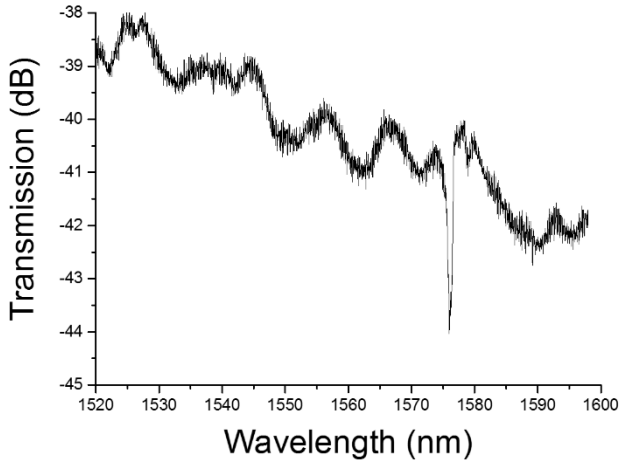

Figure 3.12: Measurement of the AlN photonic device.

3.4 Conclusion

In conclusion, we demonstrated a novel design of dispersion engineered slow light PhC waveguide. The slow light performance is optimized by changing the second line of PhC air holes from circular shape to ellipse shape. The lateral shift of such a line of ellipse air holes is analyzed through PWE model approach. The group index and low dispersion bandwidth are optimized to 166 and 1.69 nm, respectively, where the DBP is derived as 0.1812. The optimized PhC using ellipse lattice design of lateral shift 160 nm were fabricated and embedded in a MZI in order to characterize the slow light characteristics of such elliptical PhC waveguide. A slow light interference pattern is observed in both transmission patterns of MZIs embedded with the ellipse and circular lattice PhC waveguides. The enhancement of the slow light performance within the device increases light-matter interaction which potentially increases the sensitivity of the device to environmental changes. We also extended the investigation to implementing in-plane photonics with AlN as the device layer. This is done through a simple design of PhC resonator by introducing a defect. Measurement of the device reveals a resonance at 1576.3 nm with a Q-factor of around 2000. While the performance of this AlN photonic device is not exceptional, it can be enhanced through meticulous optimization of the design. More importantly, the fabrication process at the current state left much to desire. Once these issues are resolved, we believe that AlN photonics can perform as well as Si photonics and pave a strong foundation for further endeavours for better optical designs such as tunable slow light devices using AlN.

CHAPTER 4: Two-Dimensional Out-of-plane Photonic Crystal based Reflector

4.1 Introduction

In this chapter, we report the design, fabrication and characterization of ultra-compact polycrystalline Si based 2-D PhC reflector working in the MIR range. Two designs of the PhC membranes with circular and square air holes were investigated and characterized to show greater than 90% reflectivity in the MIR wavelength at 3.45 μm, which are important wavelengths for applications of detection of gases with hydrocarbons. The bandwidth of the high reflectance should be less than 200 nm but more than 100 nm. To the best of our knowledge, this is the first demonstration of a free-standing polycrystalline Si PhC membrane to be used in MIR region. High annealing temperature is used to reduce the residual stress in the membrane. In order to further reinforce the mechanical strength of the PhC membrane, PhC with square air holes was developed. Compared to circular air holes, PhC with square air holes maintains high reflectivity in MIR region. However, square air holes when compared to circular air holes, have a lower filling factor, which is defined as the volume of air holes over the volume of Si within a unit cell. This makes the membrane less brittle while keeping the reflectance around 3.45 μm more than 90%.

We also subject the polycrystalline Si based 2-D PhC membranes to high temperatures and examine the impact of temperature on its performance. As expected, thermo-optic effect dominates the performance and the peak wavelengths shifts towards higher wavelengths as temperature increases. At

450°C, the peak reflection wavelength shifts by 75 nm and it is measured that thermo-optic effect induces a shift of 0.174 nm per degrees Celsius temperature change. This indicates that the thermo-optic coefficient of the device is $+1.70\times10^{-4}$ K^{-1}. In order to offset thermo-optic effect in Si based PhC membranes, we introduce a simple method by simply altering the dimension of the air holes in order to ensure that peak reflection is at the desired wavelength after thermally induced shift.

While the method of altering the size of the air holes proves to be a possible solution, it is however suitable for applications with only one expected working temperature. In order to achieve a more passive correction to thermo-optic effect, it is more ideal to have a material with very low thermo-optic coefficient. In this aspect, AlN is a good material of choice as it has a thermo-optic coefficient which is one order lower than Si. In this chapter, we demonstrate the usage of AlN as the PhC reflector material and show how its peak reflection wavelengths remain relatively unchanged even at 450°C working temperature. This showcases the robustness of AlN as a photonic material.

4.2 Design, modelling and fabrication of Si-based Photonic Crystal reflector

The schematic of the design with air holes is shown in Figure 4.1(a). The radius of the air hole is indicated as **r**, the lattice constant is defined as **a** and the thickness of the PhC membrane is **t**. In our proposed PhC device, the ratio of **r/a** and **t/a** are set to be 0.395($2\pi c/\mathbf{a}$) and 0.513($2\pi c/\mathbf{a}$) respectively. Figure

4.1(b) shows the corresponding band structure of the PhC design that was calculated based on PWE. As can be seen, a band gap (shaded in red) is found from 0.528(2πc/**a**) to 0.587(2πc/**a**). In order to have a high reflectivity of more than 95% at 3.45μm, the lattice constant is determined to be 1.92μm. The radius is calculated to be 0.758μm and the thickness of the Si membrane is 0.985um. Fabrication of the PhC began with a bare Si wafer and a 1μm thick BOX was grown using thermal oxidation (Figure 4.2(a)). This was followed by a 1μm thick low-pressure chemical vapour deposition (LPCVD) Si layer which acts as the device layer (Figure 4.2(b)]. In order to ensure that the Si device layer is polycrystalline and to reduce the residual stress of the eventual suspended membrane, a high temperature anneal of 1000^{o}C was done for 30 minutes (Figure 4.2(c)). The surface was then patterned by using deep-UV lithography and DRIE (Figure 4.2(d)). The photoresist (PR) on the wafer is then stripped and the wafer cleaned. Finally, the selected reticle on the wafer is released using vapour hydrofluoric acid (VHF). The importance of the VHF release will be highlighted in later section. In Figure 4.1(c), the SEM photograph is shown. Due to fabrication uncertainties, the radius of the air holes is 0.77 μm and the lattice constant is 1.95 μm. The thickness of the device layer is measured as 1 μm.

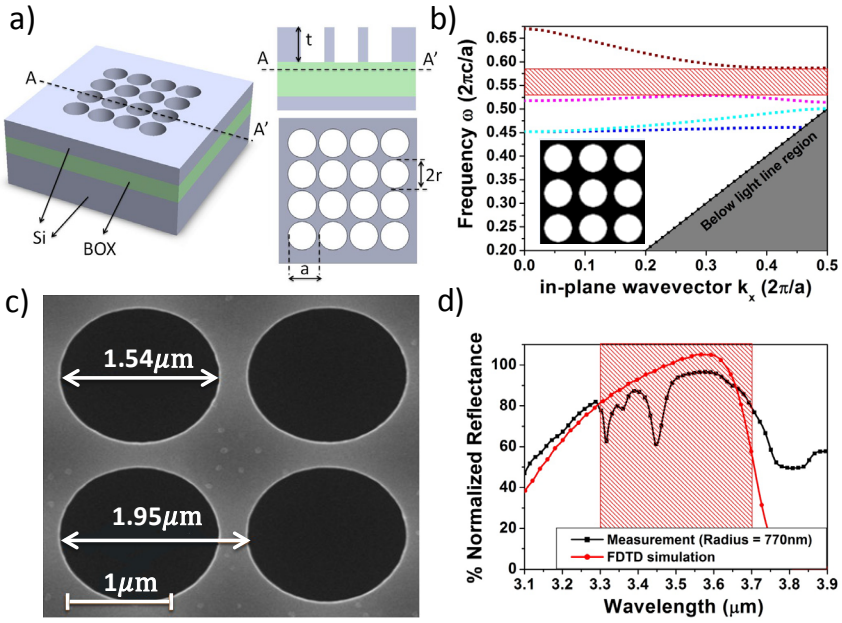

Figure 4.1: Schematic of the structure with circle air holes and (b) band structure of the propose PhC with circle air holes with the band gap region shaded in red. (c) SEM image of the fabricated device and (d) the simulation of the reflectance based on the fabricated PhC with circle air holes overlaid with the measurement result.

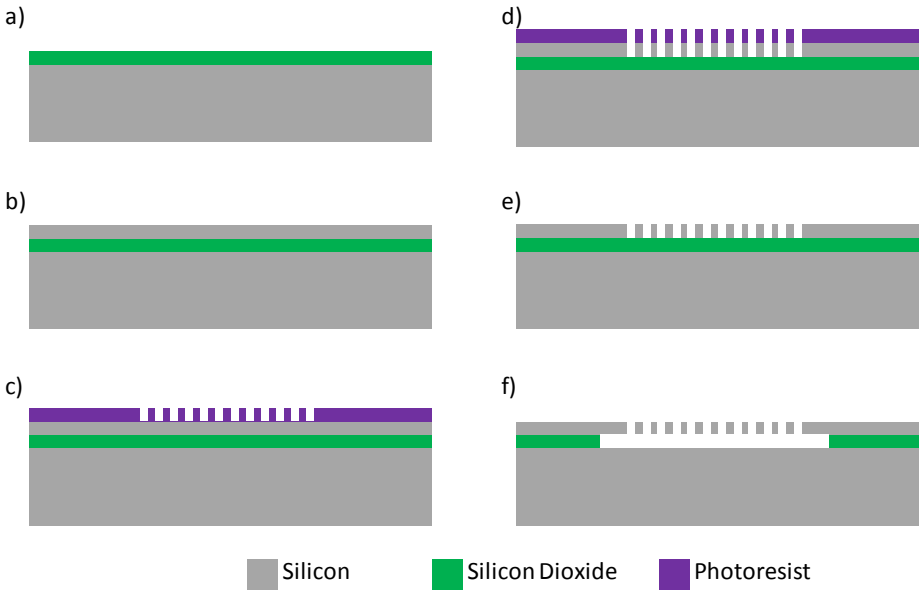

Figure 4.2: Process flow for PhC based reflector. (a) 1µm thermal SiO_2 is grown on a bare 8" Si wafer. (b) 1µm Si is then grown using LPCVD and annealing is done at 1000°C. (c) Coat and photolithography of PR to define air holes. (d) DRIE of Si to pattern the air holes. (e) PR strip and cleaning of wafer. (f) Device release in VHF.

Simulation is done using FDTD methodology to examine the performance of the PhC membranes. The refractive index of the Si is assumed to be 3.464 and the boundary conditions of the unit cell is set to periodic. The incidence angle of the input light beam is set to 45° which is consistent to the experimental setup that is used for measurement. As shown in Figure 4.1(d), the simulated reflectivity displays a peak around 3.60 µm and more than 90% reflectivity over a 286 nm range. In addition, it also matches well with the band gap region from the band structure calculated in (b), where the reflectance is high within the band gap region and experiences a drop once outside it. Generally, the simulated result agrees well with measurement result expect for two dips in reflectivity at 3.31 µm and 3.45 µm. The higher reflectivity measured after 3.70 µm wavelength is due to the reflection caused by the presence of the substrate.

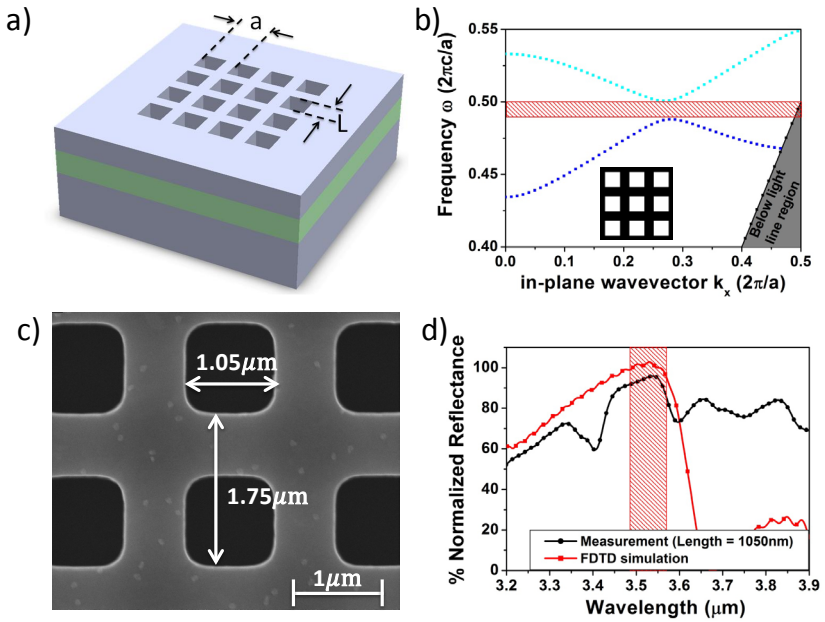

Figure 4.3: (a) Schematic of the structure with square air holes and (b) band structure of the propose PhC with square air holes with the band gap region shaded in red. (c) SEM image of the fabricated device and (d) the simulation of the reflectance based on the fabricated PhC with square air holes overlaid with the measurement result.

Similar approach is adopted for the design of the square air holes in Figure 4.3(a). The length of the square air hole, **L**, is designed to be 0.618**a** and the thickness, **t**, is set to be 0.588**a**. Based on the band gap region from 0.488(2πc/a) to 0.501(2πc/a) in Figure 4.3(b), the lattice constant is determined to be 1.70 μm. This equates to an **L** of 1.05 μm and **t** of 1 μm. The SEM photograph of the fabricated PhC membrane is shown in Figure 4.3(c). Similar to the circle air holes, fabrication uncertainties caused the measured length of the square air holes to be 1.05 μm and the lattice constant to be 1.75 μm. The device layer of the square air holes is still 1μm. From the fabricated parameters, it can be calculated that the filling factor of the square air holes in the membrane is 36%. In contrast, the filling factor for circular air holes is 49%. The lower filling factor allows the membrane to be mechanical stronger and hence less brittle. This allows more flexibility in design and fabrication especially in MEMS application where such membranes are released and free-standing, as demonstrated in our PhC design. Simulation is also performed using FDTD calculation. The simulated result shows a high peak around 3.55 μm in Figure 4.3(d) and this match well with the measurement data. It can be observed that the square air holes are rounded and the radius of the curvature of the edges is estimated to be around 200 nm. In order to examine the effect of the rounded edges of the square holes, we have simulated the structures using FDTD. The curvature of the edge is related to the radius of the circle as shown in Figure 4.4(a). At a radius of 525 nm, the air hole is circular in shape.

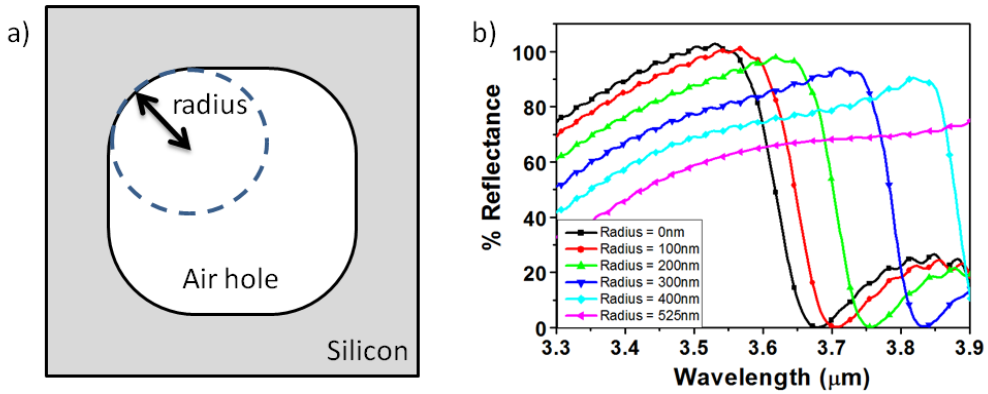

Figure 4.4: (a) Definition of radius with respect to the curvature of the edge, (b) FDTD simulation of reflectance with various radius of curvature at the edge.

The simulated reflectance is summarized in Figure 4.4(b). As shown, as the edges get more rounded, the reflectance starts to redshift and maximum reflectance decreases. If we benchmark high reflectance to be more than 90% at the desired wavelength of 3.55 μm, the tolerance is close to a rounded edge of radius 200 nm. Based on the fabricated device, the curvature radius is around 200 nm and this is within the tolerance that is allowed for a high reflectance.

4.3 Characterization of Si-based Photonic Crystal reflector

The experimental results of circle air holes are shown in Figure 4.5. The PhC reflectors are designed to be 300 by 300 μm^2 in order to ensure that the input beam is illuminated only on the PhC patterns. This is done by controlling the size of the aperture on the microscope and ensuring that the device is placed within the illumination area. The background spectrum which the measurement results are normalized against is reflection of a gold surface which, as previously mentioned, assumed to have an almost perfect reflectance across the MIR wavelengths. The measured reflectance of the circle air holes of radius 770 nm shows a peak of 95.5% at wavelengths around 3.61 μm and reflectance greater

than 90% spans from 3.56 µm to 3.68µm. As the radius of the circle air holes changes, it is observed that the reflected bandwidth experiences a blueshift as the radius increases. This can be attributed to the slight shift in the band gap region towards higher frequencies as the ratio of **r/a** increases. Outside the band gap region, low reflectance values are measured. It is expected as the light enters one of the propagation modes sandwiching the band gap region.

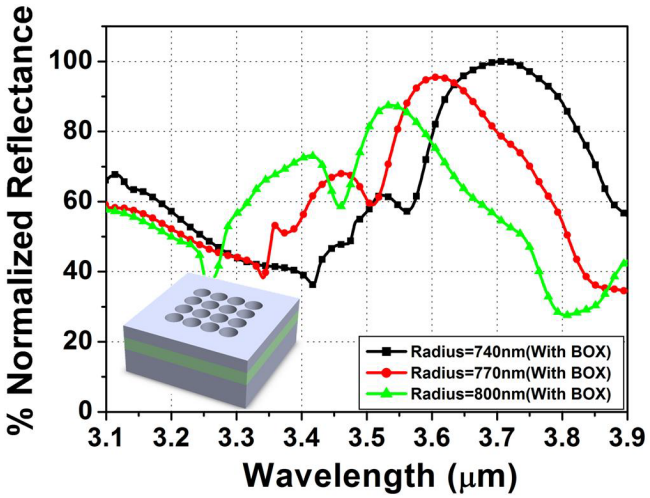

Figure 4.5: Experimental results of circle air holes design (with BOX).

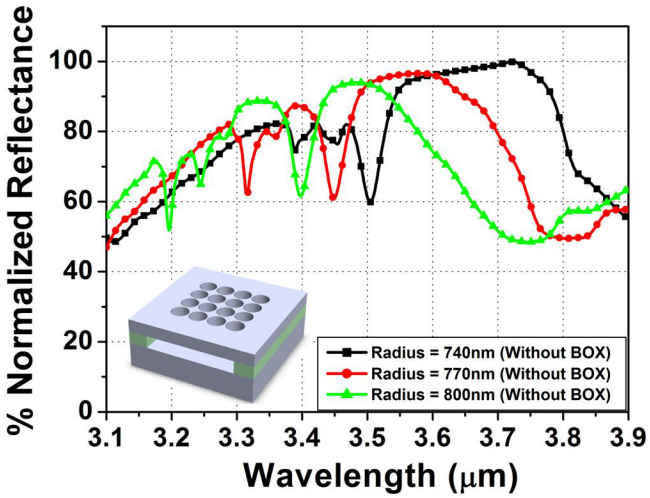

Figure 4.6: Experimental results of released circle air holes design (without BOX).

For an increased performance of the PhC membrane with circle air holes, the

BOX layer is removed by isotropic etching using VHF. The schematic of the released structure is shown in the inset of Figure 4.6. The measured reflectance of the PhC membrane with different radius of the circle air holes is shown as well. A peak of 96.5% reflectance is observed at 3.58 μm for circular air holes with radius of 770 nm. Generally, the spectra measured for the released PhC membrane with circle air holes shows a distinct blueshift when compared to the unreleased circle air holes design. As the BOX layer is removed, the refractive index of the cladding below the PhC membrane decreased from 1.44 (SiO_2) to 1 (air). This reduces the effective refractive index which leads to the movement of the spectra towards lower wavelengths. Sharp dips in reflection are also found at 3.31 μm and 3.45 μm, and such dips in reflection are attributed to non-zero angle of incidence according to K. B. Crozier [83]. In this case, the incidence angle is set to 45^o. In the band structure analysis of the PhC reflector, existing modes will coupled into PhC reflector and appears as low reflection dips. This is shown in the simulation where modes are coupled into the PhC reflector at 3.25 μm (not shown), 3.47 μm and 3.70 μm. However, these modes might not appear as strongly coupled in experimental measurement as it depends on the strength of the coupling of the illumination and the PhC reflector. In order for the mode to display low reflection, the electric field distribution of the mode has to possess even parity about x-axis and odd parity about y-axis or vice versa. When this condition is fulfilled, the plane wave propagating normal to the PhC reflector can couple to the input plane wave as it has the same parity as the mode. The strength of the coupling hence depends on the mode that is excited during the measurement. In addition, the coupling strength will defer due to the

imperfections of the crystal and finite angular spread of the illuminating beam. Figure 4.7 shows the experimental results of 300 by 300 μm^2 unreleased PhC membrane with square air holes. For square air holes with length of 1035 nm, a reflectance peak of 92.0% is present at 3.60 μm wavelength. The high reflectance region spans across a much smaller bandwidth from 3.58μm to 3.61 μm. Similar to the PhC membrane with circle air holes, when the length of the square air holes increases, the reflectance peak shows blueshift because more area within the membrane becomes air which has a lower refractive index. This causes the band gap region moving towards higher frequencies. After the BOX layer is removed using isotropic etching by VHF, the reflectance is enhanced as shown in Figure 4.8. The measured reflectance for the square air holes with length 1035 nm is 97.2% at 3.59 μm wavelength. Similar blueshift can be seen when the length of the square air holes is increased.

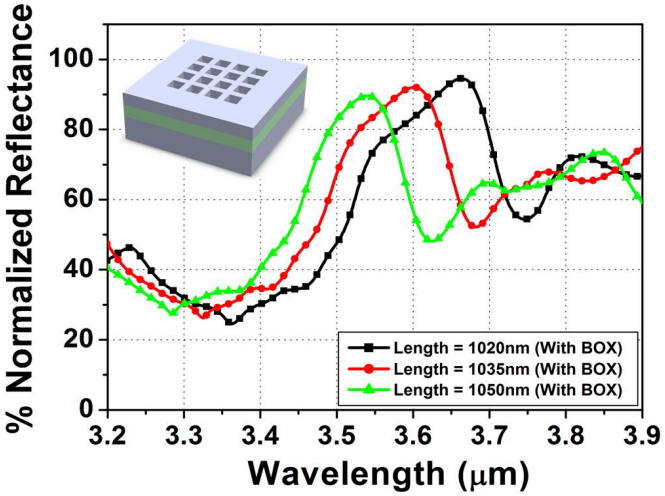

Figure 4.7: Experimental results of stationary square air holes design (with BOX).

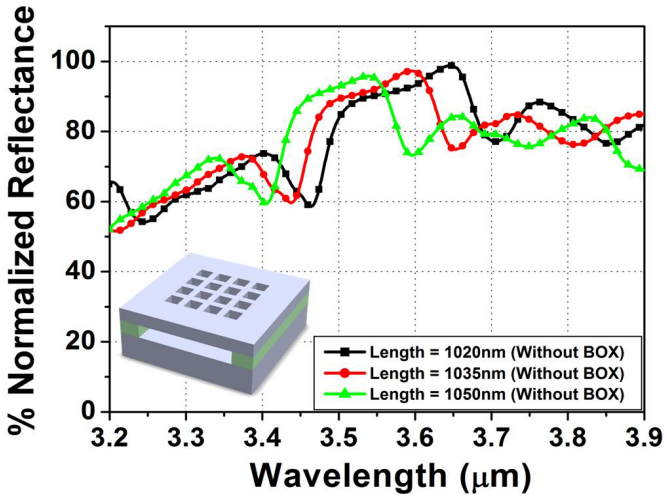

Figure 4.8: Experimental results of released square air holes design (without BOX).

4.4 Si-based Photonic Crystal reflector for high temperature applications

In this section, in order to characterize only the PhC reflector without effects from the underlying Si substrate, we demonstrate a free-standing polycrystalline Si-based PhC membrane where the Si substrate is removed through DRIE. Characterization of both the reflection and the transmission is done at room temperature. Experimental measurements show that around 97% reflection and 3% transmission at a 3.58 μm wavelength are obtained for the PhC membrane. In order to show the feasibility of such a PhC membrane in applications such as down-hole oil drilling, characterization is also done up to 450°C. Due to the high temperature, the peak reflection of the PhC membrane shifts by 75 nm to higher wavelengths. This corresponds to a linear wavelength shift of 0.174 nm/°C. In order to ensure that the peak reflection of the PhC membrane remains around 3.55 μm wavelength, we have demonstrated that the thermo-optic effect can be compensated by altering the dimension of the PhC air holes.

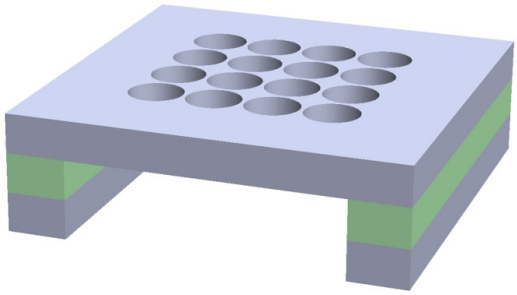

Figure 4.9: Schematic of fully released PhC membrane with etched air holes. The Si substrate and BOX SiO_2 are removed using DRIE and the VHF.

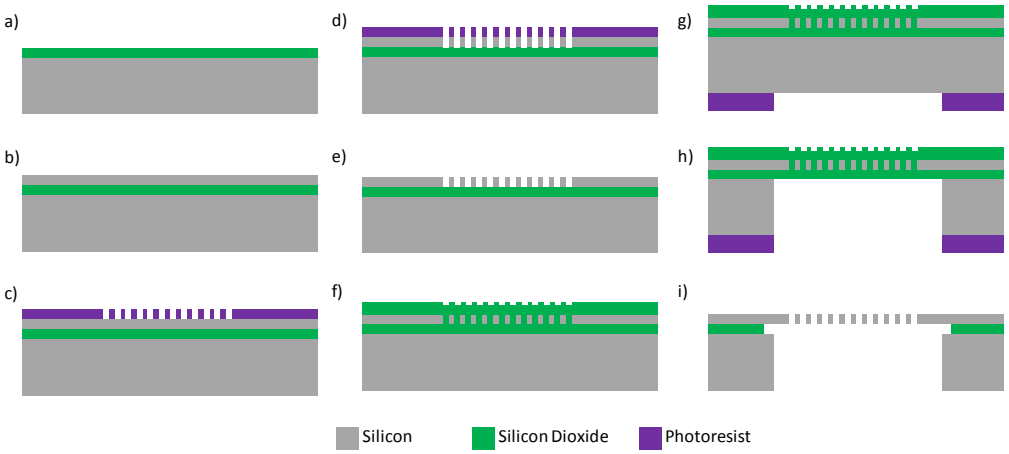

Figure 4.10: Process flow for free-standing PhC based reflector. (a) 1µm thermal SiO_2 is grown on a bare 8" Si wafer. (b) 1µm Si is then grown using LPCVD and annealing is done at 1000°C. (c) Coat and photolithography of PR to define air holes. (d) DRIE of Si to pattern the air holes. (e) PR strip and cleaning of wafer. (f) 1µm SiO_2 is deposited using PECVD. (g) Coat and photolithography of PR on the backside of the wafer. (h) DRIE of Si substrate. (i) PR strip and VHF to realize free-standing PhC reflector.

The design of the polycrystalline free-standing Si-based PhC reflector is shown in Figure 4.9. In order to examine the reflection and transmission characteristics of the PhC membrane, the Si substrate is removed. Similar to previous section, the thickness, **t**, the radius, **r**, and lattice constant, **a**, are designed to be 1 µm, 760 nm and 1.95 µm respectively as shown in (b). Fabrication of the PhC suspended membrane as shown in Figure 4.10 is largely similar to the fabrication steps presented in the previous section. The exception is that a few more steps are included for the removal of the Si substrate. Fabrication begins

with growing a 1 μm thermal SiO_2 at 1050°C on a bare 8" Si wafer (Figure 4.10(a)). The device layer of 1 μm thick polycrystalline Si is then deposited using LPCVD (Figure 4.10(b)). This is followed by a thermal anneal at 1000°C for 30 minutes to reduce the residual stress within the device layer. The air holes are then patterned using deep-UV lithography and etched using DRIE (Figure 4.10(c) and (d)). The PR is then removed and the wafer is cleaned (Figure 4.10(e)). Before proceeding to release the PhC membrane from the Si substrate, the front of the wafer is covered with 1 μm thick PECVD SiO_2 (Figure 4.10(f)). The back of the wafer is then patterned using photolithography and DRIE is used to etch the Si substrate (Figure 4.10(g) and (h)). Finally, the PR is removed and the whole PhC membrane is released using VHF (Figure 4.10(i)). The fabricated free-standing PhC membrane is shown in Figure 4.11. The radius of air hole and lattice constant of PhC structure are observed to be 760 nm and 1.95 μm respectively with little variation along the PhC membrane.

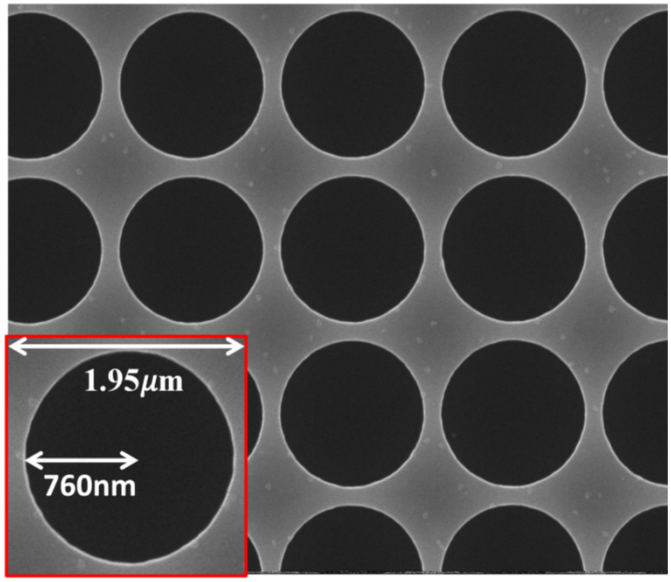

Figure 4.11: SEM image of the fabricated device with r fixed at 760 nm.

4.5 Characterization of free-standing Si-based Photonic Crystal based reflector at room temperature

The simulated reflection result is overlaid with the measurement results as shown in Figure 4.12(a). Generally, the simulated result agrees with the measurement data and both shows high reflection around 3.58 μm. In (b), the transmission characteristic of the PhC membrane is examined. Similar spike is also observed in the transmission spectrum at 3.47 μm and this can once again be attributed to the incidence angle of 45^{o}. From the band structure, low reflection is expected at 3.25 μm due to the presence of a mode at 0.60(2πc/**a**). However, the simulation assumes that prefect coupling will occur which is not true in experimental measurement. The mode is only partially excited and hence a difference result is obtained at 3.30 μm to 3.45 μm. For the wavelengths around 3.70 μm to 3.80 μm, the simulations predicts a high reflection at 3.78 μm due to the bandgap at around 0.495(2πc/**a**). This bandgap is however too narrow and is not excited in the measurement, hence causing a low reflection, rather than a high reflection predicted by the simulation to appear. In both the simulation and measurement, low transmission is shown in wavelength regions that exhibit high reflection.

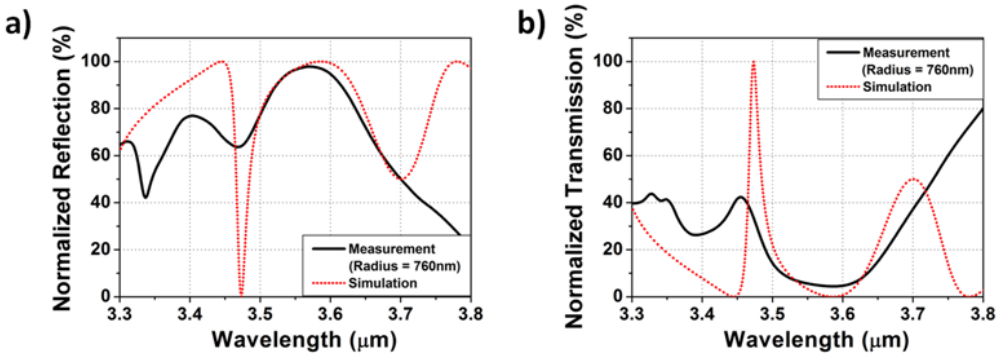

Figure 4.12: (a) Simulated reflection (dashed) being overlaid onto the measurement result (solid) showing the high reflection around 3.55μm wavelength. (b) Simulated transmission (dashed) being overlaid onto the measurement result (solid) showing the low transmission around 3.55μm wavelength.

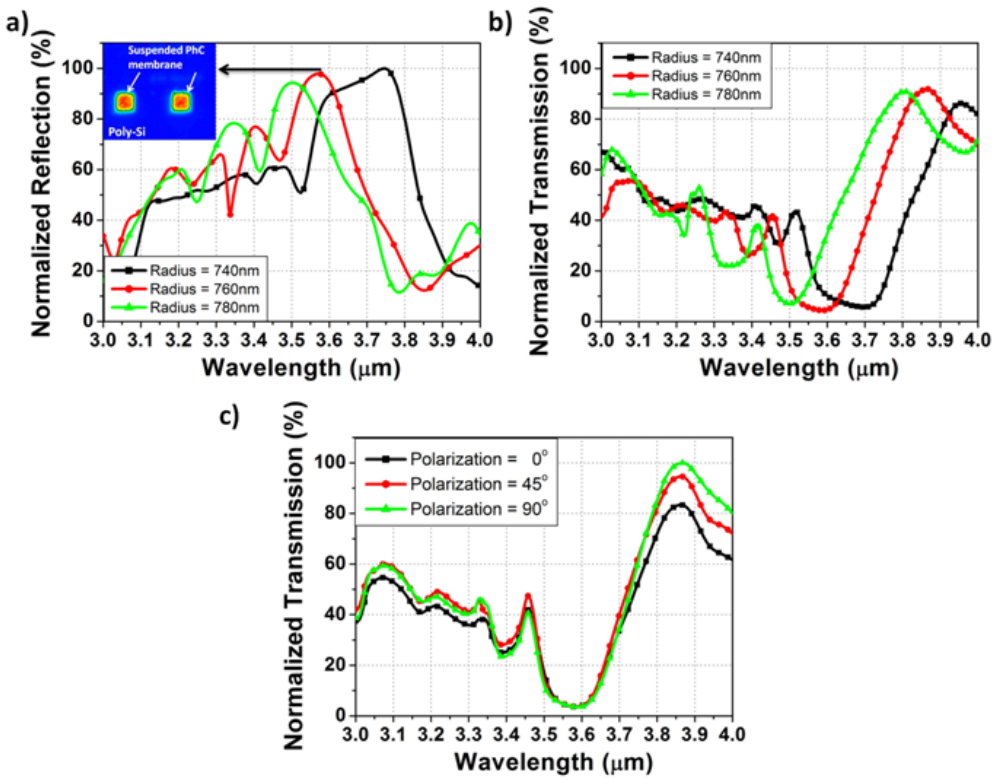

Figure 4.13: Measured reflection of PhC membranes with different air hole radius, r. The inset is the IR image of the sample taken at 3.58□m of the sample when r is 760 nm. (b) Measured transmission of PhC membranes with various air hole radii. (c) Transmission spectra of different polarization angle when r is 760 nm.

Figure 4.13(a) shows the measured reflection spectrum. As **r** increases, it can also be seen that the wavelength of the peak reflection decreases due to the lower

refractive index of the PhC membrane. With the radius of the air hole at 760 nm, the peak reflection wavelength is at 3.58 μm. The dips that appear in the measured reflection are, as mentioned above, due to the 45^{o} angle of incidence of the FTIR microscope used. The inset of (a) indicates the IR image of the PhC membrane at 3.58 μm during measurement. From the diagram, it is conclusive that the peak reflection shown at 3.58 μm wavelength is only due to the PhC suspended membrane. After the Si substrate is removed, the transmission spectra of the PhC membranes are measured and shown in Figure 4.13(b). Again, the measured results are normalized against air and no object is placed along the light path of the source to the MCT detector. Similar to the reflection spectrum, when **r** is fixed at 760 nm, the transmission drops to the lowest value at around 3.58 μm. As **r** increases, the wavelengths at which low transmission is measured also display the tendency to shift to lower wavelengths. While the low transmission in spectrum means the high reflection as well, this indicates that there is low loss within the PhC membrane structure. Besides, the transmission spectra of the PhC suspended membrane with **r** of 760 nm are measured with incident radiation of different polarization angles, namely 0^{o}, 45^{o} and 90^{o} (Figure 4.13(c)). Generally, the three spectra show very similar response over the measured wavelengths. Over the low transmission wavelength region around 3.58 μm, the PhC suspended membrane shows remarkably low dependency on the polarization of the input IR source. As the input IR source in transmission measurement is introduced perpendicularly to the device, the transmission measurements of the device in various polarization angles should ideally be similar. The minute difference displayed in the

measured spectra of the PhC suspended membrane can be mainly attributed to fabrication imperfection.

4.6 Temperature effect on the performance of Si-based PhC membrane

In this work, the thermo-optic effect of the PhC suspended membrane up to 450^{o}C, which is the expected working temperature of the device, is examined and a simple method of altering the dimension of the PhC air holes is deployed to compensate the thermo-optic effect.

The measurement results of PhC membrane with **r** at 760 nm is shown in Figure 4.14(a). At room temperature of 25^{o}C, the peak reflection is around 3.58 μm which is the intended operating wavelength. As temperature increases, the refractive index of the polycrystalline Si in the PhC suspended membrane increases. As predicted by equation (1), it induces a redshift in the peak reflection. At 450^{o}C, the reflection is located at 3.65 μm and also experiences a drop in maximum intensity. The relationship between the shifts in the peak reflection wavelength is plotted in (b). The shift in the wavelength as temperature increases is 75 nm at 450^{o}C. From the linear fit line of the measurement results, it is measured that thermo-optic effect induces a shift of 0.174 nm per degrees Celsius temperature change. Using equation (1), the thermo-optic coefficient can be calculated to be $+1.70\times10^{-4}$ K^{-1} which is near to the value quoted by other works, where $\Delta n/\Delta T = +1.86\times10^{-4}$ K^{-1} [165] and $\Delta n/\Delta T = +1.80\times10^{-4}$ K^{-1} [146].

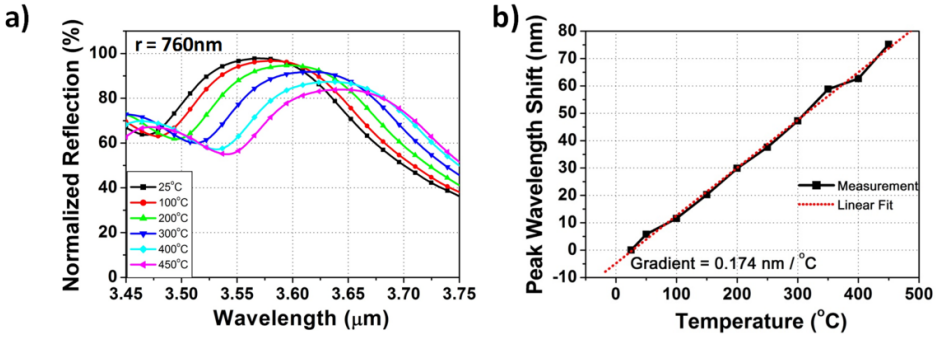

Figure 4.14: (a) Measured reflection of PhC membranes at various temperatures up to 450°C. (b) The relationship between the shift in the peak reflection wavelength against temperature and its corresponding linear fit line.

4.7 Compensation of temperature effect on the performance of Si-based PhC membrane

In order to compensate the thermo-optic effect, a simple methodology is to alter the air hole dimension when designing the device. Based on the measured data, in order to achieve a maximum reflection at 3.55 μm at 450°C, the PhC membrane should show maximum reflection at 3.47 μm wavelength at room temperature. This coincides with the performance of the PhC suspended membrane with **r** of 780 nm.

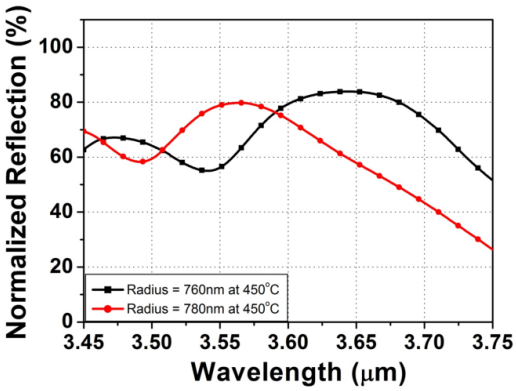

Figure 4.15: Measurement of PhC membrane with r at 760 nm and 780 nm at 450°C.

The measurements of the devices are shown in Figure 4.15. As expected, the reflection displayed by PhC suspended membrane with **r** at 780 nm shows a peak reflection at around 3.56 μm. This shows that the thermo-optic effect which causes the reflection to redshift has been compensated through simple alteration of the dimension of the air holes. Based on this methodology of optimizing the air hole radius of the PhC suspended membrane, desired optical performance can be achieved at various temperatures. This is important for industrial applications such as gas sensing in the down-hole oil drilling process where high temperatures are expected.

4.8 AlN-based Photonic Crystal reflector for athermal operations

With a relatively high thermo-optic coefficient of $+1.70\times10^{-4}$ K^{-1}, Si is unsuitable for applications with high as well as changing operating temperatures. In order to minimize the impact of such temperature changes for applications where such thermo-optic effect is detrimental, research are done to compensate the refractive index change in the material [153]. For example, research has been done to introduce polymer cladding, which have negative thermo-optic coefficient, to the photonic device [152, 153, 166, 167]. However as mentioned before, such method faces the problem of integration with CMOS process, as well as reliability concerns due to high sensitivity on the polymer thickness. Other methods such as the use of temperature feedback circuits increase the power usage and require larger footprint [152]. In view of these problems, it is largely desired to have a CMOS compatible material to be used

as the photonic device and also achieve high independence from operating temperature changes.

Due to progression in epitaxial film deposition, research involving the use of AlN as photonic material has gained speed even in out-of-plane applications. More importantly, AlN has a high thermal conductivity (κ_{AlN} = 285 W/m.K) and small thermo-optic coefficient (dn/dT = $+2.32\times10^{-5}$ K^{-1}) compared to Si [132]. This makes AlN very attractive as a new material to be used in photonic designs for applications with fluctuating operating temperatures. In this section, we present the design and characterization of an AlN based PhC reflector working in the MIR wavelengths. The study on using AlN as the material for a 2-D PhC reflector is lacking currently, especially at elevated temperatures. We also designed the peak reflection wavelength to be around 3.50 μm. Through our measurement, high reflection of more than 90% was observed from 3.08 μm to 3.78 μm. Due to the relatively low refractive index of AlN (n_{AlN} = 2.2), we also employed the use of sacrificial layer release of SiO_2 to enhance the performance of the PhC. Characterization of the AlN based PhC reflector is done up to 450^{o}C to examine the effect of such temperature changes on the performance of the AlN based PhC. From experimental results, despite the increasing temperature to 450^{o}C, the redshift in the peak reflection of the PhC is estimated to be 14.1 nm. In comparison, the redshift in the peak reflection wavelength of a Si based PhC is 75 nm. Such insensitivity to thermo-optic effect makes AlN based PhC a promising technology to be used as photonic components for high temperature applications. The design of the AlN based PhC is shown in Figure 4.16(a). The

AlN based PhC is make up of a suspended AlN slab with a thickness of 330 nm. The BOX is 1 µm and acts as a sacrificial layer. Periodic patterning of air holes is etched into the slab, with the radius of each air hole being 620 nm and the period being 1.95 µm.

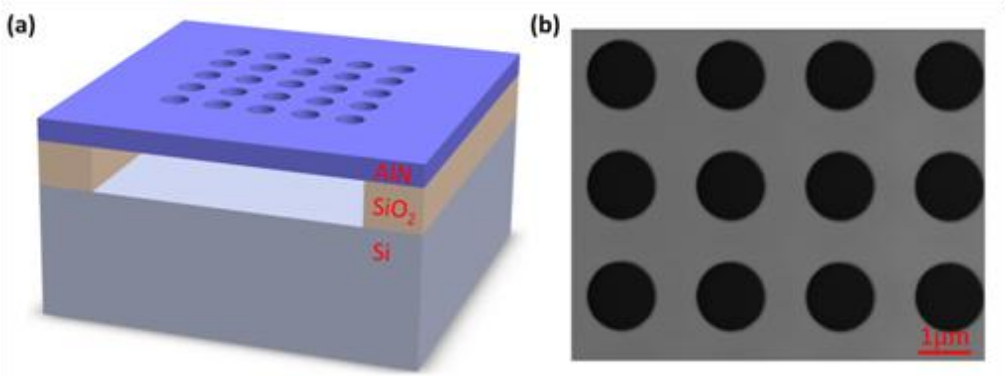

Figure 4.16: .(a) Schematic drawing of the suspended AlN PhC slab, and (b) SEM image of the fabricated AlN PhC slab.

Fabrication of the device begins with an 8" bare Si wafer and the BOX is deposited using PECVD. A 330 nm thick polycrystalline AlN layer is then deposited on the BOX using sputtering. The air holes are defined using photolithography and the AlN slab is etched using reactive ion etching (RIE). Finally, the AlN based PhC is made suspended when the BOX layer is removed by utilizing VHF. The SEM image is shown in Figure 4.16(b). The fabricated device matches very highly with the designed parameters with the radius of the air holes being 620 nm and the period 1.95 µm. Through cross-sectional analysis of etched AlN PhC slab, it is seen with a sloping sidewall with a measured angle of 79.8^{o}. This is taken into account for the subsequent simulations. While the radius at the top of the membrane is maintained at the designed value, the radius of the air hole at the bottom of the membrane is drawn to be 60 nm smaller to

account for the effect of the sloping sidewall. The refractive index of AlN after deposition through sputtering was also measured using ellipsometry. Based on the measurement, the refractive index of the AlN film is 2.2. This is close to values reported for the refractive index of AlN which are 2.12 [132] and 2.10 [168].

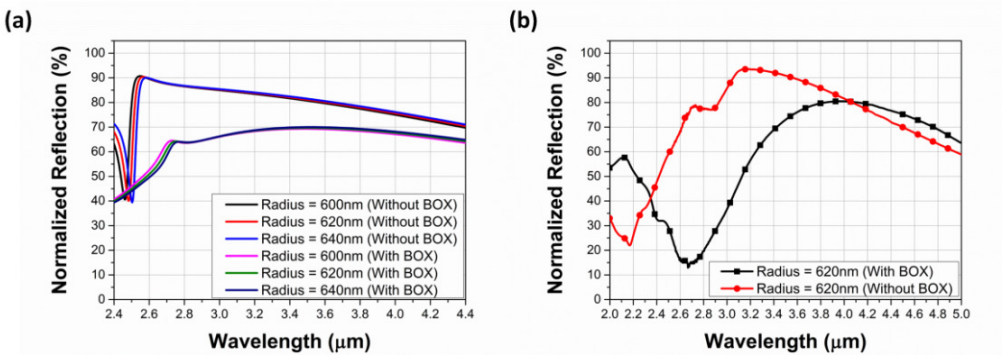

Figure 4.17: (a) FDTD simulation of the AlN based PhC with various air hole radii and (b) experimental measurement of the AlN based PhC device with underlying BOX and without the BOX layer.

Simulation of the AlN based PhC is done using FDTD method. The simulated results of the PhC with various air hole radii are presented in Figure 4.17(a), where the refractive index of AlN is set to 2.2 and periodic boundary conditions are set on the sides of the unit cell. Based on the simulation, high reflection is expected from the AlN based PhC around 2.58 μm when the AlN layer is released. As the radius of the air hole increases, the peak reflection wavelength experiences a redshift. With the presence of the BOX layer, in addition to a redshift of the peak reflection wavelength, the reflection drops sharply as well. Reflection measurement of the AlN based PhC is done using the FTIR Microscope from 2 μm to 5 μm. The effect of BOX on the performance of the AlN based PhC is examined in Figure 4.17(b). As shown, the measurement results of the AlN based PhC with air hole radius of 620 nm is presented. When

the BOX layer is removed by using the abovementioned method of etching through the use of VHF, more than 90% reflection is measured from 3.08 μm to 3.78 μm. When the BOX layer is present, the peak reflection redshifts to higher wavelengths due to the increase of the refractive index of the cladding layer below the AlN based PhC membrane from 1 (air) to 1.44 (SiO_2). This leads to an increment of the effective refractive index of the device and hence moves the peak reflection wavelength to higher wavelength. In addition, with the presence of the BOX layer, the peak intensity of the measured reflection is only 81% which is significantly lower than the peak reflection of 96% when the BOX layer is removed. This is likely due to the low refractive index of AlN of 2.2. When the AlN based PhC is in contact with the BOX layer, there is high leakage into the BOX layer as it has a relatively high refractive index of 1.44. This exemplifies the importance of etching of BOX layer in order to enhance the performance of the AlN based PhC.

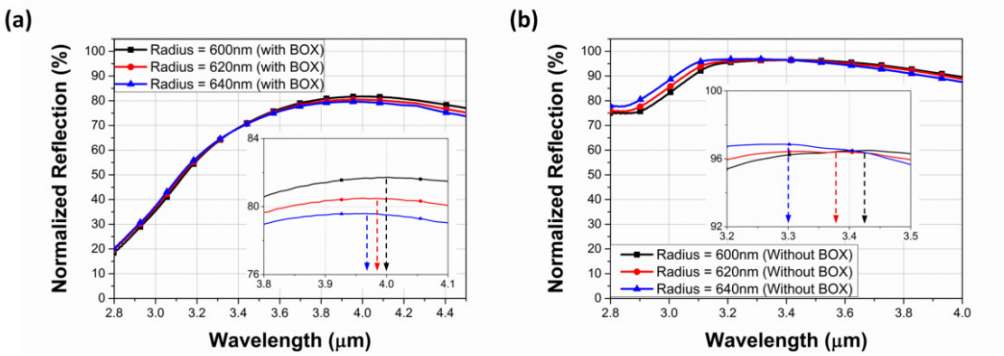

Figure 4.18: (a) Experimental measurement of the effect of the change in the air hole radius on the performance of the AlN based PhC device (a) with underlying BOX and (b) without the BOX layer.

The effect of the change in the air hole radius on the performance of the AlN based PhC is also examined. The measurement was taken at room temperature (25ºC) with higher resolution and the results are shown in Figure 4.18. As

presented, when the radius of the air hole increase from 600 nm to 640 nm, the peak reflection peak of the AlN based PhC blueshifts due to a decrease in the effective refractive index of the membrane with the replacement of AlN with air. For the AlN based PhC with BOX, the shift in the reflection is around 36 nm from 4.00 μm to 3.96 μm. When the BOX is removed by using VHF, the reflection wavelength of the released AlN based PhC experience a blueshift from 3.43 μm to 3.30 μm. This equates to a shift of 130 nm with the same radius change of the air hole. The seemingly lower shift in the peak reflection wavelength in the AlN based PhC with BOX can be attributed to the higher overall effective refractive index of the membrane. The change in the radius of the air hole brings about a much lower percentage change in the effective refractive index of the AlN based PhC with BOX than its counterpart without BOX. This thus has a smaller change in the peak reflection wavelength. Overall, the wavelength shift of the peak reflection is small considering the operating wavelength of the AlN based PhC. This indicates an added advantage of higher fabrication variation tolerance when using AlN.

Thermo-optic effect on the AlN based PhC is also done by placing the released membrane on a heating stage up to 450^{o}C. Similar to the procedure used in Si based PhC reflector, at each temperature step, the AlN based PhC is left untouched in the chamber for ten minutes before measurement is taken. However, as the thermo-optic coefficient of AlN is expected to be much lower than Si, the changes of the reflection spectra across different temperature steps is also expected to be small. In order to ensure that such small changes are

captured in the measurements, a high resolution scan is employed. Instead of the more typically used resolution of $4cm^{-1}$, the resolution set in this measurement is $0.09cm^{-1}$ which is the highest that can be set in the FTIR microscope. At wavelengths around 3.1μm, the wavelength step attainable is 0.08 nm. This is sufficient to detect any small changes in the reflection measurement of the device. The downside of such a high resolution scan is the time taken for each measurement which is around ten minutes. A more detailed background scan is also required to ensure that the additional noise measured are filtered away. The measurement of the AlN based PhC with air hole radius of 620 nm under various temperature conditions are shown in Figure 4.19. At room temperature (25^oC), the peak reflection wavelength of the AlN based PhC with air hole radius of 620 nm is around 3.29 μm. As the temperature increases, based on equation (1), the refractive index of AlN also increases. This raises the effective refractive index and induces a redshift in the peak reflection wavelength. At 450^oC, the peak reflection wavelength of the AlN based PhC is around 3.31 μm, with a 14.1 nm redshift in wavelength. With n_0 and λ_0 being 2.2 and 3.29 μm respectively, the thermo-optic coefficient is estimated to be $+2.22\times10^{-5}\ K^{-1}$, which is an order of magnitude lower than Si [153]. Even at elevated temperatures, the low thermo-optic coefficient of AlN ensures that the peak reflection wavelength does not change drastically.

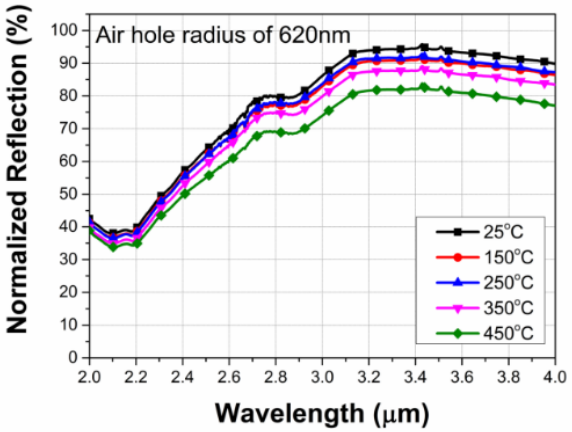

Figure 4.19: Measurement of the AlN based PhC of air hole radius of 620 nm under various temperatures.

4.9 Conclusion

We have shown the use of polycrystalline Si to be used as a 2-D PhC reflector. Two designs of 2-D PhC based polycrystalline Si membranes have been demonstrated as ultra-compact Si based reflector. Both the circle air holes and square air holes designs were measured to show 96.5% and 97.2% reflectance around 3.58μm, which is an important wavelength for hydrocarbon gas sensing in the MIR region. While not sacrificing optical performance, PhC with square air holes offers more mechanical strength due to its lower filling factor of 36%.

We have also presented the fabrication of a PhC reflector with the substrate removed to thorough characterizes the performance of the PhC reflector at high temperatures. The measured reflection and transmission spectra of the PhC suspended membrane indicate that around 97% reflection and 3% transmission at 3.58μm wavelength are obtained at room temperature. Measurements done at 450^{o}C reveal that thermo-optic effect induces a linear shift of 0.174 nm per degrees Celsius temperature change. The thermo-optic coefficient is calculated

as $+1.70\times10^{-4}$ K^{-1}. In order to compensate the redshift of 75 nm induced by the thermo-optic effect, a simple methodology of changing the air hole dimension is feasible. Measured data of the PhC suspended membrane with **r** of 780 nm at 450^{o}C support the fact that such thermo-optic effect is compensated.

In order to passively correct the shift introduced by thermo-optic effect at all temperatures, an AlN based PhC is fabricated and characterized as a highly reflective mirror working in the MIR wavelengths. The AlN slab is designed to be 330 nm thick and the air hole radius is varied from 600 nm to 640 nm. Through measurement, the PhC with air hole radius of 620 nm is shown to have greater than 90% reflection across 3.08 μm to 3.78 μm, with the peak reflection of 96% at 3.16 μm. Characterization of the AlN based PhC is also performed at 450^{o}C to examine the thermo-optic effect. Due to the minute increase in the refractive index of AlN at elevated temperatures, it is measured that the peak reflection redshift by 14.1 nm when the temperature is at 450^{o}C. The thermo-optic coefficient is estimated as $+2.22\times10^{-5}$ K^{-1}. This is an order of magnitude lower than Si and is hence significantly better performing in high operating temperatures. This highlights the suitability of using AlN over Si as a photonic material especially when the applications involve temperature fluctuations.

CHAPTER 5: Photonic Crystal based Fabry-Perot Filter

5.1 Introduction

In the previous chapter, we have described our work in realizing high performance PhC. By using these PhC mirrors in the formation of the FPF. FPF is an important device that is widely used in sensing applications such as gas sensing. The Q-factor obtained in the FPF by using PhC mirrors can be much higher than conventional methods. In this chapter, we will demonstrate the design, fabrication and characterization of a FPF which is fabricated using a CMOS-compatible monolithic fabrication process which is highly desirable [112]. In this section, we will introduce the optimization steps that were taken in the fabrication process in order to realize the FPF. Several failures were experienced before the fabrication process was fixed. In our previous section where we fabricated the PhC mirror, the process used involved a high temperature anneal of 1000^{o}C. The annealing step induces very high thermal stress and this causes cracking of the silicon layers and wafer breakage. A single etch process was also attempted to define both PhC mirrors but this was also found to be unsuccessful. Details of these fabrication attempts will be discussed in the following section. In the end, we alleviate the thermal stress issue through the use of low stress epitaxial polycrystalline Si which is deposited at a lower temperature of 610^{o}C and a bottom-up approach in the realization of the FPF. The fabricated FPF show a transmission peak centered at 3.51 μm with a Q-factor of around 300. While this is lower than simulations, it is still significantly

higher than existing works which typically have Q-factor of few tens [114, 117, 118]. This opens the possibility of utilizing such PhC FPF for high-resolution applications like gas sensing [113, 169] and hyperspectral imaging [115, 118].

5.2 Theory of Fabry-Perot Filter

The FPF comprises of two flat and highly reflective mirrors which with an air gap between them. Thus, the FPF can be considered to be a system with 3 mediums. The individual mediums can first be considered as shown in Figure 5.1. For an incoming beam from Medium 1 striking on the interface between Medium 1 and 2, the beam can be characterized with complex reflection amplitude, $\mathbf{r_1}$, and complex transmission amplitude $\mathbf{t_1}$. Likewise, for an incoming beam from Medium 2 incidence on the interface between Medium 1 and 2, the beam is undergoes reflection back into Medium 2 with complex reflection amplitude, $\mathbf{r_1'}$, and transmission into Medium 1 with complex transmission amplitude $\mathbf{t_1'}$. Finally, when a beam from Medium 2 strikes the interface between Medium 2 and 3, the complex reflection amplitude is $\mathbf{r_2}$ and the complex transmission amplitude is $\mathbf{t_2}$.

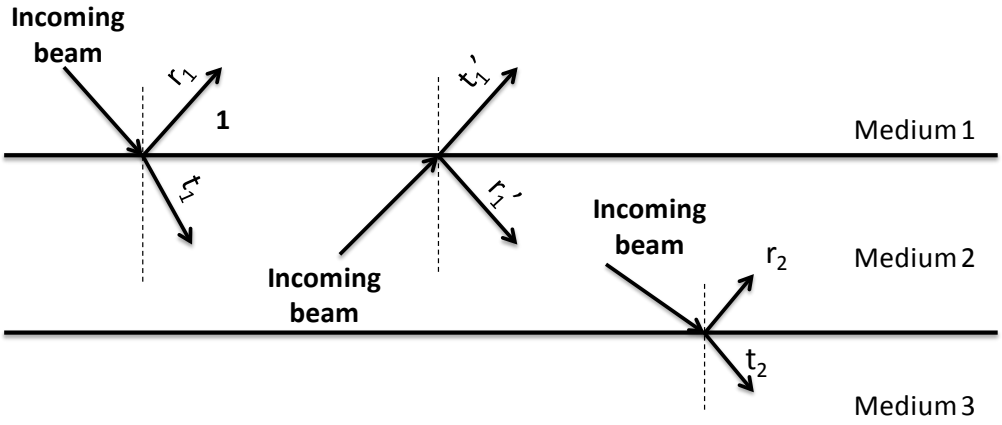

Figure 5.1: The three individual mediums of the FPF system with the

various complex reflection amplitudes and complex transmission amplitudes when incoming beam originated from different mediums

The FPF is characterized by its overall reflectance, **R** and transmittance, **T**. Both **R** and **T** are Poynting's vectors of the portion of energy reflected and transmitted respectively. In order to obtain **R** and **T** of the FPF, we consider that the incoming beam from Medium 1 strikes the interface between Medium 1 and 2 and resonates within Medium 2 before transmitting through into Medium 3. This causes it to incident repeatedly within the two interfaces (n times) as shown in Figure 5.2. The distance between the interfaces is fixed at **d**. At every incidence onto the interfaces, a portion of the complex amplitudes travel into either Medium 1 or Medium 3.

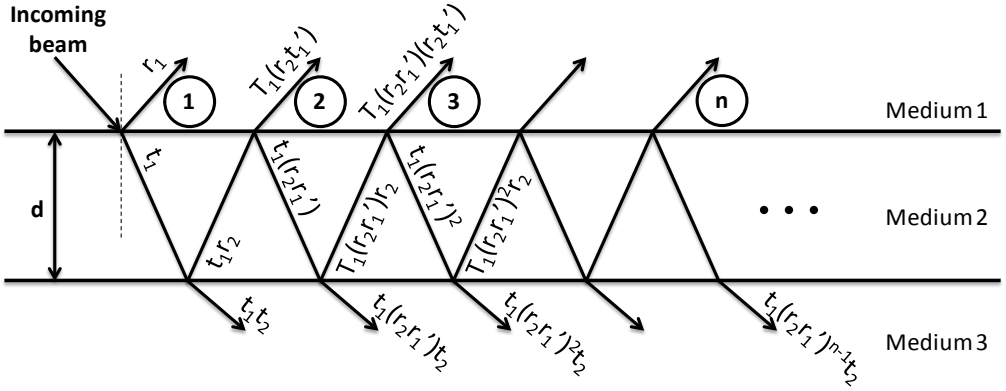

Figure 5.2: The FPF system with an incoming beam from Medium 1 and resonating within Medium 2. The overall reflection amplitude of the FPF can be obtained by summing all the complex reflection amplitudes into Medium 1 and the overall transmittance amplitude is obtained by summing all the complex transmittance amplitudes into Medium 3

Since Medium 1 and Medium 3 are the same, we can simplify the amplitude components to

$$\boldsymbol{r_1' = r_2 = r}$$

$$\boldsymbol{r}_1' = -\boldsymbol{r}_1$$

$$\boldsymbol{r}_2 = -\boldsymbol{r}_1$$

$$\boldsymbol{t}_1' = \boldsymbol{t}_1 = \boldsymbol{t}$$

$$\boldsymbol{t}_1\boldsymbol{t}_1' = 1 - \boldsymbol{r}^2$$

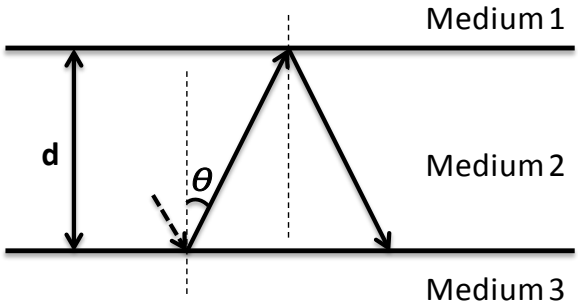

Figure 5.3: Geometry of the system to determine the phase difference between two successive transmitted waves

As shown in Figure 5.3, based on the geometry of the system, the phase difference between two successive transmitted waves can be defined as

$$\delta = \frac{2\boldsymbol{d}\cos\theta}{\lambda_0/n_0}2\pi$$

In order to obtain the overall reflection amplitude of the FPF, $\mathbf{r}_{FPF}$, we sum all the individual complex reflection amplitudes travelling into Medium 1 when the incoming beam strikes the interface between Medium 1 and Medium 2. The overall reflection amplitude is given as follows

$$\boldsymbol{r}_{FPF} = \boldsymbol{r}_1 + \boldsymbol{t}_1(\boldsymbol{r}_2\boldsymbol{t}_1')e^{-i\delta} + \boldsymbol{t}_1(\boldsymbol{r}_2 r_1')(\boldsymbol{r}_2\boldsymbol{t}_1')e^{-i2\delta} + \cdots$$

$$+ \boldsymbol{t}_1(\boldsymbol{r}_2 r_1')^{n-2}(\boldsymbol{r}_2\boldsymbol{t}_1')e^{-i(n-1)\delta} + \cdots$$

$$= \boldsymbol{r}_1 + \frac{\boldsymbol{t}_1(\boldsymbol{r}_2\boldsymbol{t}_1')e^{-i\delta}}{1 - \boldsymbol{r}_2\boldsymbol{r}_1'e^{-i\delta}}$$

$$= \frac{\boldsymbol{r}_1 + \boldsymbol{r}_2e^{-i\delta}(-\boldsymbol{r}_1\boldsymbol{r}_1' + \boldsymbol{t}_1\boldsymbol{t}_1')}{1 - \boldsymbol{r}_2\boldsymbol{r}_1'e^{-i\delta}}$$

$$= \boldsymbol{r}_1 + \frac{\boldsymbol{r}_1 + \boldsymbol{r}_2 e^{-i\delta}}{1 + \boldsymbol{r}_1 \boldsymbol{r}_2 e^{-i\delta}}$$

The overall reflectance, **R** of the FPF can be calculated as follows

$$\boldsymbol{R} = \boldsymbol{r}_{FPF}{}^2 = \frac{\left(\boldsymbol{r}_1 + \boldsymbol{r}_2 e^{-i\delta}\right)\left(\boldsymbol{r}_1 + \boldsymbol{r}_2 e^{+i\delta}\right)}{(1 + \boldsymbol{r}_1 \boldsymbol{r}_2 e^{-i\delta})(1 + \boldsymbol{r}_1 \boldsymbol{r}_2 e^{+i\delta})}$$

$$= \frac{(\boldsymbol{r}_1 + \boldsymbol{r}_2)^2 - 4\boldsymbol{r}_1 \boldsymbol{r}_2 \sin^2 \frac{\delta}{2}}{(1 + \boldsymbol{r}_1 \boldsymbol{r}_2)^2 - 4\boldsymbol{r}_1 \boldsymbol{r}_2 \sin^2 \frac{\delta}{2}}$$

$$= \frac{4|\boldsymbol{r}|^2 \sin^2 \frac{\delta}{2}}{(1 - |\boldsymbol{r}|^2)^2 + 4|\boldsymbol{r}|^2 \sin^2 \frac{\delta}{2}}$$

Likewise, in order to obtain the overall transmission amplitude of the FPF, $\mathbf{t}_{FPF}$, we sum all the individual complex transmission amplitudes travelling into Medium 3 when the incoming beam strikes the interface between Medium 2 and Medium 3. The overall transmission amplitude is given as follows

$$\boldsymbol{t}_{FPF} = \boldsymbol{t}_1 \boldsymbol{t}_2 + \boldsymbol{t}_1 (\boldsymbol{r}_2 \boldsymbol{r}_1') \boldsymbol{t}_2 e^{-i\delta} + \boldsymbol{t}_1 (\boldsymbol{r}_2 \boldsymbol{r}_1') \boldsymbol{t}_2 e^{-i2\delta} + \cdots$$

$$+ \boldsymbol{t}_1 (\boldsymbol{r}_2 \boldsymbol{r}_1')^{n-1} \boldsymbol{t}_2 e^{-i(n-1)\delta} + \cdots$$

$$= \frac{\boldsymbol{t}_1 \boldsymbol{t}_2}{1 - \boldsymbol{r}_2 \boldsymbol{r}_1' e^{-i\delta}}$$

The overall transmittance, **T** of the FPF can be calculated as follows

$$\boldsymbol{T} = \boldsymbol{t}_{FPF} \boldsymbol{t}_{FPF}{}^* = \frac{\boldsymbol{t}_1{}^2 \boldsymbol{t}_2{}^2}{(1 - \boldsymbol{r}_2 \boldsymbol{r}_1' e^{-i\delta})(1 - \boldsymbol{r}_2 \boldsymbol{r}_1' e^{+i\delta})}$$

$$= \frac{\boldsymbol{t}_1{}^2 \boldsymbol{t}_2{}^2}{(1 - \boldsymbol{r}_2 \boldsymbol{r}_1')^2 + 4\,\boldsymbol{r}_2 \boldsymbol{r}_1' \sin^2 \frac{\delta}{2}}$$

$$= \frac{\boldsymbol{t}_1{}^2 \boldsymbol{t}_2{}^2}{(1 - \boldsymbol{r}_2 \boldsymbol{r}_1')^2 + 4\,\boldsymbol{r}_2 \boldsymbol{r}_1' \sin^2 \frac{\delta}{2}}$$

$$= \frac{\boldsymbol{t_1}^2\boldsymbol{t_2}^2}{(1-\boldsymbol{r_2}\boldsymbol{r_1'})^2}\frac{1}{1+\boldsymbol{F}\sin^2\frac{\delta}{2}}$$

where

$$\boldsymbol{F} = \frac{4\boldsymbol{r_2}\boldsymbol{r_1'}}{(1-\boldsymbol{r_2}\boldsymbol{r_1'})^2}$$

F is also known as the coefficient of finesse and is an indication of the Q-factor of the filtered peak. When the reflectance of the mirrors is high, the finesse of the FPF increases and high Q-factor of the filtered peak can be obtained. Also, when we assuming normal incidence of the incoming beam, ie. $\theta = 0^{\circ}$, maximum overall transmittance occurs when **d** is set to half of an integer multiple of the wavelength.

5.3 Simulation of Fabry-Perot Filter

In this section, the feasibility of implementing 2-D PhC designs as high reflectivity mirror in FPF is explored using FDTD simulations. As discussed, such high reflectivity mirrors are commonly implemented using multi-layer structures which faces the problem of high residual stress in the layers. In contrast, 2-D PhC designs are able to achieve high reflectivity using a thin Si membrane which is light weight and easy to fabricate. We have also verified in previous chapter that the PhC reflector is able to show extremely high reflection at any desired wavelength just by altering the geometry of the design. The schematic of our designed FPF is shown in Figure 5.4(a). The PhC membranes are used as the mirrors and the top Si PhC membrane is supported using springs.

The cavity length can be made tunable by using MEMS techniques like applying a voltage difference between the top and bottom Si slab. This induces an attractive electrostatic force which will pull the top and bottom slabs towards each other, hence reducing the gap between them. More discussion on the design of the spring will be done in later chapter.

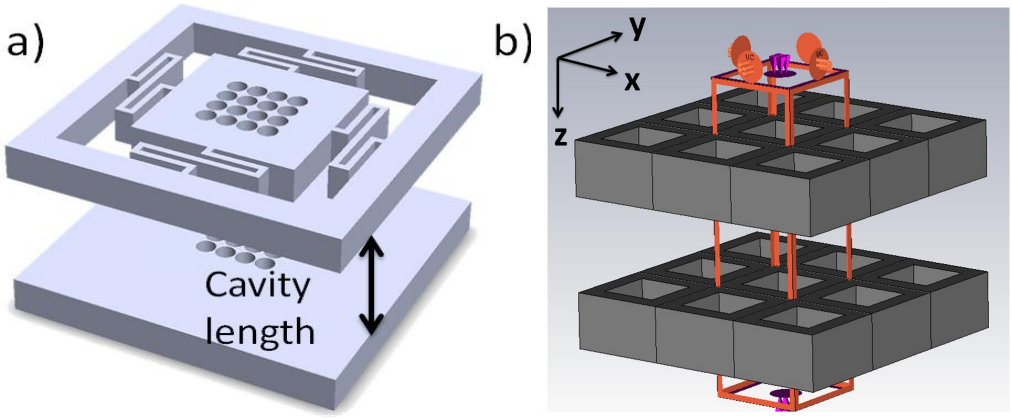

Figure 5.4: (a) Schematic of FPF using PhC reflector as mirrors and (b) model of PhC based FPF used in simulation programme, CST MWS.

The transmission output of the FPF as the cavity length changes is simulated. The simulation model is shown in Figure 5.4(b). Only the unit cell indicated by the red box is simulated and periodic boundary condition is set on all four sides. This helps to reduce computation time while maintaining high accuracy in the simulated output. In the previous chapter, we have shown the possibility of using both circle and square holes in the PhC reflector design. In order to show their feasibility, of using square air holes to be used in FPF, we will simulate the performance of the FPF with PhC reflector with circle and square air holes. In Figure 5.5, the simulated spectrum of the FPF using circle air holes is presented. In the simulations, the inputted light is propagating along the z direction and the electric field is along the x direction. The radius of the circle

air hole is 770 nm and the lattice constant is 1.95 µm. The thickness of the top and bottom Si slabs are maintained at 1µm. The full-width half-maximum (FWHM) of the transmittance peak corresponding to a cavity length of 2.00 µm is 0.07 nm which equates to a Q-factor of about 52000. The tuning range of the FPF is 28 nm from 3.68 µm to 3.71 µm when the cavity length is changed 1.95 µm to 2.05 µm. This is around an order of magnitudes higher than the simulated Q-factor of FPF using multi-layered structures [114, 117, 119].

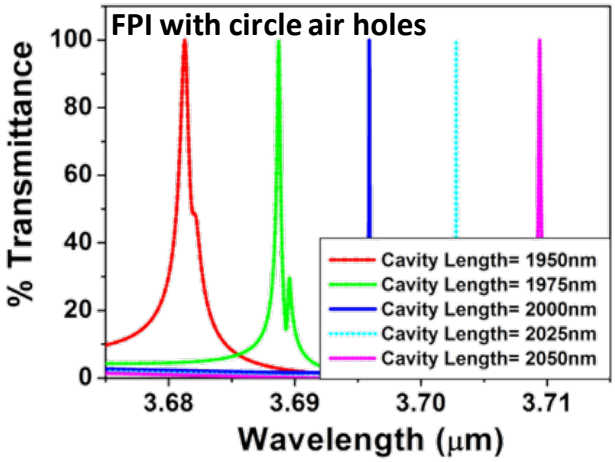

Figure 5.5: Simulated transmittance of the FPF with various cavity length using circle air holes.

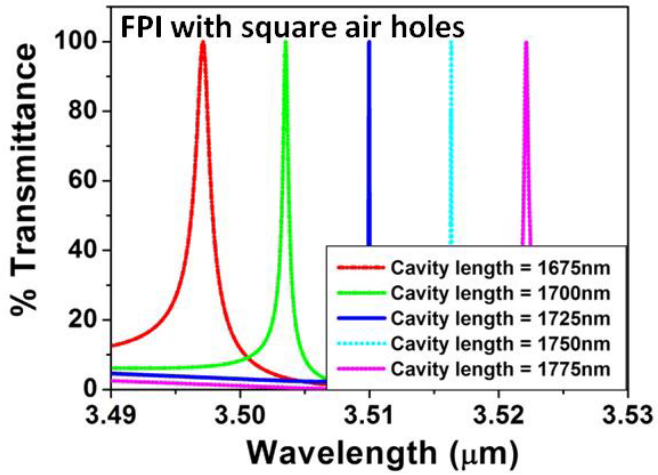

Figure 5.6: Simulated transmittance of the FPF with various cavity length using square air holes.

In order to fully assess the practicability of using square air holes in FPF, FPF

with square air holes reflector are also simulated for comparison using similar method mentioned above. The values of **L**, **a** and **t** are 1.05 μm, 1.70 μm and 1 μm respectively. The simulated results are presented in Figure 5.6. The FPF shows a tuning range of 25nm from 3.50μm to 3.52μm when the cavity length is changed 1.675 μm to 1.775 μm. When the cavity length is 1.725 μm, the FWHM of the simulated peak is 0.08 nm which corresponds to a Q-factor of 43800. Based on the simulations of the FPF using both circle air holes and square air holes, it has been shown the proposed PhC designs are ideal candidates for the realization of the high reflectivity mirrors. At the same time, the use of PhC with square air holes in FPF also displays good optical performance which is comparable to PhC with circle air holes. As described in pervious section, using PhC with square air holes offers higher mechanical strength which is vital in applications such as FPF where the PhC reflectors are free-standing. In summary, the comparison between PhC reflector and multi-layer Bragg reflector when used as mirror in FPF are summarized in Table 7 below.

Table 7: Comparison of PhC and Bragg reflector when used in FPF

PhC Reflector	Bragg Reflector
Simple fabrication process without bonding process	Complex fabrication process involving bonding process and possible stress issue
High reflectivity achieved using one single Si slab hence low power actuation is possible	High power needed for actuation due to thick multi-stack mirror
Wide range of materials available	Limited choice of materials available
Very high Q-factor output when used in FPF	Low Q-factor output when used in FPF

In this thesis, we have developed the process flow where the FPF is fabricated using a monolithic procedure which will be detailed later. This removes the need of the bonding process which is typically used in FPF that uses Bragg reflector. This is due to the number of layers needed for multi-stacked mirrors which makes it impractical due to high stress issues to make the process flow monolithic. The use of PhC reflector allows the realization of a light-weight mirror component that is suitable for low power actuation to change the cavity length for a tunable output. The light-weight nature of the device also allows for a lower actuation power. This is in contrast with Bragg mirror which is formed by multiple layers of different materials which results in a much heavier mirror. This causes the actuation power needed to be much higher. In order to realize the PhC reflector, various materials such as Si, AlN and SiN can be used. In this thesis, Si is used due to its prevalent presence in CMOS foundries. However, for Bragg reflector, it is formed by depositing thin layers of two alternating materials with high and low refractive indices. The larger the difference between the refractive indices of the two materials, the Bragg reflector will display higher reflection. This limits the choice of materials that are suitable. Simulations also show that the Q-factors by FPF that uses PhC reflectors are very high. This is due to the bandwidth of around 160 nm which has more than 90% reflection in PhC reflector. This makes the PhC reflector able to filter unwanted wavelengths more efficiently than the multilayer Bragg reflector, hence resulting in higher Q-factor.

5.4 Fabrication of Photonic Crystal based Fabry-Perot filter

In order to fabricate the PhC based FPF, we propose a monolithic approach to the fabrication process in order to avoid any physical bonding of the mirrors which is usually used in existing works. Such monolithic fabrication approach provides simplicity and low-risk fabrication which can be achieved across the whole wafer. The schematic of the proposed PhC FPF to be fabricated is shown in Figure 5.7.

The first fabrication process proposed was a continuation of the steps used in the previous chapter where we used LPCVD Si and annealing at 1000^{o}C. We also attempted to use a single etch step to define both PhC mirrors in order to prevent the use of chemical mechanical polishing (CMP) of SiO_2. The effect of the CMP process will be highlight in subsequent section. The detailed fabrication steps are shown in Figure 5.8. Fabrication of the FPF starts with a 1 μm PECVD SiO_2 on a bare Si wafer as shown in Figure 5.8(a). Then a 1 μm LPCVD Si (Figure 5.8(b)) and 1.72 μm PECVD SiO_2 is deposited (Figure 5.8(c)). This 1.72 μm SiO_2 defines the Fabry-Perot cavity length between the two PhC mirrors. To form the upper PhC mirror, another 1 μm LPCVD Si is deposited and the wafer is annealed at 1000^{o}C (Figure 5.8(d)). Photolithography is then done to define the air holes (Figure 5.8(e)) and DRIE is done to etch both the Si mirror layer and SiO_2 layer (Figure 5.8(f)). The PR is then stripped and the wafer cleaned (Figure 5.8(g)). Finally, VHF is used to remove the SiO_2 in order to form the FPF (Figure 5.8(h)). When attempting the proposed fabrication, two critical problems were faced. The first is the thermal stress that occurs during the annealing step in Figure 5.8(d). Unlike previous fabrication

flow which includes only one layer of Si, the $SiO_2/Si/SiO_2/Si$ stack in this case cracks more readily at high temperature as shown in Figure 5.9. While not all the wafers crack after annealing, the high temperature anneal is a high risk process for the fabrication of the FPF.

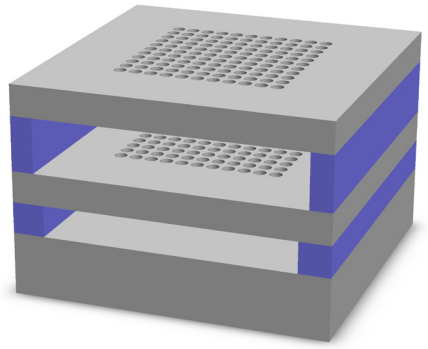

Figure 5.7: Schematic of the PhC based FPF to be fabricated.

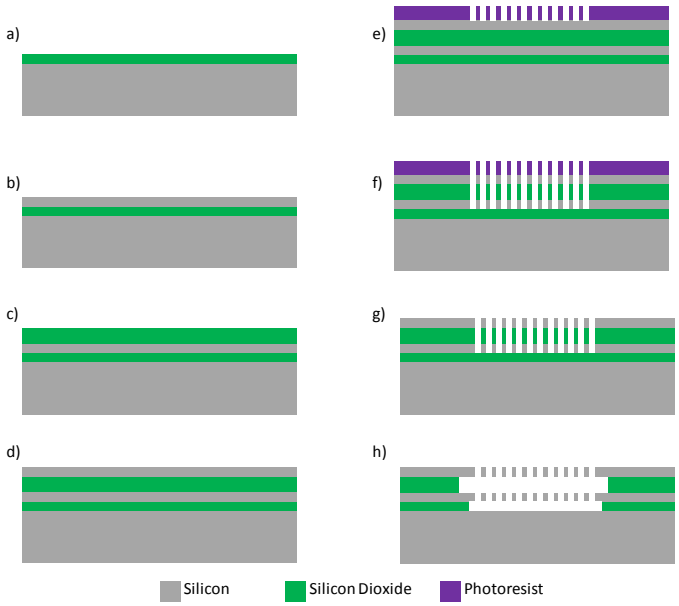

Figure 5.8: Process flow for PhC FPF. (a) 1µm PECVD SiO_2 is grown on a bare 8" Si wafer. (b) 1µm Si is then grown using LPCVD and annealing is done at 1000ºC. (c) 1.75µm SiO_2 is deposited using PECVD to define the cavity length. (d) The 1µm Si top reflector is deposited using LPCVD. (e) Coat and photolithography of PR to define air holes. (f) DRIE of $Si/SiO_2/Si$ layers to pattern the air holes in both Si layers. (g) PR strip and cleaning of wafer. (h) VHF to realize PhC FPF.

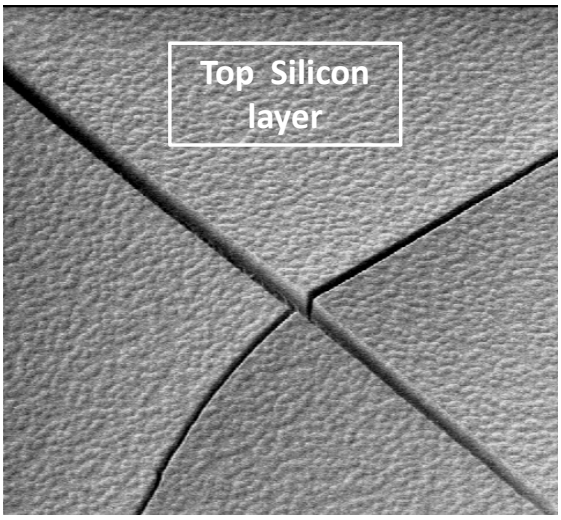

Figure 5.9: Cracking of the wafer after the 1000°C anneal step.

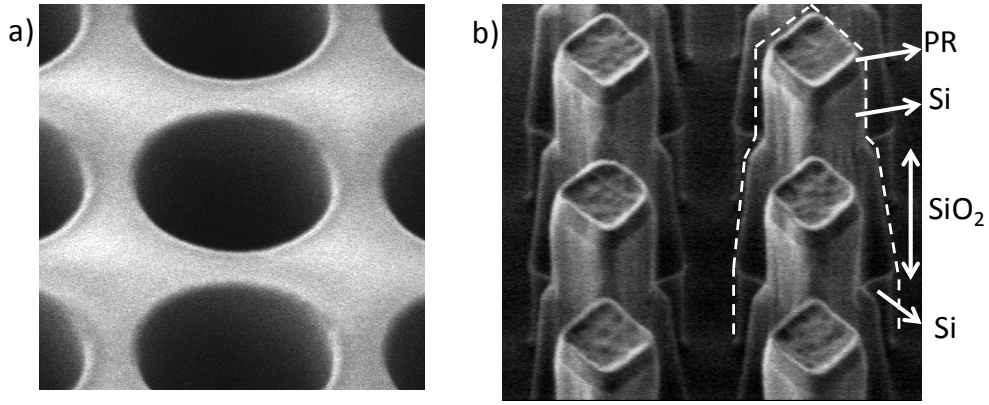

Figure 5.10: (a) SEM image of the wafer when only the top Si is etched and (b) sloping sidewall profile after the Si/SiO_2/Si stack is etched.

In order to avoid CMP of the SiO_2 which defines the Fabry-Perot cavity so as to obtain maximum accuracy of its thickness, we used a single etch step to define the FPF as shown in Figure 5.8(f). In Figure 5.10(a), when only the top Si layer is etched, the etched holes are still well defined. However, after etching the Si/SiO_2/Si stack as shown in (b), it was observed that the top Si experiences over etching which causes the size of the air hole to enlarge. In the etching of SiO_2, it is also observed that the sidewall profile is sloping. This causes the air hole pattern on the bottom Si mirror to be much smaller than designed. With a different air hole size between the top and bottom Si layers, based on the

analysis in previous chapter, it is expected that they will display vastly different reflection spectrum. Without working at a common wavelength, the efficiency of the Fabry-Perot cavity to filter unwanted wavelengths will be greatly reduced. Due to the inability to control the etching profile of the $Si/SiO_2/Si$ stack, the fabrication process has to be revised. In order to reduce the thermal budget of the fabrication flow, we have to replace the high temperature steps with lower temperature ones. Firstly, the LPCVD Si which forms the Si reflectors is grown in a furnace at 540^{o}C. However, the Si is amorphous and requires anneal at 1000^{o}C to form polycrystalline Si. The high temperature anneal induces very high thermal stress and causes the wafers to crack as shown above. In order to avoid the high temperature anneal, epitaxial Si is used instead. Although the epitaxial Si is deposited at 610^{o}C, the Si deposited is polycrystalline. This means that there is no need for the wafers to undergo the 1000^{o}C anneal step. The next issue faced is the inability to control the sidewall profile of the $Si/SiO_2/Si$ stack after etching. The proposed method to overcome this is the use of a bottom-up approach in the fabrication. Instead of depositing the $Si/SiO_2/Si$ stack before etching the air holes, the reflectors in the FPF is etched layer by layer. The detailed fabrication process is shown in Figure 5.11.

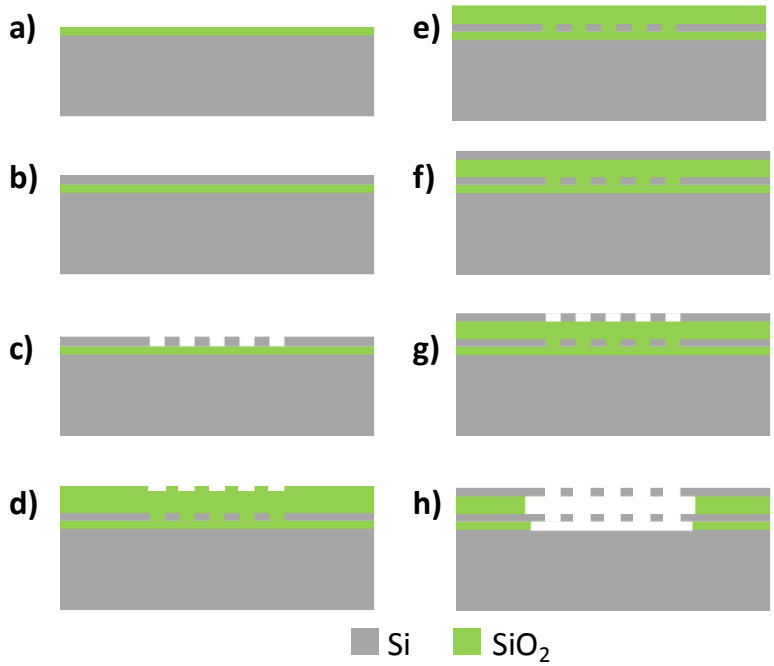

Figure 5.11: Revised process flow for PhC FPF. (a) 1µm PECVD SiO_2 is grown on a bare 8" Si wafer. (b) 1µm epitaxial Si is then deposited. (c) Photolithography of PR and DRIE of Si to define air holes. (d) 2µm SiO_2 is deposited using PECVD to define the cavity length. (e) CMP of the SiO_2 layer to remove topology of the top wafer. (f) Deposition of epitaxial Si for top reflector. (g) DRIE of Si to pattern the air holes in top Si layers. (h) VHF to realize PhC FPF.

The revised fabrication process flow of the FPF starts with a 1 µm PECVD SiO_2 on a bare Si wafer as shown in Figure 5.11(a). The device layer of 1 µm thick polycrystalline Si of the bottom PhC mirror is then deposited using epitaxy (Figure 5.11(b)). Photolithography followed by DRIE of poly crystalline Si layer to form the air holes is then performed to define the bottom PhC mirror (Figure 5.11(c)). A 2 µm PECVD SiO2 is deposited (Figure 5.11(d)) before CMP of 0.2 µm of SiO_2 is done to remove topology issues and also to define the cavity length of the FPF (Figure 5.11(e)). The 1 µm Si device layer of the top PhC mirror is then deposited using epitaxy (Figure 5.11(f)) and the air holes are defined through photolithography and DRIE (Figure 5.11(g)). Finally, the FPF is released by using VHF (Figure 5.11(g)).

The CMP step in Figure 5.11(e) is needed due to the topology issue. When SiO_2 is deposited after the etching of the bottom Si reflector (Figure 5.11(d)), it was found that the top surface of the SiO_2 is not flat as shown in Figure 5.12. If this topology issues on the top surface of the SiO_2 is not removed, such unevenness will be transferred to the top Si layer when it is deposited. In order to prevent this, we deposit an additional 0.20 μm of SiO_2 and CMP is used to thin it back to the desired 1.80 μm. The compromise that has to be taken is the incapability to control exactly the thickness of SiO_2 left to define the Fabry-Perot cavity. This is because the CMP of SiO_2 is time-based and variation cannot be avoided. The variation can, however, be minimized by using multiple test wafers to determine the CMP rate before proceeding with the FPF wafers.

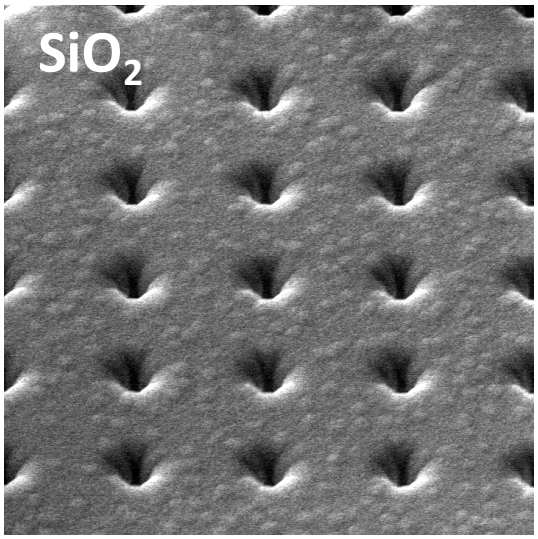

Figure 5.12: SEM image of the wafer after the SiO_2 is deposited to define the cavity length. Topology issue is apparent at the top surface and this is removed by performing CMP of SiO_2.

The fabricated device is shown in Figure 5.13(a). In order to reveal the bottom PhC reflector, the fabricated device is cleaved along dotted line. It is also noted that the air holes, although etched after different photolithography steps, the misalignment between the top Si reflector and bottom Si reflector is minimal.

In addition, the dimensions of the air holes are also well-controlled. The cross-sectional view of the FPF before release is shown in Figure 5.13(b). The bottom SiO_2 layer shown is the BOX while the top SiO_2 defines the Fabry-Perot cavity and it is measured to be 1.70 μm. This will have an impact on the FPF performance which will be discussed later.

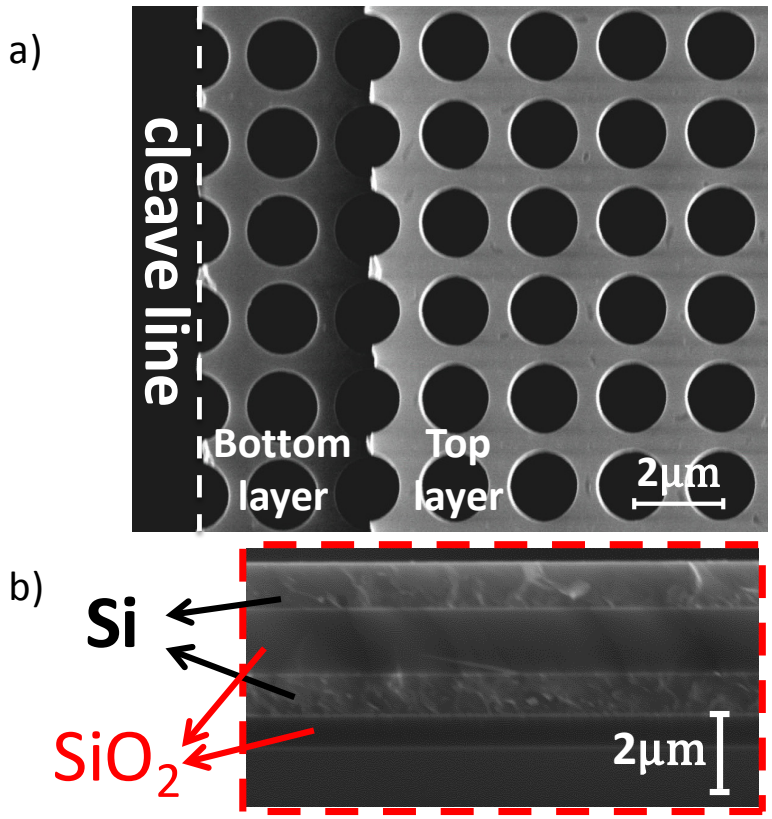

Figure 5.13: SEM image of the (a) top and (b) cross-sectional view of the fabricated FPF before VHF release.

5.5 Characterization of Photonic Crystal based Fabry-Perot filter using epitaxial Si

As mentioned above, the PhC mirrors are now fabricated using epitaxial Si instead of the previously utilized LPCVD Si which requires high temperature annealing. Hence there is a need to characterize the epitaxial Si PhC mirror to

ensure that the reflection peak is still around 3.55μm. The PhC reflector is made suspended in order to make it compatible with subsequent fabrication of the FPF as shown in Figure 5.14(a). Fabrication of the PhC reflector starts by growing a 1 μm PECVD SiO_2 on a bare 8" Si wafer. The device layer of 1 μm thick polycrystalline Si is then deposited by using epitaxy. The air holes are patterned using deep-UV lithography and etched using DRIE. The PhC reflector is finally released using VHF. The SEM of the fabricated PhC reflector is shown in (b).

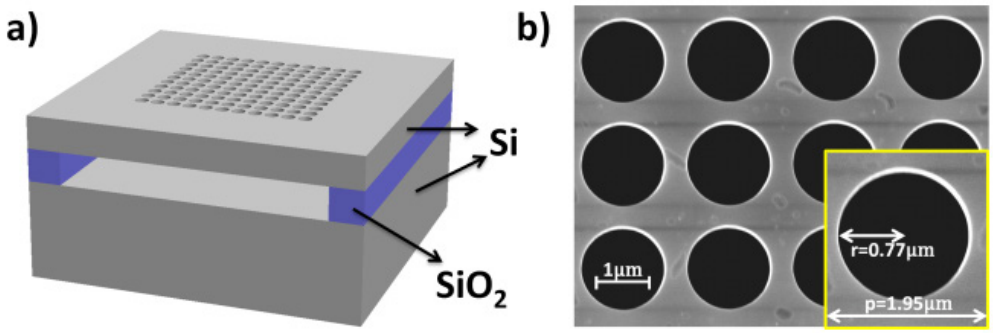

Figure 5.14: (a) Schematic of PhC reflector and (b) SEM of fabricated chip.

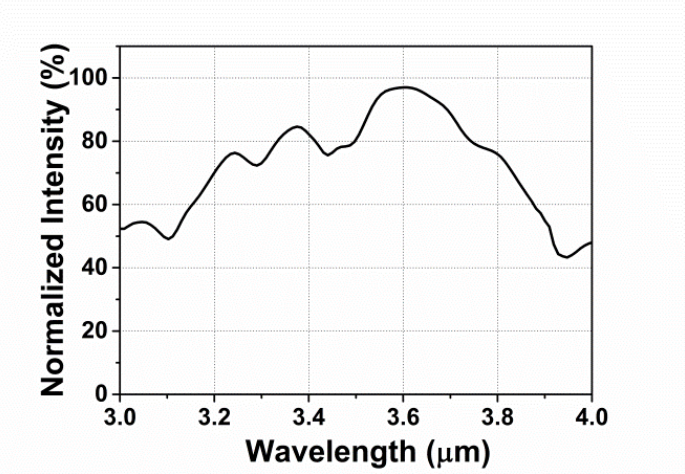

Figure 5.15: Reflection measurement of the fabricated PhC reflector.

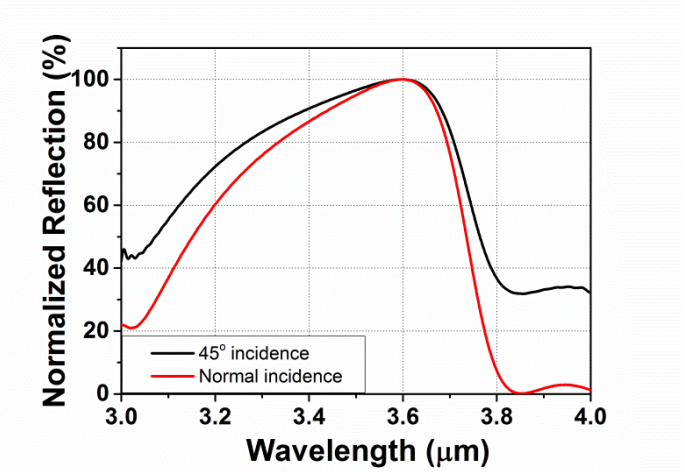

Figure 5.16: 3-D FDTD simulation of the PhC reflector at 45° incidence and normal incidence.

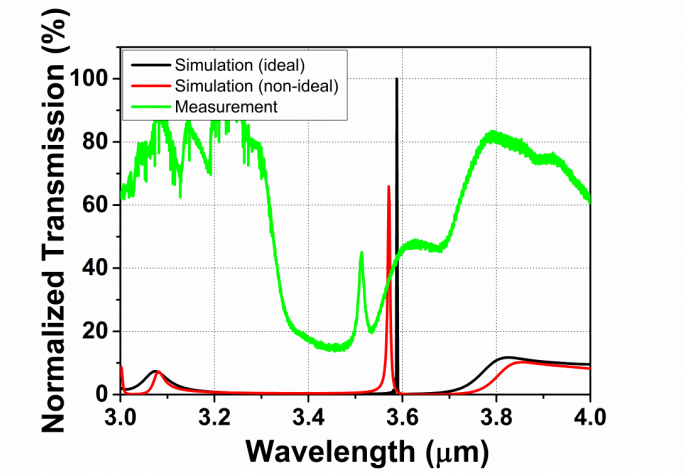

Figure 5.17: Simulation of ideal and non-ideal case of the FPF and measurement of the fabricated FPF.

Measurement of the PhC mirror is also done using the FTIR Microscope from 2 μm to 8 μm. Due to the experimental setup, the angle of incidence for the reflection measurement is limited to 45°. The reflection measurement of the PhC mirror is shown in Figure 5.15. A high reflection of 96.4% is measured at 3.60 μm with a bandwidth of 160 nm for wavelengths that have reflection of more than 90%. The dips in reflection observed at 3.29 μm and 3.43 μm was looked into in our previous section where we attributed them to the 45° angle of incidence. It is noted that the peak reflection wavelength of 3.60 μm of the PhC

reflector using epitaxial Si is slightly higher than the PhC reflector using LPCVD Si. This is due to a slight increase in the refractive index of the epitaxial Si than LPCVD Si.

As the subsequent measurement of the FPF is based on transmission which has an angle of incidence fixed to normal incidence, the dependence of the performance of the PhC mirror with incident angle is investigated. Based on FDTD simulations of the PhC mirror, the wavelength of high reflection when the input IR light is incidence at 45^{o} and normal incidence remains the same at 3.60 μm as shown in Figure 5.16. Based on the measurement results from the PhC mirror where the peak reflection is at 3.60 μm, the cavity gap between the mirrors is designed to be around 1.80 μm which is half of the peak reflection wavelength. However, due to the inability to control the thickness variation induced by the CMP process of the top SiO_2 layer, it was found that the cavity length of the fabricated FPF is measured to be 1.70 μm. This has an impact on the Q factor of the eventual transmitted Fabry-Perot filtered peak.

Simulation of the FPF is done using 3-D FDTD as well where two identical 1μm thick Si slabs with air hole radius of 0.77μm are drawn with a separation defined by the cavity length. Similar to the PhC reflector simulation, the unit cell consists of both the Si slabs with a length of 1.95 μm on each side and the refractive index of Si is set to 3.464. The boundary conditions are also set to be periodic boundary condition with perfectly matched layers. In order to obtain the theoretical Q-factor of the FPF, unlike the PhC reflector, the expected high Q-factor is determined by the slope of the envelope of the decaying signal in the

simulation. This is because the energy within the cavity cannot completely decay in a time that can be simulated reasonably and the maximum Q-factor that can be simulated scales with the simulation time. The simulated Q-factor in an optimized case of a cavity length of 1.80 μm is found to be in excess of 45000 at a wavelength of 3.59 μm (ideal case) as shown in Figure 5.17. However, after taking fabrication variations into account, the simulated Q-factor drops to around 540 at 3.52 μm (non-ideal case). The enhanced Q-factor over existing works is attributed to the additional filtering effects of the PhC reflector. The first filtering effect is within the Fabry-Perot cavity where the undesired wavelengths are attenuated due to destructive interference. The second filtering effect is due to the intrinsic wavelength selective reflectivity of PhC reflector which has a bandwidth of around 160 nm which has more than 90% reflection. In contrast, multilayer Bragg reflector has bandwidth of more than 3 μm in the MIR wavelengths for reflection more than 90% [106, 170, 171]. This makes the PhC reflector able to filter unwanted wavelengths more efficiently than the multilayer Bragg reflector, hence resulting in higher Q-factor Measurement of the FPF is also done by Agilent Cary 620 FTIR Microscope from 2 μm to 8 μm. Similarly, the size of the FPF is designed to be 200 μm by 200 μm. In the case of transmission measurement, the incidence angle is normal to the sample. The resolution of the FTIR microscope is set to 0.09 cm^{-1}. As the wavelengths are around 3.50μm, the wavelength step at this resolution is 0.11 nm. This corresponds to a measureable Q-factor of 32000. The measurement result is also shown in Figure 5.17. Measurement of the fabricated device reveals a Q-factor of around 300 at a wavelength of 3.51 μm. The lower transmission intensity for

wavelength range below 3.35 μm and above 3.55 μm in the simulations can be attributed to the simulation methods adopted for the high Q-factor simulations as the transmission intensity of wavelengths where there are no resonances are suppressed. Hence the measurement has higher transmission for wavelength range below 3.35 μm and above 3.55 μm. Figure 5.18 below shows the simulated spectra when different simulation times are used. As can be seen, with an increased simulation time from 1ps to 10ps, the reflection intensity for wavelength range below 3.35 μm and above 3.55 μm are being suppressed, hence the large difference between the reflection intensities observed for the measurement and the simulation. A longer simulation time is needed to accurately calculate the maximum Q-factor and the simulation with a simulation time of 10 ps is used. Any simulation time longer than 10 ps is found to be insignificant to the Q-factor simulated.

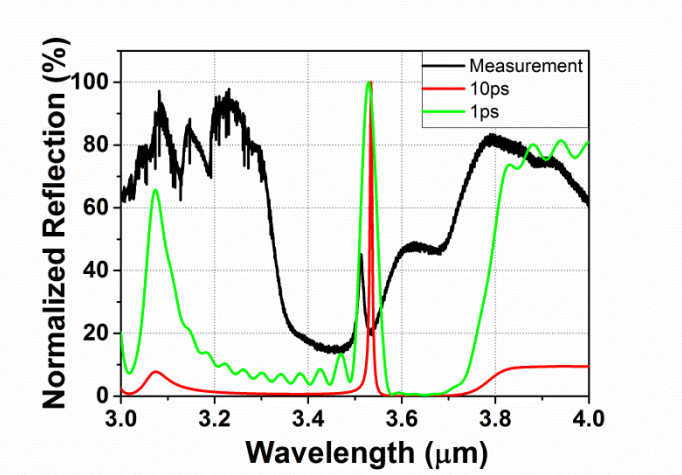

Figure 5.18: Comparison of the measurement results with 3-D FDTD simulation of the FPE with various simulation times.

While the measured Q-factor is lower than the simulated Q-factor, it is still around an order of magnitude higher than existing works where the Q-factor is

typically few tens. The shift in the transmission wavelength and the drop in Q-factor can be attributed to the variation in the cavity length. When the cavity length is not at the optimal distance, the MIR light is unable to be confined within the cavity due to higher transmission. This reduces the efficiency of the constructive interference of the desired wavelength, which causes a drop in output intensity as well as broadening of the transmission peak. Both these factors result in a much lower Q-factor. In addition, the presence of the Si substrate in the FPF causes a drop in the transmitted intensity. Based on measurements of bare Si, the transmitted intensity is reduced to around 60% for wavelengths around 3.60 μm. The effect of the Si substrate will be removed in future iterations by performing a DRIE etch of the Si substrate. In order to alleviate the fabrication variations introduced by the CMP process on the cavity length, MEMS technology can be incorporated in the design. With MEMS technology, it will enable actuation of the PhC reflector and hence achieve tunability of the cavity length. This not only reduces the impact of cavity length variation in fabrication process, it also offers the possibility of realizing a tunable Fabry-Perot interferometer.

5.6 Conclusion

In conclusion, we have demonstrated the development of a PhC FPF aiming to work in the mid-infrared wavelengths. The highly reflective PhC mirrors are realized by fabricating free-standing polycrystalline Si membranes with etched circular air holes. We have proposed a monolithic approach in the fabrication in order to achieve simplicity and low-risk. We observed a peak reflection of

96.4% at 3.60 μm through measurement. We have also fabricated and characterized a PhC FPF based on the knowledge obtained from the PhC mirror. With a high reflection at 3.60 μm, the cavity length of the cavity is designed to be around 1.80 μm. From simulations, the Q-factor in an ideal scenario where the optimized cavity length is 1.80 μm is found to be in excess of 45000. After taking fabrication variations into account, the simulated Q-factor is around 540. Measurement of the fabricated device reveals a Q-factor of around 300 which is around an order of magnitude higher than existing works.

CHAPTER 6: Future work

6.1 Conclusions on current work

In the previous part of the thesis, numerous photonic crystal based designs have been described. Starting from an in-plane design, the photonic crystal based waveguide was introduced. By embedding the PhC waveguide with a MZI, the device demonstrates slow light effect, which is a key method to increase light-matter interaction for improved sensor performance. In order to enhance the performance of the photonic device, shape of the air holes on selected rows is changed from circular to elliptical. In addition, lattice shifting is also performed to achieve lower dispersion and hence higher DBP. In conclusion, a group index of 166 and DBP of 0.1812 is achieved and this poses well for future optimization on such PhC waveguide design to demonstrate better slow light effect.

We also move on to using in-plane PhC designs which utilizes AlN as the main optical material. This will be the preliminary work in order to realize more complicated photonic design in the future. We start the investigation with a simple AlN bus waveguide that is coupled to a 1-D PhC design which has a cavity defect. We have designed the coupling wavelength to be 1550 nm. However, due to fabrication variations, experimental results show that the coupled wavelength is around 1575 nm instead. Nonetheless, the dip in the optical signal measured from the bus waveguide still reveals a high Q-factor of 2000. This signifies that AlN is a viable option to be used as an optical layer despite its relatively low refractive index. The propagation loss for AlN

waveguide is also within tolerance. This bodes well for further optical design involving AlN such as slow light devices etc. This is especially important as the material offers flexibility such as non-linearity and piezoelectric effect, which are absence or difficult to obtain in Si based photonic designs.

The thesis continues to describe works that are done to realize PhC based reflector which can be used in an out-of-plane manner. PhC reflector has been used in many sensing applications. By using polycrystalline Si, we introduced a low cost fabrication method. Two shapes of the air holes are investigated and the wavelength at which the reflectors work in is chosen to be in the MIR as there are numerous industrial applications that utilize such wavelengths. While the reflector with circle air holes performs to expectation by showing high reflectivity at around 3.60μm, PhC reflector with square air holes are also designed to show high reflectivity in MIR region as well. Square air holes however, when compared to circular air holes, have a lower filling factor, which makes the membrane less brittle and offers more flexibility in design and fabrication especially in MEMS application where such membranes are released and free-standing. Temperature effect on the performance of the PhC reflector is also examined by subjecting the PhC reflector to a high temperature of 450^{o}C. Due to thermo-optic effect, the peak reflection of the PhC reflector at 25^{o}C increase from 3.58 μm to 3.65 μm when the temperature increases to 450^{o}C. Based on this results, the thermo-optic effect induces a shift of 0.174 nm per degrees Celsius temperature change and the thermo-optic coefficient can be calculated to be $+1.70\times10^{-4}$ K^{-1}.

In order to compensate such thermo-optic effect, a simple methodology proposed is to alter the air hole dimension when designing the device. By doing simple calculation based on the thermo-optic coefficient, the redshift induced by the increase in temperature can be totally removed by increasing the dimension of the PhC air holes. In this thesis, it is demonstrated that the PhC reflector is able to still display a maximum reflection at 3.55 μm at 450^{o}C by altering the radius of the circle air hole from 760 nm to 780 nm.

A more attractive method to reduce thermo-optic effect is to use AlN as the photonic material as it has a much smaller thermo-optic coefficient compared to Si. Based on our design, AlN PhC reflector is still able to display high reflection of more than 90% was observed from 3.08 μm to 3.78 μm. When the temperature is increases to 450^{o}C, it is observed that the redshift in the peak reflection of the PhC is estimated to be 14.1 nm. The thermo-optic coefficient is estimated to be $+2.22\times10^{-5}$ K^{-1}, which is an order of magnitude lower than Si. Even at elevated temperatures, the low thermo-optic coefficient of AlN ensures that the peak reflection wavelength does not change drastically.

We extended our work to include the design, fabrication and characterization of a FPF which is fabricated using a CMOS-compatible monolithic fabrication process. FPF is an important device that is widely used in sensing applications such as gas sensing. The fabrication process was one of the major issues that were faced due to the multiple layers of Si and SiO_2 involved. An optimized process flow was finally realized and implemented by using the bottom-up approach. Although the Fabry Perot cavity length was not well-controlled due

to CMP, the measured filtered peak still has a Q-factor of around 300. This is around an order to magnitude higher than existing works. In future works as described below, the inclusion of MEMS technologies to achieve tunability and to alleviate fabrication variations will allow the realization of high performing PhC FPF for high-resolution applications such as gas sensing and hyperspectral imaging.

6.2 Recommendations for future work

6.2.1 In-plane photonic designs using AlN

While preliminary work on AlN based in-plane photonic designs has been presented, the non-linearity aspect and thermo-optic effect of AlN has yet to been explored and exploited. In order to do so, external electric field has to be introduced to the device. By using a voltage bias that creates a concentrated electric field going through the AlN photonic, it is possible to realize a tunable photonic design. In order to add voltage bias to the device, the process flow of AlN photonic design has to be altered slightly as shown in Figure 6.1.

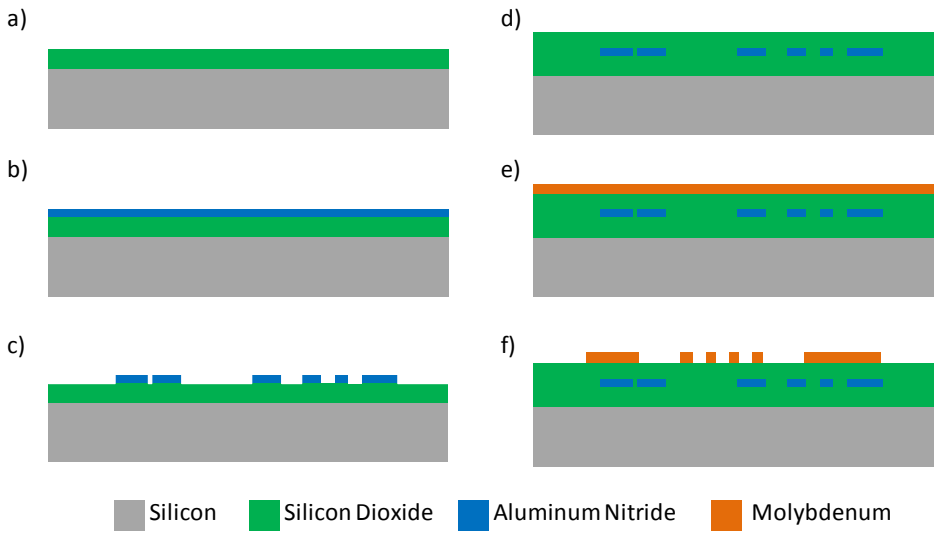

Figure 6.1: Revise fabrication process flow for tunable AlN photonics.

The process flow begins with the deposition of 2 μm SiO_2 on a bare 8" Si wafer (a). AlN is then deposited using PVD, followed by a thin SiO_2 hardmask (b). Photolithography and etching is then done to pattern the SiO_2 and subsequently the AlN photonic layer (c). A thick layer of SiO_2 is then deposited to cover the AlN layer and CMP done to remove any topology issues (d). As mentioned before, Mo is a good candidate to be used as the metal electrode due to its CMOS compatibility and its high melting point. Hence, Mo is deposited on SiO_2 (e) and Mo is patterned and etched (f). In this configuration, the Mo electrodes can be designed to create a high electric field to go through the AlN photonic pattern. With a high enough electric field, Pockel's effect can be excited and the refractive index of the AlN photonic material can be tuned. Based on the direction of the electric field, the refractive index of AlN can be increased or decreased, thus causing the resonance wavelength to redshift or blueshift respectively.

It is important to note that given that only a thin layer of Mo is deposited as the electrode, topology issues has to be removed via CMP. Without doing so, the unevenness of the top surface will be transferred to the Mo metal lines as shown in Figure 6.2. Due to the height difference, the metal line will be thinner at the interception point as shown by the circle in Figure 6.2. There is hence a possibility that the metal line will break and an open circuit will be formed. While thicker Mo layer can be deposited to alleviate this issue, it creates new problems such as thicker PR needed for Mo etching and higher voltages needed to achieve similar performance due to larger cross-sectional area.

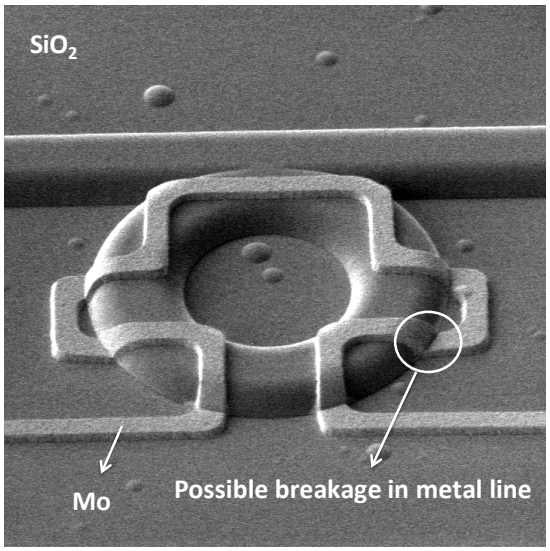

Figure 6.2: SEM image of AlN photonic without CMP to remove the topology issue after SiO_2 deposition.

6.2.2 Design and fabrication of tunable FPF

In previous work, we have fabricated FPF that displays high Q-factor. However, due to the CMP process of the SiO_2 in between the two Si layers, the Fabry Perot cavity gap is not well-controlled. In order to overcome such variations, MEMS technology can be incorporated to implement actuators into the design. This enables electrostatic actuation of one of the PhC reflector and hence achieves tunability of the cavity length. This not only reduces the impact of cavity length variation in fabrication process, it also offers the possibility of realizing a tunable Fabry-Perot interferometer. The design of the actuator plays a critical role as the Si layer has to be made less stiff in order to introduce displacement. This will create issues such as buckling of the Si reflector when actuated which will reduce the performance of the tunable FPF. While buckling can be reduced by having softer springs, it will introduce problems such as both Si membranes sticking together after release. Hence, an optimization process has to be undertaken.

A simple spring design is to have eight fixed-fixed beams connected to the released Si membrane which include the PhC reflector, as shown in Figure 6.3(a). We maintained a PhC reflector area of 150 µm by 150 µm and the eight fixed-fixed beams of 40 µm by 90 µm. The thickness of the Si is still 1 µm. However, when actuated as shown in (b), it was realized that buckling effect of the Si membrane is severe, especially in the middle. The height difference between the edge and the middle of the PhC reflector is around 60 nm and this causes the Fabry Perot length to vary. In order to maintain good performance of the FPF, the Si membrane should be made as flat as possible when actuated.

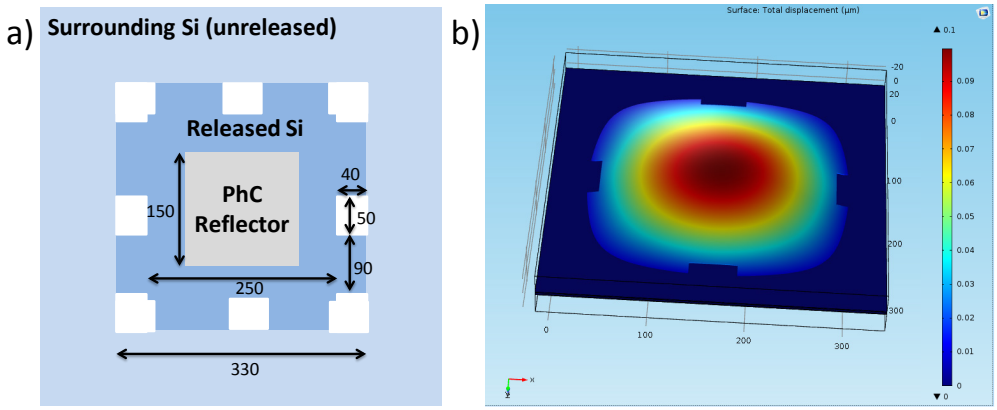

Figure 6.3: (a) Spring design of the Si membrane and (b) Simulation of the Si membrane when undergoing electrostatic actuation. All dimensions indicated are in µm.

In order to reduce buckling effect of the Si membrane when actuated, an enhanced version of the spring design can be implemented. One of the better designs is the meander shaped spring. Likewise to previous design, the PhC reflector area is 150 µm by 150 µm and the thickness of the Si is still 1 µm. The parameters are shown in Figure 6.4(a). When the Si membrane is actuated as shown in (b), the deformation in the released Si membrane is very flat in the middle. The height difference between the edge of the PhC reflector and the

middle is also minimized to 1.7 nm. This amount of height variation is negligible.

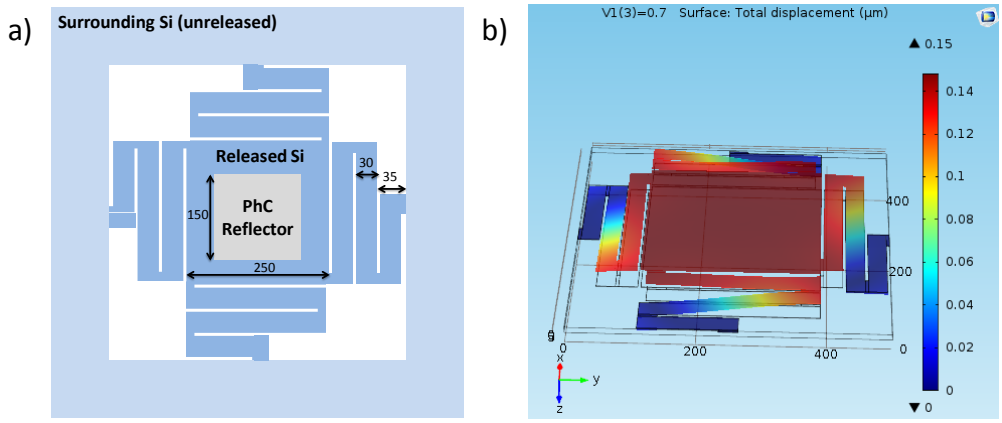

Figure 6.4: (a) Enhanced spring design of the Si membrane and (b) Simulation of the Si membrane when undergoing electrostatic actuation. All dimensions indicated are in µm.

The fabrication process flow of tunable FPF has to be changed as the two Si layers have to be doped and metal vias created for contact pads. The proposed fabrication flow is shown in Figure 6.5. The proposed process flow is largely similar to that of the FPF described earlier. The main additional steps are the inclusion of selective area doping so that the Si membranes are conductive and can be actuated through electrostatic attraction. 1 µm of SiO_2 is first grown opn the 8" bare wafer and 1 µm of epitaxial Si is then deposited (Figure 6.5(a)). The PhC reflector design is then etched on the bottom layer (Figure 6.5(b)) and the area of the released Si is then doped through ion implantation (Figure 6.5(c)). Care has to be taken to ensure that the area of the PhC reflector is not doped as it will cause the refractive index of the Si to change, hence affecting the performance of the reflector. The frame of the bottom Si reflector is then defined (Figure 6.5(d)) and the wafer is then covered with 2 µm of SiO_2 (Figure 6.5(e)). CMP is then done to remove 0.2 µm of SiO_2 to reduce topology (Figure 6.5(f)).

The top 1 µm epitaxial Si is then grown (Figure 6.5(g)) and the PhC reflector defined (Figure 6.5(h)). The top Si is then doped (Figure 6.5(i)) and the frame and springs designs are then defined through DRIE (Figure 6.5(j)). The wafer is then covered with SiO_2 (Figure 6.5(k)) before vias are etched into the SiO_2 for metal contacts. Aluminium is then deposited and etched to form the metal pads (Figure 6.5(l)) and the device undergoes VHF release to realize the tunable FPF (Figure 6.5(m)).

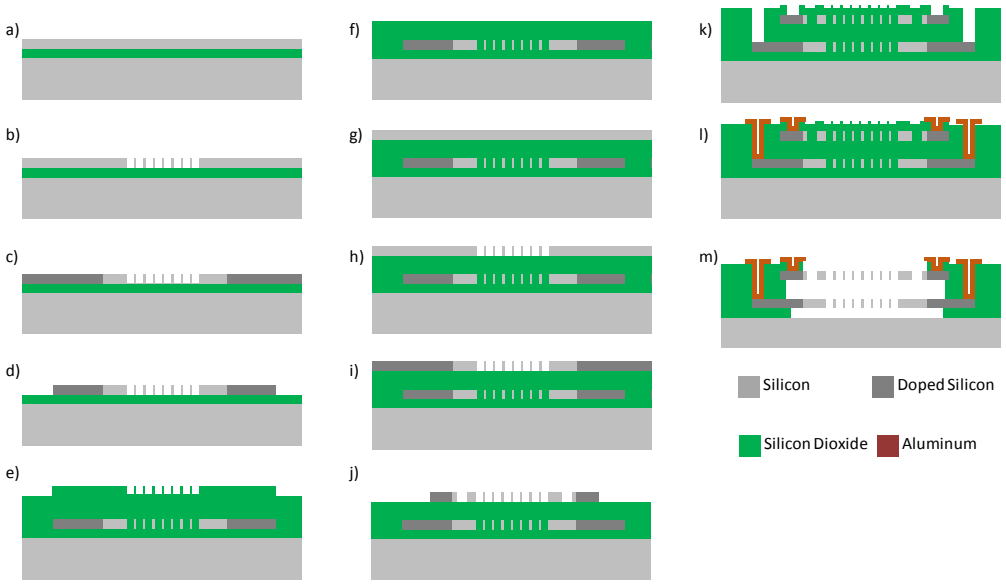

Figure 6.5: Fabrication process flow for tunable FPF.

6.2.3 Terahertz FPF

THz region of the EM spectrum has a great potential in the realization of wide range of impactful applications, such as non-invasive medical inspection, next-generation wireless communication networks, non-destructive fault analysis, security surveillance, etc. [172-175]. In order to enhance the sensitivity of the devices to surrounding environment, devices with high Q-factor output are desirable. While the use of metamaterial is common in the THz range, the Q-factor obtained is usually lesser than 300 [176-180]. In an

attempt to increase the Q-factor, Chen et al. used a 1-D PhC based Fabry Perot filter and demonstrated an output with Q-factor over 11000 [181]. This is done through placing two mirrors which are made of three 472 µm Si wafers and two 200 µm of air layers. While this approach offers extremely high Q-factor, the size of the whole device is not suitable practical usage. In order to obtain even higher Q-factor and also to reduce the footprint of the device, we propose to utilize a THz 2-D PhC based FPF. The designed frequency of the FPF is around 0.30 THz and hence the PhC reflector should display high reflection at around 0.30 THz as well. In order to do so, the PhC reflector is designed to have a pitch of 530 µm, the radius of the circle air hole is 213 µm and the thickness is 300 µm. The simulation of the THz PhC reflector is shown Figure 6.6. The reflection peak and transmission dip are both around 0.30THz.

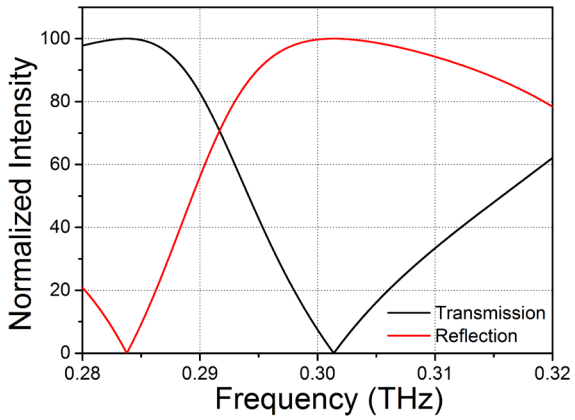

Figure 6.6: Simulation of the THz PhC reflector.

In order to realize the THz FPF, the PhC reflector is fabricated and assembled with a spacer in between to define the cavity gap. The process flow to realize the THz FPF is shown in Figure 6.7. The process flow starts with an 8" Si wafer which has a thickness of 725 µm (Figure 6.7(a)). A 2 µm PECVD SiO_2 is then

deposited as hard mask (Figure 6.7(b)), followed by photolithography and etching of the SiO_2 (Figure 6.7(c) and (d)). The wafer is then placed for 400 µm Si etch (Figure 6.7(e)) before the PR and hard mask are removed (Figure 6.7(f)). The PhC reflector is then realized by sticking the wafer to a Si holder before back-grinding the wafer to 300 µm thin (Figure 6.7(g)). The Si holder is then removed by heating the wafer to 160°C. Finally, the PhC reflector is assembled into THz FPF by using Si spacer which defines the cavity gap.

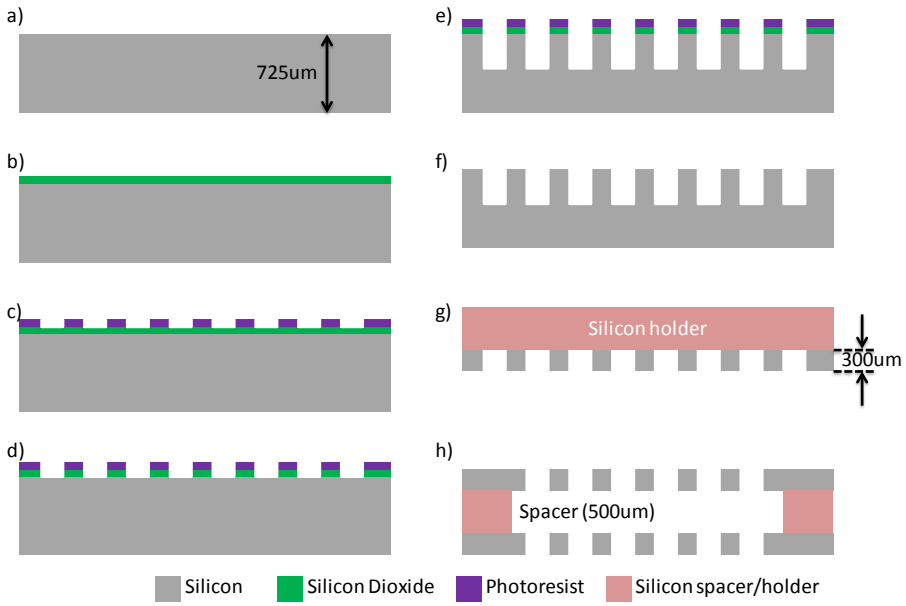

Figure 6.7: Fabrication process flow of THz FPF.

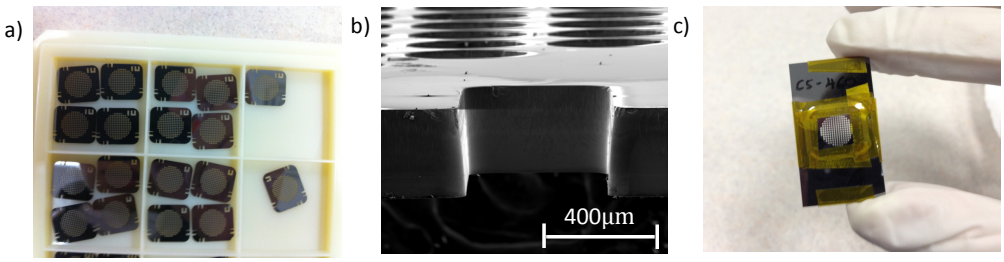

Figure 6.8: (a) Photograph and (b) SEM image of the fabricated PhC reflector. (c) Image of the FPF which is assembled with two PhC reflectors at the front and back.

The fabricated PhC reflector is shown in Figure 6.8(a). From the SEM image shown in (b), it can be seen that the Si etching producing a sloping sidewall

which is calculated to be 86.9^{o}. The FPF is assembled with two PhC reflectors with a Si spacer in between as shown in (c). The thickness of the Si spacer is defined by performing a back-grind on a bare Si wafer. The simulation of the THz FPF is shown in Figure 6.9. As seen, the filter peak has a high Q-factor of around 30000 which is about three times higher than the highest Q-factor reported in existing works.

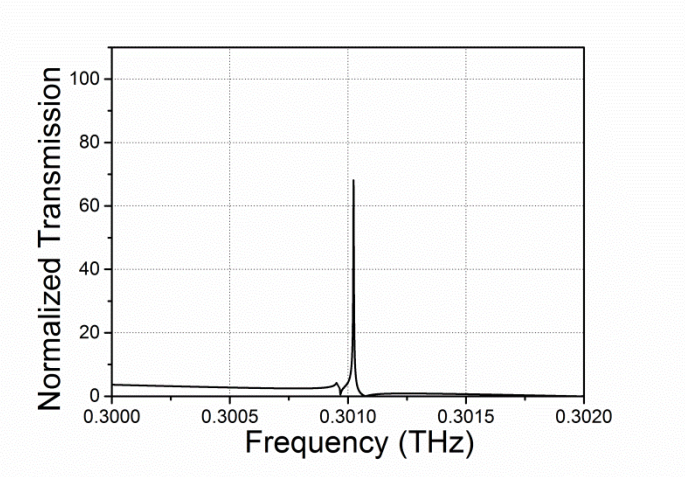

Figure 6.9: Simulation of the THz FPF.

In order to characterize the THz FPF at such a high Q-factor, the measurement setup needs to have a resolution of at least 10 MHz. Such a system is not readily available and collaborations with external parties might have to be explored in order to improve the situation.

BIBLIOGRAPHY

[1] D. K. Armani, T. J. Kippenberg, S. M. Spillane, and K. J. Vahala, "Ultra-high-Q toroid microcavity on a chip," *Nature,* vol. 421, pp. 925-928, 2003.

[2] M. L. Gorodetsky, A. A. Savchenkov, and V. S. Ilchenko, "Ultimate Q of optical microsphere resonators," *Optics Letters,* vol. 21, pp. 453-455, 1996.

[3] D. W. Vernooy, V. S. Ilchenko, H. Mabuchi, E. W. Streed, and H. J. Kimble, "High-Q measurements of fused-silica microspheres in the near infrared," *Optics Letters,* vol. 23, pp. 247-249, 1998.

[4] D. W. Vernooy, A. Furusawa, N. P. Georgiades, V. S. Ilchenko, and H. J. Kimble, "Cavity QED with high-Q whispering gallery modes," *Physical Review A,* vol. 57, pp. R2293-R2296, 1998.

[5] B. Gayral, J. M. Gérard, A. Lemaître, C. Dupuis, L. Manin, and J. L. Pelouard, "High-Q wet-etched GaAs microdisks containing InAs quantum boxes," *Applied Physics Letters,* vol. 75, pp. 1908-1910, 1999.

[6] K. Djordjev, S.-J. Choi, S.-J. Choi, and P. D. Dapkus, "Microdisk tunable resonant filters and switches," *IEEE Photonics Technology Letters,* vol. 14, pp. 828-830, 2002.

[7] A. L. Washburn, M. S. Luchansky, A. L. Bowman, and R. C. Bailey, "Quantitative, label-free detection of five protein biomarkers using multiplexed arrays of silicon photonic microring resonators," *Analytical Chemistry,* vol. 82, pp. 69-72, 2009.

[8] S. Lacey, I. M. White, Y. Sun, S. I. Shopova, J. M. Cupps, P. Zhang, and X. Fan, "Versatile opto-fluidic ring resonator lasers with ultra-low threshold," *Optics Express,* vol. 15, pp. 15523-15530, 2007.

[9] A. Melloni, R. Costa, P. Monguzzi, and M. Martinelli, "Ring-resonator filters in silicon oxynitride technology for dense wavelength-division multiplexing systems," *Optics Letters,* vol. 28, pp. 1567-1569, 2003.

[10] M. Soltani, S. Yegnanarayanan, and A. Adibi, "Ultra-high Q planar silicon microdisk resonators for chip-scale silicon photonics," *Optics Express,* vol. 15, pp. 4694-4704, 2007.

[11] C. Baker, S. Stapfner, D. Parrain, S. Ducci, G. Leo, E. M. Weig, and I. Favero, "Optical instability and self-pulsing in silicon nitride whispering gallery resonators," *Optics Express,* vol. 20, pp. 29076-29089, 2012.

[12] S. Ghosh and G. Piazza, "Photonic microdisk resonators in aluminum nitride," *Journal of Applied Physics,* vol. 113, p. 016101, 2013.

[13] M. Bürger, M. Ruth, S. Declair, J. Förstner, C. Meier, and D. J. As, "Whispering gallery modes in zinc-blende AlN microdisks containing non-polar GaN quantum dots," *Applied Physics Letters,* vol. 102, p. 081105, 2013.

[14] K. Volyanskiy, P. Salzenstein, H. Tavernier, M. Pogurmirskiy, Y. K. Chembo, and L. Larger, "Compact optoelectronic microwave oscillators using ultra-high Q whispering gallery mode disk-resonators and phase modulation," *Optics Express,* vol. 18, pp. 22358-22363, 2010.

[15] S. Hadzialic, S. Kim, A. F. Sarioglu, Sudb, x00F, A. S., and O. Solgaard, "Displacement Sensing With a Mechanically Tunable Photonic Crystal," *IEEE Photonics Technology Letters,* vol. 22, pp. 1196-1198, 2010.

[16] N. Descharmes, U. P. Dharanipathy, Z. Diao, M. Tonin, and R. Houdre, "Single particle detection, manipulation and analysis with resonant optical trapping in photonic crystals," *Lab on a Chip,* vol. 13, pp. 3268-3274, 2013.

[17] Y. Yao, M. A. Kats, R. Shankar, Y. Song, J. Kong, M. Loncar, and F. Capasso, "Wide Wavelength Tuning of Optical Antennas on Graphene with Nanosecond Response Time," *Nano Letters,* vol. 14, pp. 214-219, 2014.

[18] G. Gilardi, H. Yilmaz, M. Sharif Murib, R. Asquini, A. d'Alessandro, A. Serpengüzel, and R. Beccherelli, "Tunable integrated optical filters based on sapphire microspheres and liquid crystals," *SPIE Photonics Europe. International Society for Optics and Photonics*, pp. 77191E-77191E-7, 2010.

[19] P. Wang, M. Ding, T. Lee, G. Senthil Murugan, L. Bo, Y. Semenova, Q. Wu, D. Hewak, G. Brambilla, and G. Farrell, "Packaged chalcogenide microsphere resonator with high Q-factor," *Applied Physics Letters,* vol. 102, p. 131110, 2013.

[20] M. Barth, J. Stingl, N. Nüsse, B. Löchel, and O. Benson, "Controlled coupling of nanoparticles to photonic crystal cavities," 2009, pp. 72230Y-72230Y-8.

[21] M. Li, X. Wu, L. Liu, X. Fan, and L. Xu, "Self-Referencing Optofluidic Ring Resonator Sensor for Highly Sensitive Biomolecular Detection," *Analytical Chemistry,* vol. 85, pp. 9328-9332, 2013.

[22] B. Robert, L. Li, M. H. F. Gordon, and U. Deepak, "MEMS-actuated wavelength drop filter based on microsphere whispering gallery modes," *Journal of Micromechanics and Microengineering,* vol. 21, p. 115020, 2011.

[23] V. R. Dantham, S. Holler, C. Barbre, D. Keng, V. Kolchenko, and S. Arnold, "Label-Free Detection of Single Protein Using a Nanoplasmonic-Photonic Hybrid Microcavity," *Nano Letters,* vol. 13, pp. 3347-3351, 2013.

[24] M. Fujiwara, T. Noda, A. Tanaka, K. Toubaru, H.-Q. Zhao, and S. Takeuchi, "Coupling of ultrathin tapered fibers with high-Q microsphere resonators at cryogenic temperatures and observation of phase-shift transition from undercoupling to overcoupling," *Optics Express,* vol. 20, pp. 19545-19553, 2012.

[25] B. E. Little, J. S. Foresi, G. Steinmeyer, E. R. Thoen, S. T. Chu, H. A. Haus, E. P. Ippen, L. C. Kimerling, and W. Greene, "Ultra-compact Si-SiO_2 microring resonator optical channel dropping filters," *IEEE Photonics Technology Letters,* vol. 10, pp. 549-551, 1998.

[26] B. E. Little, J.-P. Laine, and S. T. Chu, "Surface-roughness-induced contradirectional coupling in ring and disk resonators," *Optics Letters,* vol. 22, pp. 4-6, 1997.

[27] E. Yablonovitch, "Inhibited Spontaneous Emission in Solid-State Physics and Electronics," *Physical Review Letters,* vol. 58, pp. 2059-2062, 1987.
[28] S. John, "Strong localization of photons in certain disordered dielectric superlattices," *Physical Review Letters,* vol. 58, pp. 2486-2489, 1987.
[29] H.-T. Chien, C. Lee, H.-K. Chiu, K.-C. Hsu, C.-C. Chen, J.-a. A. Ho, and C. Chou, "The Comparison Between the Graded Photonic Crystal Coupler and Various Couplers," *Journal of Lightwave Technology,* vol. 27, pp. 2570-2574, 2009.
[30] K. J. Vahala, "Optical microcavities," *Nature,* vol. 424, pp. 839-846, 2003.
[31] P. Lalanne, C. Sauvan, and J. P. Hugonin, "Photon confinement in photonic crystal nanocavities," *Laser & Photonics Reviews,* vol. 2, pp. 514-526, 2008.
[32] S. Fan, P. Villeneuve, J. Joannopoulos, and H. Haus, "Channel drop filters in photonic crystals," *Optics Express,* vol. 3, pp. 4-11, 1998.
[33] C.-C. Chen, H.-D. Chien, and P.-G. Luan, "Photonic crystal beam splitters," *Applied optics,* vol. 43, pp. 6187-6190, 2004.
[34] L.-M. Chang, C.-H. Hou, Y.-C. Ting, C.-C. Chen, C.-L. Hsu, J.-Y. Chang, C.-C. Lee, G.-T. Chen, and J.-I. Chyi, "Laser emission from GaN photonic crystals," *Applied Physics Letters,* vol. 89, p. 071116, 2006.
[35] S. Kim, I. Park, H. Lim, and C.-S. Kee, "Highly efficient photonic crystal-based multichannel drop filters of three-port system with reflection feedback," *Optics Express,* vol. 12, pp. 5518-5525, 2004.
[36] K. Hwang and G. Song, "Design of a high-Q channel add-drop multiplexer based on the two-dimensional photonic-crystal membrane structure," *Optics Express,* vol. 13, pp. 1948-1957, 2005.
[37] D.-S. Park, O. Beom-Hoan, S.-G. Park, E.-H. Lee, and S. G. Lee, "Photonic crystal-based GE-PON triplexer using point defects," in *Integrated Optoelectronic Devices 2008*, 2008, pp. 689711-689711-9.
[38] E. Camargo, H. Chong, and R. De La Rue, "2D photonic crystal thermo-optic switch based on AlGaAs/GaAs epitaxial structure," *Optics Express,* vol. 12, pp. 588-592, 2004.
[39] Y.-D. Wu, M.-L. Huang, and T.-T. Shih, "Optical interleavers based on two-dimensional photonic crystals," *Applied optics,* vol. 46, pp. 7212-7217, 2007.
[40] M. Lipson, "Guiding, modulating, and emitting light on silicon-challenges and opportunities," *Journal of Lightwave Technology,* vol. 23, p. 4222, 2005.
[41] M. Notomi, A. Shinya, S. Mitsugi, E. Kuramochi, and H. Ryu, "Waveguides, resonators and their coupled elements in photonic crystal slabs," *Optics Express,* vol. 12, pp. 1551-1561, 2004.
[42] B. E. Little, S. T. Chu, H. A. Haus, J. Foresi, and J.-P. Laine, "Microring resonator channel dropping filters," *Journal of Lightwave Technology,* vol. 15, pp. 998-1005, 1997.
[43] F.-l. Hsiao and C. Lee, "Computational study of photonic crystals nano-ring resonator for biochemical sensing," *Sensors Journal, IEEE,* vol. 10, pp. 1185-1191, 2010.

[44] F.-L. Hsiao and C. Lee, "Nanophotonic biosensors using hexagonal nanoring resonators: computational study," *Journal of Micro/Nanolithography, MEMS, and MOEMS,* vol. 10, pp. 013001-013001-8, 2011.

[45] K. De Vos, J. Girones, T. Claes, Y. De Koninck, S. Popelka, E. Schacht, R. Baets, and P. Bienstman, "Multiplexed antibody detection with an array of silicon-on-insulator microring resonators," *IEEE Photonics Journal,* vol. 1, pp. 225-235, 2009.

[46] M. Iqbal, M. Gleeson, B. Spaugh, F. Tybor, W. G. Gunn, M. Hochberg, T. Baehr-Jones, R. C. Bailey, and L. C. Gunn, "Label-free biosensor arrays based on silicon ring resonators and high-speed optical scanning instrumentation," *IEEE Journal of Selected Topics in Quantum Electronics,* vol. 16, pp. 654-661, 2010.

[47] J. T. Kirk, G. E. Fridley, J. W. Chamberlain, E. D. Christensen, M. Hochberg, and D. M. Ratner, "Multiplexed inkjet functionalization of silicon photonic biosensors," *Lab on a Chip,* vol. 11, pp. 1372-1377, 2011.

[48] C. P. Ho, B. Li, A. J. Danner, and C. Lee, "Design and modeling of 2-D photonic crystals based hexagonal triple-nano-ring resonators as biosensors," *Microsystem technologies,* vol. 19, pp. 53-60, 2013.

[49] R. L. Rich and D. G. Myszka, "Advances in surface plasmon resonance biosensor analysis," *Current opinion in biotechnology,* vol. 11, pp. 54-61, 2000.

[50] N. Backmann, C. Zahnd, F. Huber, A. Bietsch, A. Plückthun, H.-P. Lang, H.-J. Güntherodt, M. Hegner, and C. Gerber, "A label-free immunosensor array using single-chain antibody fragments," *Proceedings of the National Academy of Sciences of the United States of America,* vol. 102, pp. 14587-14592, 2005.

[51] Y. L. Bunimovich, Y. S. Shin, W.-S. Yeo, M. Amori, G. Kwong, and J. R. Heath, "Quantitative real-time measurements of DNA hybridization with alkylated nonoxidized silicon nanowires in electrolyte solution," *Journal of the American Chemical Society,* vol. 128, pp. 16323-16331, 2006.

[52] S. Kahl and A. M. Grishin, "Enhanced Faraday rotation in all-garnet magneto-optical photonic crystal," *Applied Physics Letters,* vol. 84, pp. 1438-1440, 2004.

[53] Z. Wang and S. Fan, "Optical circulators in two-dimensional magneto-optical photonic crystals," *Optics Letters,* vol. 30, pp. 1989-1991, 2005.

[54] Q. Wang, Z. Ouyang, M. Lin, and Q. Liu, "Compact photonic crystal circulator with flat-top transmission band created by cascading magneto-optical resonance cavities," *Applied optics,* vol. 54, pp. 9741-9746, 2015.

[55] K. Busch and S. John, "Liquid-crystal photonic-band-gap materials: the tunable electromagnetic vacuum," *Physical Review Letters,* vol. 83, p. 967, 1999.

[56] S. John and K. Busch, "Photonic bandgap formation and tunability in certain self-organizing systems," *Journal of Lightwave Technology,* vol. 17, p. 1931, 1999.

[57] G. Gilardi, H. Yilmaz, M. S. Murib, R. Asquini, A. d'Alessandro, A. Serpengüzel, and R. Beccherelli, "Tunable integrated optical filters based on sapphire microspheres and liquid crystals," *SPIE Photonics Europe*, pp. 77191E-77191E-7, 2010.

[58] D. Erickson, T. Rockwood, T. Emery, A. Scherer, and D. Psaltis, "Nanofluidic tuning of photonic crystal circuits," in *Integrated Optoelectronic Devices 2007*, pp. 647513-647513-11, 2007.

[59] M. Scullion, A. Di Falco, and T. Krauss, "Slotted photonic crystal cavities with integrated microfluidics for biosensing applications," *Biosensors and Bioelectronics,* vol. 27, pp. 101-105, 2011.

[60] P. Domachuk, H. Nguyen, B. Eggleton, M. Straub, and M. Gu, "Microfluidic tunable photonic band-gap device," *Applied Physics Letters,* vol. 84, pp. 1838-1840, 2004.

[61] A. Majumdar, J. Kim, J. Vuckovic, and F. Wang, "Electrical control of silicon photonic crystal cavity by graphene," *Nano Letters,* vol. 13, pp. 515-518, 2013.

[62] M. Roussey, M.-P. Bernal, N. Courjal, D. Van Labeke, F. Baida, and R. Salut, "Electro-optic effect exaltation on lithium niobate photonic crystals due to slow photons," *Applied Physics Letters,* vol. 89, p. 241110, 2006.

[63] J. H. Wülbern, J. Hampe, A. Petrov, M. Eich, J. Luo, A. K.-Y. Jen, A. Di Falco, T. F. Krauss, and J. Bruns, "Electro-optic modulation in slotted resonant photonic crystal heterostructures," *Applied Physics Letters,* vol. 94, p. 241107, 2009.

[64] X. Chew, G. Zhou, H. Yu, F. S. Chau, J. Deng, Y. C. Loke, and X. Tang, "An in-plane nano-mechanics approach to achieve reversible resonance control of photonic crystal nanocavities," *Optics Express,* vol. 18, pp. 22232-22244, 2010.

[65] O. Arcizet, P.-F. Cohadon, T. Briant, M. Pinard, A. Heidmann, J.-M. Mackowski, C. Michel, L. Pinard, O. Francais, and L. Rousseau, "High-sensitivity optical monitoring of a micromechanical resonator with a quantum-limited optomechanical sensor," *Physical Review Letters,* vol. 97, p. 133601, 2006.

[66] O. Arcizet, T. Briant, A. Heidmann, and M. Pinard, "Beating quantum limits in an optomechanical sensor by cavity detuning," *Physical Review A,* vol. 73, p. 033819, 2006.

[67] A. G. Krause, M. Winger, T. D. Blasius, Q. Lin, and O. Painter, "A high-resolution microchip optomechanical accelerometer," *Nature Photonics,* vol. 6, pp. 768-772, 2012.

[68] T. Baba, "Slow light in photonic crystals," *Nature Photonics,* vol. 2, pp. 465-473, 2008.

[69] X. Yang, M. Yu, D.-L. Kwong, and C. W. Wong, "All-optical analog to electromagnetically induced transparency in multiple coupled photonic crystal cavities," *Physical Review Letters,* vol. 102, p. 173902, 2009.

[70] M. F. Yanik, W. Suh, Z. Wang, and S. Fan, "Stopping light in a waveguide with an all-optical analog of electromagnetically induced transparency," *Physical Review Letters,* vol. 93, p. 233903, 2004.

[71] M. R. Singh, "Anomalous electromagnetically induced transparency in photonic-band-gap materials," *Physical Review A,* vol. 70, pp. 033813, 2004.
[72] A. H. Safavi-Naeini, T. M. Alegre, J. Chan, M. Eichenfield, M. Winger, Q. Lin, J. T. Hill, D. E. Chang, and O. Painter, "Electromagnetically induced transparency and slow light with optomechanics," *Nature,* vol. 472, pp. 69-73, 2011.
[73] A. K. Patnaik, J. Liang, and K. Hakuta, "Slow light propagation in a thin optical fiber via electromagnetically induced transparency," *Physical Review A,* vol. 66, pp. 063808, 2002.
[74] F. Le Kien and K. Hakuta, "Intracavity electromagnetically induced transparency in atoms around a nanofiber with a pair of Bragg grating mirrors," *Physical Review A,* vol. 79, pp. 043813, 2009.
[75] L. Thévenaz, "Slow and fast light in optical fibres," *Nature Photonics,* vol. 2, pp. 474-481, 2008.
[76] Y. A. Vlasov, M. O'Boyle, H. F. Hamann, and S. J. McNab, "Active control of slow light on a chip with photonic crystal waveguides," *Nature,* vol. 438, pp. 65-69, 2005.
[77] T. F. Krauss, "Slow light in photonic crystal waveguides," *Journal of Physics D: Applied Physics,* vol. 40, pp. 2666, 2007.
[78] K. M. Awan, S. A. Schulz, D. X. Liu, K. Dolgaleva, J. Upham, and R. W. Boyd, "Post-process wavelength tuning of silicon photonic crystal slow-light waveguides," *Optics Letters,* vol. 40, pp. 1952-1955, 2015.
[79] Y. Hamachi, S. Kubo, and T. Baba, "Slow light with low dispersion and nonlinear enhancement in a lattice-shifted photonic crystal waveguide," *Optics Letters,* vol. 34, pp. 1072-1074, 2009.
[80] L. H. Frandsen, A. V. Lavrinenko, J. Fage-Pedersen, and P. I. Borel, "Photonic crystal waveguides with semi-slow light and tailored dispersion properties," *Optics Express,* vol. 14, pp. 9444-9450, 2006.
[81] C. Caer, X. L. Roux, D. Marris-Morini, N. Izard, L. Vivien, D. Gao, and E. Cassan, "Dispersion engineering of wide slot photonic crystal waveguides by Bragg-like corrugation of the slot," *IEEE Photonics Technology Letters,* vol. 23, pp. 1298-1300, 2011.
[82] S. Boutami, B. B. Bakir, H. Hattori, X. Letartre, J.-L. Leclercq, P. Rojo-Romeo, M. Garrigues, C. Seassal, and P. Viktorovitch, "Broadband and compact 2-D photonic crystal reflectors with controllable polarization dependence," *IEEE Photonics Technology Letters,* vol. 18, pp. 835-837, 2006.
[83] K. B. Crozier, V. Lousse, O. Kilic, S. Kim, S. Fan, and O. Solgaard, "Air-bridged photonic crystal slabs at visible and near-infrared wavelengths," *Physical Review B,* vol. 73, p. 115126, 2006.
[84] W. Zhou, D. Zhao, Y.-C. Shuai, H. Yang, S. Chuwongin, A. Chadha, J.-H. Seo, K. X. Wang, V. Liu, and Z. Ma, "Progress in 2D photonic crystal Fano resonance photonics," *Progress in Quantum Electronics,* vol. 38, pp. 1-74, 2014.
[85] S. Boutami, B. Benbakir, J.-L. Leclercq, and P. Viktorovitch, "Compact and polarization controlled 1.55 μm vertical-cavity surface-emitting

laser using single-layer photonic crystal mirror," *Applied Physics Letters,* vol. 91, pp. 071105, 2007.

[86] L. Zeng, Y. Yi, C. Hong, J. Liu, N. Feng, X. Duan, L. Kimerling, and B. Alamariu, "Efficiency enhancement in Si solar cells by textured photonic crystal back reflector," *Applied Physics Letters,* vol. 89, pp. 111111, 2006.

[87] M. Lončar, A. Scherer, and Y. Qiu, "Photonic crystal laser sources for chemical detection," *Applied Physics Letters,* vol. 82, pp. 4648-4650, 2003.

[88] S. A. Asher, V. L. Alexeev, A. V. Goponenko, A. C. Sharma, I. K. Lednev, C. S. Wilcox, and D. N. Finegold, "Photonic crystal carbohydrate sensors: low ionic strength sugar sensing," *Journal of the American Chemical Society,* vol. 125, pp. 3322-3329, 2003.

[89] J. O. Grepstad, P. Kaspar, O. Solgaard, I.-R. Johansen, and A. S. Sudbø, "Photonic-crystal membranes for optical detection of single nano-particles, designed for biosensor application," *Optics Express,* vol. 20, pp. 7954-7965, 2012.

[90] J. Chee, J. Hwu, T. Kim, J. Kubby, S. Velicu, and N. Gupta, "Large size MOEMS Fabry-Perot interferometer filter for focal plane array hyperspectral imaging," in *SPIE OPTO*, 2015, pp. 93750K-93750K-7.

[91] M. Tuohiniemi, A. Näsilä, A. Akujärvi, and M. Blomberg, "MOEMS Fabry–Pérot interferometer with point-anchored Si-air mirrors for middle infrared," *Journal of Micromechanics and Microengineering,* vol. 24, pp. 095019, 2014.

[92] A. Rissanen, R. Mannila, and J. Antila, "Bragg reflectors for large optical aperture MEMS Fabry-Perot interferometers," in *SPIE Defense, Security, and Sensing*, 2012, pp. 83732R-83732R-8.

[93] A. Rissanen and R. L. Puurunen, "Use of ALD thin film Bragg mirror stacks in tuneable visible light MEMS Fabry-Perot interferometers," *SPIE MOEMS-MEMS*, pp. 82491A-82491A-9, 2012.

[94] M. W. Pruessner, T. H. Stievater, and W. S. Rabinovich, "Integrated waveguide Fabry-Perot microcavities with silicon/air Bragg mirrors," *Optics Letters,* vol. 32, pp. 533-535, 2007.

[95] L. Hui, Y. Lianshan, G. Zhen, P. Wei, W. Kunhua, L. Hengyi, and X. Luo, "Enhanced Focusing Properties Using Surface Plasmon Multilayer Gratings," *IEEE Photonics Journal,* vol. 4, pp. 57-64, 2012.

[96] M. Carras, G. Maisons, B. Simozrag, M. Garcia, O. Parillaud, J. Massies, and X. Marcadet, "Room-temperature continuous-wave metal grating distributed feedback quantum cascade lasers," *Applied Physics Letters,* vol. 96, pp. 161105-161105-3, 2010.

[97] L. Liyang, L. Fei, X. Mu, W. Tao, W. Jiayang, Z. Linjie, and S. Yikai, "Mode-Selective Hybrid Plasmonic Bragg Grating Reflector," *IEEE Photonics Technology Letters,* vol. 24, pp. 1765-1767, 2012.

[98] Z. Yu, P. Deshpande, W. Wei, J. Wang, and S. Y. Chou, "Reflective polarizer based on a stacked double-layer subwavelength metal grating structure fabricated using nanoimprint lithography," *Applied Physics Letters,* vol. 77, pp. 927-929, 2000.

[99] A. Liu, F. Fu, Y. Wang, B. Jiang, and W. Zheng, "Polarization-insensitive subwavelength grating reflector based on a semiconductor-insulator-metal structure," *Optics Express,* vol. 20, pp. 14991-15000, 2012.

[100] D. A. Horsley, J. Provine, and J. L. Skinner, "Integration of subwavelength metal gratings with MEMS actuators," pp. 600810-600810, 2005.

[101] J. Il Woong, S. Basu Mallick, and O. Solgaard, "A Large-Area High-Reflectivity Broadband Monolithic Single-Crystal-Silicon Photonic Crystal Mirror MEMS Scanner With Low Dependence on Incident Angle and Polarization," *Selected Topics in Quantum Electronics, IEEE Journal of,* vol. 15, pp. 1447-1454, 2009.

[102] Y. Zhang, M. Khan, Y. Huang, J. Ryou, P. Deotare, R. Dupuis, and M. Loncar, "Photonic crystal nanobeam lasers," *Applied Physics Letters,* vol. 97, pp. 051104-051104-3, 2010.

[103] H. Yang, D. Zhao, S. Chuwongin, J.-H. Seo, W. Yang, Y. Shuai, J. Berggren, M. Hammar, Z. Ma, and W. Zhou, "Transfer-printed stacked nanomembrane lasers on silicon," *Nat Photon,* vol. 6, pp. 615-620, 2012.

[104] Y. Wang, Y. Kanamori, H. Zhu, and K. Hane, "Single layer silicon photonic crystal slab," *Photonics and Nanostructures - Fundamentals and Applications,* vol. 10, pp. 146-152, 2012.

[105] S. Basu Mallick, J. Il Woong, A. M. Meisner, J. Provine, R. T. Howe, and O. Solgaard, "Multilayered Monolithic Silicon Photonic Crystals," *IEEE Photonics Technology Letters,* vol. 23, pp. 730-732, 2011.

[106] S. Yichen, Z. Deyin, G. Medhi, R. Peale, M. Zhenqiang, W. Buchwald, R. Soref, and Z. Weidong, "Fano-Resonance Photonic Crystal Membrane Reflectors at Mid- and Far-Infrared," *IEEE Photonics Journal,* vol. 5, pp. 4700206-4700206, 2013.

[107] R. Shankar, R. Leijssen, I. Bulu, and M. Lon?ar, "Mid-infrared photonic crystal cavities in silicon," *Optics Express,* vol. 19, pp. 5579-5586, 2011.

[108] S. Y. Lin, J. G. Fleming, D. L. Hetherington, B. K. Smith, R. Biswas, K. M. Ho, M. M. Sigalas, W. Zubrzycki, S. R. Kurtz, and J. Bur, "A three-dimensional photonic crystal operating at infrared wavelengths," *Nature,* vol. 394, pp. 251-253, 1998.

[109] M. Muneeb, X. Chen, P. Verheyen, G. Lepage, S. Pathak, E. Ryckeboer, A. Malik, B. Kuyken, M. Nedeljkovic, J. Van Campenhout, G. Z. Mashanovich, and G. Roelkens, "Demonstration of Silicon-on-insulator mid-infrared spectrometers operating at 3.8um," *Optics Express,* vol. 21, pp. 11659-11669, 2013.

[110] C. Reimer, M. Nedeljkovic, D. J. M. Stothard, M. O. S. Esnault, C. Reardon, L. O'Faolain, M. Dunn, G. Z. Mashanovich, and T. F. Krauss, "Mid-infrared photonic crystal waveguides in silicon," *Optics Express,* vol. 20, pp. 29361-29368, 2012.

[111] S. Kim, S. Hadzialic, A. S. Sudbo, and O. Solgaard, "Reflectivity and polarization dependence of polysilicon single-film broadband photonic crystal micro-mirrors," *Optics Express,* vol. 20, pp. 6306-6315, 2012.

[112] X. Wu, C. Jan, and O. Solgaard, "Single-Crystal Silicon Photonic-Crystal Fiber-Tip Pressure Sensors," *Journal of Microelectromechanical Systems,* vol. 24, pp. 968-975, 2015.
[113] J. Wöllenstein, A. Eberhardt, S. Rademacher, and K. Schmitt, "Miniaturized multi channel infrared optical gas sensor system," pp. 80660Q-80660Q, 2011.
[114] J. Mayrwöger, C. Mitterer, W. Reichl, C. Krutzler, and B. Jakoby, "Fabry-Perot-based thin film structure used as IR-emitter of an NDIR gas sensor: ray tracing simulations and measurements," pp. 80660K-80660K, 2011.
[115] A. J. Keating, J. Antoszewski, K. K. M. B. D. Silva, K. J. Winchester, T. Nguyen, J. M. Dell, C. A. Musca, L. Faraone, P. Mitra, J. D. Beck, M. R. Skokan, and J. E. Robinson, "Design and Characterization of Fabry–Pérot MEMS-Based Short-Wave Infrared Microspectrometers," *Journal of Electronic Materials,* vol. 37, pp. 1811-1820, 2008.
[116] C. A. Musca, J. Antoszewski, K. J. Winchester, A. J. Keating, T. Nguyen, K. K. M. Silva, J. M. Dell, L. Faraone, P. Mitra, J. D. Beck, M. R. Skokan, and J. E. Robinson, "Monolithic integration of an infrared photon detector with a MEMS-based tunable filter," *IEEE Electron Device Letters,* vol. 26, pp. 888-890, 2005.
[117] J. S. Milne, J. M. Dell, A. J. Keating, and L. Faraone, "Widely Tunable MEMS-Based Fabry Perot Filter," *Journal of Microelectromechanical Systems,* vol. 18, pp. 905-913, 2009.
[118] T. J. Russin, M. Kerber, A. Russin, A. Wang, and R. Waters, "Fabrication and Analysis of a MEMS NIR Fabry Perot Interferometer," *Journal of Microelectromechanical Systems,* vol. 21, pp. 181-189, 2012.
[119] M. Malak, F. Marty, N. Pavy, Y. A. Peter, L. Ai-Qun, and T. Bourouina, "Cylindrical Surfaces Enable Wavelength-Selective Extinction and Sub-0.2 nm Linewidth in 250um-Gap Silicon Fabry-Perot Cavities," *Journal of Microelectromechanical Systems,* vol. 21, pp. 171-180, 2012.
[120] W. Suh, M. F. Yanik, O. Solgaard, and F. Shanhui, "Displacement-sensitive photonic crystal structures based on guided resonance in photonic crystal slabs," *Applied Physics Letters,* vol. 82, pp. 1999-2001, 2003.
[121] R. V. Rossel, D. Walvoort, A. McBratney, L. J. Janik, and J. Skjemstad, "Visible, near infrared, mid infrared or combined diffuse reflectance spectroscopy for simultaneous assessment of various soil properties," *Geoderma,* vol. 131, pp. 59-75, 2006.
[122] N. Rochat, A. Troussier, A. Hoang, and F. Vinet, "Multiple internal reflection spectroscopy for quantitative infrared analysis of thin-film surface coating for biological environment," *Materials Science and Engineering: C,* vol. 23, pp. 99-103, 2003.
[123] V. G. Artioushenko, N. I. Afanasyeva, A. A. Lerman, A. P. Kryukov, E. Kuzin, N. N. Zharkova, V. G. Plotnichenko, G. A. Frank, G. Didenko, and V. V. Sokolov, "Medical applications of MIR-fiber spectroscopic probes," in *Europto Biomedical Optics' 93*, pp. 137-142, 1994.
[124] I. Puscasu, E. A. Johnson, M. U. Pralle, M. P. McNeal, J. T. Daly, and A. C. Greenwald, "Photonic crystals enable infrared gas sensors," in

Optical Science and Technology, the SPIE 49th Annual Meeting, pp. 58-66, 2004.
[125] J. S. Milne, J. M. Dell, A. J. Keating, and L. Faraone, "Widely tunable MEMS-based Fabry–Perot filter," *Journal of Microelectromechanical Systems,* vol. 18, pp. 905-913, 2009.
[126] N. Quack, S. Blunier, J. Dual, F. Felder, M. Arnold, and H. Zogg, "Mid-Infrared tunable resonant cavity enhanced detectors," *Sensors,* vol. 8, pp. 5466-5478, 2008.
[127] J. Michel, J. Liu, and L. C. Kimerling, "High-performance Ge-on-Si photodetectors," *Nature Photonics,* vol. 4, pp. 527-534, 2010.
[128] T. Fukazawa, F. Ohno, and T. Baba, "Very compact arrayed-waveguide-grating demultiplexer using Si photonic wire waveguides," *Japanese journal of applied physics,* vol. 43, pp. L673, 2004.
[129] G. T. Reed, G. Mashanovich, F. Gardes, and D. Thomson, "Silicon optical modulators," *Nature Photonics,* vol. 4, pp. 518-526, 2010.
[130] D. J. Moss, R. Morandotti, A. L. Gaeta, and M. Lipson, "New CMOS-compatible platforms based on silicon nitride and Hydex for nonlinear optics," *Nature Photonics,* vol. 7, pp. 597-607, 2013.
[131] J. S. Levy, M. A. Foster, A. L. Gaeta, and M. Lipson, "Harmonic generation in silicon nitride ring resonators," *Optics Express,* vol. 19, pp. 11415-11421, 2011.
[132] C. Xiong, W. H. Pernice, and H. X. Tang, "Low-loss, silicon integrated, aluminum nitride photonic circuits and their use for electro-optic signal processing," *Nano Letters,* vol. 12, pp. 3562-3568, 2012.
[133] H. Jung, C. Xiong, K. Y. Fong, X. Zhang, and H. X. Tang, "Optical frequency comb generation from aluminum nitride microring resonator," *Optics Letters,* vol. 38, pp. 2810-2813, 2013.
[134] A. G. Griffith, R. K. Lau, J. Cardenas, Y. Okawachi, A. Mohanty, R. Fain, Y. H. D. Lee, M. Yu, C. T. Phare, and C. B. Poitras, "Silicon-chip mid-infrared frequency comb generation," *Nature Communications,* vol. 6, 2015.
[135] S. Tadesse, H. Li, Q. Liu, and M. Li, "Surface Acoustic Wave Modulation of Optical Cavities on a Suspended Membrane," in *CLEO: Science and Innovations*, 2015, pp. STh4I. 7.
[136] S. A. Tadesse and M. Li, "Sub-optical wavelength acoustic wave modulation of integrated photonic resonators at microwave frequencies," *Nature communications,* vol. 5, 2014.
[137] N. Wang, F.-L. Hsiao, J. Tsai, M. Palaniapan, D.-L. Kwong, and C. Lee, "Numerical and experimental study on silicon microresonators based on phononic crystal slabs with reduced central-hole radii," *Journal of Micromechanics and Microengineering,* vol. 23, pp. 065030, 2013.
[138] T. Wang, X. Mu, P. Kropelnicki, A. B. Randles, and C. Lee, "Viscosity and density decoupling method using a higher order Lamb wave sensor," *Journal of Micromechanics and Microengineering,* vol. 24, pp. 075002, 2014.
[139] H. Li, S. A. Tadesse, Q. Liu, and M. Li, "Nanophotonic cavity optomechanics with propagating phonons in microwave Ku band," *arXiv preprint arXiv:1507.00808,* 2015.

[140] H. Li, S. A. Tadesse, Q. Liu, and M. Li, "Nanophotonic cavity optomechanics with propagating acoustic waves at frequencies up to 12 GHz," *Optica,* vol. 2, pp. 826-831, 2015.
[141] W. Song, M. Chahal, G. K. Celler, Y. Jaluria, G. T. Reed, and W. Jiang, "The influence of substrate on SOI photonic crystal thermo-optic devices," *Optics Express,* vol. 21, pp. 4235-4243, 2013.
[142] J. Malik, K. Jindal, V. Kumar, V. Kumar, A. Kumar, K. S. Singh, and T. Singh, "Effect of temperature on photonic band gaps in semiconductor-based one-dimensional photonic crystal," *Advances in Optical Technologies,* vol. 2013, 2013.
[143] C. Markos, K. Vlachos, and G. Kakarantzas, "Bending loss and thermo-optic effect of a hybrid PDMS/silica photonic crystal fiber," *Optics Express,* vol. 18, pp. 24344-24351, 2010.
[144] S. H. Teo, A. Liu, J. Zhang, M. Hong, J. Singh, M. Yu, N. Singh, and G. Lo, "Photonic bandgap crystal resonator enhanced, laser controlled modulations of optical interconnects for photonic integrated circuits," *Optics Express,* vol. 16, pp. 7842-7848, 2008.
[145] W. S. Fegadolli, G. Vargas, X. Wang, F. Valini, L. A. Barea, J. E. Oliveira, N. Frateschi, A. Scherer, V. R. Almeida, and R. R. Panepucci, "Reconfigurable silicon thermo-optical ring resonator switch based on Vernier effect control," *Optics Express,* vol. 20, pp. 14722-14733, 2012.
[146] D. M. Beggs, T. P. White, L. O'Faolain, and T. F. Krauss, "Ultracompact and low-power optical switch based on silicon photonic crystals," *Optics Letters,* vol. 33, pp. 147-149, 2008.
[147] D. Hohlfeld, M. Epmeier, and H. Zappe, "A thermally tunable, silicon-based optical filter," *Sensors and Actuators A: Physical,* vol. 103, pp. 93-99, 2003.
[148] W. Qian, C.-L. Zhao, S. He, X. Dong, S. Zhang, Z. Zhang, S. Jin, J. Guo, and H. Wei, "High-sensitivity temperature sensor based on an alcohol-filled photonic crystal fiber loop mirror," *Optics Letters,* vol. 36, pp. 1548-1550, 2011.
[149] H. Lu, B. Sadani, G. Ulliac, C. Guyot, N. Courjal, M. Collet, F. I. Baida, and M.-P. Bernal, "Integrated temperature sensor based on an enhanced pyroelectric photonic crystal," *Optics Express,* vol. 21, pp. 16311-16318, 2013.
[150] S. M. Tripathi, W. J. Bock, A. Kumar, and P. Mikulic, "Temperature insensitive high-precision refractive-index sensor using two concatenated dual-resonance long-period gratings," *Optics Letters,* vol. 38, pp. 1666-1668, 2013.
[151] Y. Wang, D. Wang, C. Liao, T. Hu, J. Guo, and H. Wei, "Temperature-insensitive refractive index sensing by use of micro Fabry–Pérot cavity based on simplified hollow-core photonic crystal fiber," *Optics Letters,* vol. 38, pp. 269-271, 2013.
[152] B. Guha, J. Cardenas, and M. Lipson, "Athermal silicon microring resonators with titanium oxide cladding," *Optics Express,* vol. 21, pp. 26557-26563, 2013.
[153] J. Teng, P. Dumon, W. Bogaerts, H. Zhang, X. Jian, X. Han, M. Zhao, G. Morthier, and R. Baets, "Athermal Silicon-on-insulator ring

resonators by overlaying a polymer cladding on narrowed waveguides," *Optics Express,* vol. 17, pp. 14627-14633, 2009.
[154] B. Guha and M. Lipson, "Controlling thermo-optic response in microresonators using bimaterial cantilevers," *Optics Letters,* vol. 40, pp. 103-106, 2015.
[155] S. Johnson and J. Joannopoulos, "Block-iterative frequency-domain methods for Maxwell's equations in a planewave basis," *Optics Express,* vol. 8, pp. 173-190, 2001.
[156] M. Kitamura, S. Iwamoto, and Y. Arakawa, "Enhanced light emission from an organic photonic crystal with a nanocavity," *Applied Physics Letters,* vol. 87, p. 151119, 2005.
[157] M. Belotti, J. F. Galisteo Lòpez, S. De Angelis, M. Galli, I. Maksymov, L. C. Andreani, D. Peyrade, and Y. Chen, "All-optical switching in 2D silicon photonic crystals with low loss waveguides and optical cavities," *Optics Express,* vol. 16, pp. 11624-11636, 2008.
[158] D. B. Nash, "Mid-infrared reflectance spectra (2.3–22 μm) of sulfur, gold, KBr, MgO, and halon," *Applied optics,* vol. 25, pp. 2427-2433, 1986.
[159] E. Kuramochi, M. Notomi, S. Hughes, A. Shinya, T. Watanabe, and L. Ramunno, "Disorder-induced scattering loss of line-defect waveguides in photonic crystal slabs," *Physical Review B,* vol. 72, p. 161318, 2005.
[160] M. Notomi, K. Yamada, A. Shinya, J. Takahashi, C. Takahashi, and I. Yokohama, "Extremely large group-velocity dispersion of line-defect waveguides in photonic crystal slabs," *Physical Review Letters,* vol. 87, p. 253902, 2001.
[161] S. Rahimi, A. Hosseini, X. Xu, H. Subbaraman, and R. T. Chen, "Group-index independent coupling to band engineered SOI photonic crystal waveguide with large slow-down factor," *Optics Express,* vol. 19, pp. 21832-21841, 2011.
[162] A. Y. Petrov and M. Eich, "Zero dispersion at small group velocities in photonic crystal waveguides," *Applied Physics Letters,* vol. 85, pp. 4866-4868, 2004.
[163] J. Li, T. P. White, L. O'Faolain, A. Gomez-Iglesias, and T. F. Krauss, "Systematic design of flat band slow light in photonic crystal waveguides," *Optics Express,* vol. 16, pp. 6227-6232, 2008.
[164] K. Nozaki, A. Shinya, S. Matsuo, T. Sato, E. Kuramochi, and M. Notomi, "Ultralow-energy and high-contrast all-optical switch involving Fano resonance based on coupled photonic crystal nanocavities," *Optics Express,* vol. 21, pp. 11877-11888, 2013.
[165] M. W. Pruessner, T. H. Stievater, M. S. Ferraro, and W. S. Rabinovich, "Thermo-optic tuning and switching in SOI waveguide Fabry-Perot microcavities," *Optics Express,* vol. 15, pp. 7557-7563, 2007.
[166] M. Han and A. Wang, "Temperature compensation of optical microresonators using a surface layer with negative thermo-optic coefficient," *Optics Letters,* vol. 32, pp. 1800-1802, 2007.
[167] E.-S. Kang, W.-S. Kim, D.-J. Kim, and B.-S. Bae, "Reducing the thermal dependence of silica-based arrayed-waveguide grating using

inorganic-organic hybrid materials," *IEEE Photonics Technology Letters,* vol. 16, pp. 2625-2627, 2004.
[168] J. Kischkat, S. Peters, B. Gruska, M. Semtsiv, M. Chashnikova, M. Klinkmüller, O. Fedosenko, S. Machulik, A. Aleksandrova, and G. Monastyrskyi, "Mid-infrared optical properties of thin films of aluminum oxide, titanium dioxide, silicon dioxide, aluminum nitride, and silicon nitride," *Applied optics,* vol. 51, pp. 6789-6798, 2012.
[169] M. Noro, K. Suzuki, N. Kishi, H. Hara, T. Watanabe, and H. Iwaoka, "CO_2/H_2O gas sensor using a tunable Fabry-Perot filter with wide wavelength range," in *Micro Electro Mechanical Systems, 2003. MEMS-03 Kyoto. IEEE The Sixteenth Annual International Conference on*, pp. 319-322, 2003.
[170] M. Ebermann, N. Neumann, K. Hiller, M. Seifert, M. Meinig, and S. Kurth, "Resolution and speed improvements of mid-infrared Fabry-Perot microspectrometers for the analysis of hydrocarbon gases," in *SPIE MOEMS-MEMS*, pp. 89770T-89770T-9, 2014.
[171] M. Tuohiniemi and M. Blomberg, "Surface-micromachined silicon air-gap Bragg reflector for thermal infrared," *Journal of Micromechanics and Microengineering,* vol. 21, p. 075014, 2011.
[172] M. Shur, "Terahertz technology: devices and applications," in *Solid-State Circuits Conference, 2005. ESSCIRC 2005. Proceedings of the 31st European*, pp. 13-21, 2005.
[173] E. Pickwell and V. Wallace, "Biomedical applications of terahertz technology," *Journal of Physics D: Applied Physics,* vol. 39, p. R301, 2006.
[174] P. H. Siegel, "Terahertz technology in biology and medicine," in *Microwave Symposium Digest, 2004 IEEE MTT-S International*, pp. 1575-1578, 2004.
[175] S. Koenig, D. Lopez-Diaz, J. Antes, F. Boes, R. Henneberger, A. Leuther, A. Tessmann, R. Schmogrow, D. Hillerkuss, and R. Palmer, "Wireless sub-THz communication system with high data rate," *Nature Photonics,* vol. 7, pp. 977-981, 2013.
[176] H.-T. Chen, W. J. Padilla, J. M. O. Zide, A. C. Gossard, A. J. Taylor, and R. D. Averitt, "Active terahertz metamaterial devices," *Nature,* vol. 444, pp. 597-600, 2006.
[177] I. Al-Naib, Y. Yang, M. M. Dignam, W. Zhang, and R. Singh, "Ultra-high Q even eigenmode resonance in terahertz metamaterials," *Applied Physics Letters,* vol. 106, pp. 011102, 2015.
[178] W. Cao, R. Singh, I. A. I. Al-Naib, M. He, A. J. Taylor, and W. Zhang, "Low-loss ultra-high-Q dark mode plasmonic Fano metamaterials," *Optics Letters,* vol. 37, pp. 3366-3368, 2012.
[179] I. A. I. Al-Naib, C. Jansen, N. Born, and M. Koch, "Polarization and angle independent terahertz metamaterials with high Q-factors," *Applied Physics Letters,* vol. 98, pp. 091107, 2011.
[180] I. Al-Naib, R. Singh, C. Rockstuhl, F. Lederer, S. Delprat, D. Rocheleau, M. Chaker, T. Ozaki, and R. Morandotti, "Excitation of a high-Q subradiant resonance mode in mirrored single-gap asymmetric split ring

resonator terahertz metamaterials," *Applied Physics Letters,* vol. 101, pp. 071108, 2012.
[181] T. Chen, P. Liu, J. Liu, and Z. Hong, "A terahertz photonic crystal cavity with high Q-factors," *Applied Physics B,* vol. 115, pp. 105-109, 2014.

LIST OF PUBLICATIONS

Journals and Letters

1. **Chong Pei Ho**, Prakash Pitchappa and Chengkuo Lee, *Digitally reconfigurable binary coded terahertz metamaterial with output analogous to NOR and AND*, **J. Appl. Phys.,** vol. 119, no. 15, pp. 153104, 2016.
2. **Chong Pei Ho**, Prakash Pitchappa, Piotr Kropelnicki, Jian Wang, Hong Cai, Yuandong Gu and Chengkuo Lee, *Two Dimensional Photonic Crystal Based Fabry-Perot Etalon*, **Opt. Lett.**, vol. 40, no. 12, pp. 2743, 2015.
3. **Chong Pei Ho**, Prakash Pitchappa,Bo Woon Soon and Chengkuo Lee, *Suspended 2-D photonic crystal aluminium nitride membrane reflector*, **Opt. Express**, vol. 23, no. 8, pp. 10598-10603, 2015.
4. Prakash Pitchappa, **Chong Pei Ho**, You Qian, Lokesh Dhakar, Navab Singh and Chengkuo Lee, *Microelectromechanically tunable multiband metamaterial with preserved isotropy*, **Sci. Rep**., vol. 5, no. 11678, pp. 1-10, 2015. **(Shared first authorship)**
5. **Chong Pei Ho**, Prakash Pitchappa, Piotr Kropelnicki, Jian Wang, Hong Cai, Yuandong Gu and Chengkuo Lee, *Characterization of polycrystalline silicon based photonic crystal suspended membrane for high temperature applications*, **J. Nanophotonics**, vol. 8, no. 1, 084096, 2014.
6. **Chong Pei Ho**, Prakash Pitchappa, Piotr Kropelnicki, Jian Wang, Yuandong Gu and Chengkuo Lee, *Development of Polycrystalline Silicon Based Photonic Crystal Membrane for Mid-Infrared Applications*, **IEEE J. Sel. Top. Quantum Electron.**, vol. 20, no.4, 4900107, 2014.
7. **Chong Pei Ho**, Prakash Pitchappa, Yu-Sheng Lin, Chia-Yi Huang, Piotr Kropelnicki and Chengkuo Lee, *Electrothermally actuated microelectromechanical systems based Omega-ring terahertz metamaterial with polarization dependent characteristics*, **Appl. Phys. Lett.**, vol. 104, no. 16, pp. 161104, 2014.
8. **Chong Pei Ho**, Bo Li, Aaron J. Danner and Chengkuo Lee, *Design and modeling of 2-D photonic crystals based hexagonal triple-nano-ring resonators as biosensors,* **Microsyst. Technol.**, vol. 19, no. 1, pp. 53-60, 2013.
9. Dihan Hasan, **Chong Pei Ho** and Chengkuo Lee, *Thermally Tunable Absorption Induced Transparency (AIT) by Quasi-3D Bow-tie*

Nanostructure for Nonplasmonic and Volumetric Refractive Index Sensing at Mid IR, **Adv. Opt. Mater.,** to be published, 2016.

10. Dihan Hasan, Prakash Pitchappa, **Chong Pei Ho**, Bin Yang, Chunsheng Yang, and Chengkuo Lee, *Thermoplasmonic Study of a Triple Band Optical Nanoantenna Strongly Coupled to Mid IR Molecular Mode*, **Scientific Reports** (Nature publisher).,to be published, 2016.

11. Prakash Pitchappa, Manukumara Manjappa, **Chong Pei Ho**, Ranjan Singh, Navab Singh and Chengkuo Lee, *Active control of electromagnetically induced transparency analogue in terahertz MEMS metamaterial*, **Adv. Opt. Mater.**, to be published, 2016.

12. Prakash Pitchappa, **Chong Pei Ho**, Longqing Cong, Ranjan Singh, Navab Singh and Chengkuo Lee, *Reconfigurable digital metamaterial for dynamic switching of terahertz anisotropy,* **Adv. Opt. Mater.**, to be published, 2016.

13. Dihan Hasan, **Chong Pei Ho**, Prakash Pitchappa,and Chengkuo Lee, *Dipolar Resonance Enhancement and Magnetic Resonance in Cross-coupled Bow-tie Nanoantenna Array by Plasmonic Cavity*, **ACS Photonics**, vol. 2, no. 7, pp. 890-898, 2015

14. Prakash Pitchappa, **Chong Pei Ho**, Lokesh Dhakar and Chengkuo Lee, *Microelectromechanically reconfigurable interpixelated metamaterial for independent tuning of multiple resonances at terahertz spectral region*, **Optica**, vol. 2, no. 6, pp. 571-578, 2015.

15. Prakash Pitchappa, Lokesh Dhakar, **Chong Pei Ho**, You Qian, Navab Singh and Chengkuo Lee, *Periodic array of subwavelength MEMS cantilevers for dynamic manipulation of terahertz waves*, **IEEE/ASME J. Microelectromech. Syst.**, vol. 24, no.3, pp. 525-527, 2015.

16. Bo Li, **Chong Pei Ho**, Fu-Li Hsiao, and Chengkuo Lee, *Lateral lattice shift engineered slow light in elliptical photonics crystal waveguides*, **J. Nanophotonics**, vol. 8, pp. 084090, 2014.

17. Prakash Pitchappa, **Chong Pei Ho**, Piotr Kropelnicki, Navab Singh, Dim-Lee Kwong and Chengkuo Lee, *Micro-electro-mechanically switchable near infrared complementary metamaterial absorber*, **Appl. Phys. Lett.**, vol. 104, no. 20, pp. 201114, 2014.

18. Prakash Pitchappa, **Chong Pei Ho**, Piotr Kropelnicki, Navab Singh, Dim-Lee Kwong and Chengkuo Lee, *Dual band complementary metamaterial*

absorber in near infrared region, **J. Appl. Phys.**, vol. 115, no. 19, pp. 193109, 2014.

19. Prakash Pitchappa, **Chong Pei Ho**, Yu-Sheng Lin, Piotr Kropelnicki, Chia-Yi Huang, Navab Singh and Chengkuo Lee, *Micro-electro-mechanically Tunable Metamaterial With Enhanced Electro-optic Performance,* **Appl. Phys. Lett.**, vol. 104, no. 15, pp. 151104, 2014.

20. Yu-Sheng Lin, **Chong Pei Ho**, Kah How Koh, and Chengkuo Lee, *Fabry-Perot filter using grating structures*, **Opt. Lett.**, vol. 38, no. 6, pp. 902-904, 2013.

Reviewed Conference Proceedings and Presentations

1. **Chong Pei Ho**, Prakash Pitchappa, and Chengkuo Lee, *Polycrystalline Silicon based Photonic Crystal Fabry-Perot Etalon*, The 20th OptoElectronics and Communications Conf. (OECC 2015), Shanghai, China, Jun.28-Jul. 02, 2015.

2. **Chong Pei Ho**, Prakash Pitchappa, Yu-Sheng Lin and Chengkuo Lee, *Electrothermally actuated MEMS terahertz metamaterial*, 2014 IEEE Intern. Conf. on Optical MEMS & Nanophotonics (OMN 2014)**,** Glasgow, Scotland, Aug. 17-21, 2014.

3. **Chong Pei Ho**, Prakash Pitchappa, Piotr Kropelnicki, Jian Wang, Hong Cai, Yuandong Gu and Chengkuo Lee, *Characterization of Polycrystalline Silicon Based Photonic Crystal Membrane for High Temperature Gas Sensing Applications*, The 6th International Symposium on Microchemistry and Microsystems (ISMM 2014)**,** pp. 27-28, Singapore, Jul. 29-Aug. 1, 2014.

4. **Chong Pei Ho**, Prakash Pitchappa, Piotr Kropelnicki, and Chengkuo Lee, *Development of Polycrystalline Silicon Based Photonic Crystal Membrane with Cross Holes in Mid-infrared Range*, Optics & Photonics Taiwan, International Conference 2013**,** pp. P0102-P034, National Central University, Zhongli, Taiwan, Dec. 5-7, 2013.

5. Prakash Pitchappa, **Chong Pei Ho**, and Chengkuo Lee, *Subwavelength prestressed microcantilevers based metamaterials for efficient manipulation of terahertz waves,* Intern. Microwave Workshop Series on Advanced Materials and Processes for RF and THz Applications (IMWS-AMP 2015), Suzhou, China, Jul. 1-3, 2015.

6. Prakash Pitchappa, **Chong Pei Ho**, and Chengkuo Lee, *Polarization-insensitive Electro-Optic Switching in Terahertz MEMS Metamaterial*, Intern. Microwave Workshop Series on Advanced Materials and Processes for RF and THz Applications, Suzhou, China, Jul. 1-3, 2015.

7. Prakash Pitchappa, **Chong Pei Ho**, and Chengkuo Lee, *Active MEMS Metamaterial with Uniaxially Isotropic Dual Band Switching Characteristics in Terahertz Region*, The 20th OptoElectronics and Communications Conf., Shanghai, China, Jun.28-Jul. 02, 2015.

8. Prakash Pitchappa, **Chong Pei Ho**, Navab Singh, and Chengkuo Lee, *Electrostatically switchable MEMS terahertz metamaterial with polarization insensitive characteristics*, IEEE conf. on Electron Devices and Solid-state Circuits (EDSSC 2015), Singapore, Jun. 1-4, 2015.

9. Prakash Pitchappa, Lokesh Dhakar, **Chong Pei Ho**, You Qian, Tao Wang and Chengkuo Lee, *Subwavelength MEMS cantilever array for dynamic manipulation of terahertz waves* , The 10th IEEE Intern. Conf. on Nano/Micro Engineered and Molecular Systems (IEEE NEMS 2015), Xi'an, China, Apr. 7-11, 2015.

10. Prakash Pitchappa, **Chong Pei Ho**, You Qian, Yu-Sheng Lin, Navab Singh and Chengkuo Lee, *Enhaned controllability in MEMS metamaterial*, The 28th IEEE Intern. Conference on Micro Electro Mechanical Systems (IEEE MEMS 2015), pp. 1032-1035, Estoril, Portugal, Jan. 18-22, 2015.

11. Prakash Pitchappa, **Chong Pei Ho**, You Qian, Yu Sheng Lin, Navab Singh and Chengkuo Lee, *MEMS switchable infrared metamaterial absorber*, Intern. Conf. on Experimental Mechanics in conjunction with the 13th Asian Conf. on Experimental Mechanics 2014 (icEM2014-ACEM13), Singapore, Nov. 15-17, 2014.

12. Prakash Pitchappa, **Chong Pei Ho**, Yu-Sheng Lin and Chengkuo Lee, *Enhanced electro-optic switching characteristics using MEMS based terahertz metamaterial*, 2014 IEEE Intern. Conf. on Optical MEMS & Nanophotonics (OMN 2014), Glasgow, Scotland, Aug. 17-21, 2014. 209.

13. Prakash Pitchappa, **Chong Pei Ho**, Yu-Sheng Lin, Piotr Kropelnicki, Chia -Yi Huang, Navab Singh and Chengkuo Lee, *Coarse and Fine Tuning of Resonant Frequency for Terahertz Metamaterial using MEMS Technology*, The 6th International Symposium on Microchemistry and Microsystems (ISMM 2014), pp. 60-61, Singapore, Jul. 29-Aug. 1, 2014.

14. Bo Li, **Chong Pei Ho**, and Chengkuo Lee, *Development of silicon photonics*

dual disks resonators as chemical sensors, 2014 IEEE Intern. Conf. on Intelligent Sensors, Sensor Networks and Information Processing (ISSNIP 2014), Singapore, Apr. 21-24, 2014.

15. Prakash Pitchappa, **Chong Pei Ho**, Piotr Kropelnicki, and Chengkuo Lee, *Complementary Metamaterial Based Infrared Absorber*, Optics & Photonics Taiwan, International Conference 2013, pp. P0102-P030, National Central University, Zhongli, Taiwan, Dec. 5-7, 2013.

16. Bo Li, **Chong Pei Ho** and Chengkuo Lee, *Thermally tunable photonic dual-disk resonator with wide operation range*, 2013 IEEE International Conf. on Optical MEMS and Nanophotonics, pp. 91-92, Kanazawa, Japan, Aug. 18-22, 2013.

17. Tianhang Zhang, Bo Li, **Chong Pei Ho** and Chengkuo Lee, *high sensitivity silicon optical index sensor based on ring-assisted Mach-Zehnder interferometer*, 2013 IEEE International Conf. on Optical MEMS and Nanophotonics, pp. 129-130, Kanazawa, Japan, Aug. 18-22, 2013.

18. Nan Wang, Min Tang, Fu-Li Hsiao, **Chong Pei Ho**, Moorthi Palaniapan, Dim-Lee Kwong and Chengkuo Lee, *Experimental verification of phononic crystal slab based silicon microresonators*, 2013 IEEE International Conf. on Optical MEMS and Nanophotonics, pp. 131-132, Kanazawa, Japan, Aug. 18-22, 2013.

19. Fusheng Ma, Yu-Sheng Lin, You Qian, **Chong Pei Ho**, Prakash Pitchappa and Chengkuo Lee, *Development of tunable 3-D eSRR for THz applications*, 2013 IEEE International Conf. on Optical MEMS and Nanophotonics, pp. 141-142, Kanazawa, Japan, Aug. 18-22, 2013.

20. Prakash Pitchappa, **Chong Pei Ho**, Piotr Kropelnicki and Chengkuo Lee, *Complementary metamaterial infrared absorber*, 2013 IEEE International Conf. on Optical MEMS and Nanophotonics, pp. 143-144, Kanazawa, Japan, Aug. 18-22, 2013.

21. Yu-Sheng Lin, **Chong Pei Ho**, Prakash Pitchappa, Fusheng Ma, You Qian, Piotr Kropelnicki and Chengkuo Lee, *Tunable THz filter using 3-D split-ring resonators*, 2013 IEEE International Conf. on Optical MEMS and Nanophotonics, pp. 167-168, Kanazawa, Japan, Aug. 18-22, 2013.

22. Bo Li, **Chong Pei Ho** and Chengkuo Lee, *Development of Silicon Photonics Dual Disk Resonators as Chemical Sensors*, The 2nd Japan-Singapore Research Exchange & ICT Farm Project, Kyushu University, Japan, Aug. 16-17, 2013.